2016

The Oxidation And Decoration Chemistry Of Platinum And Palladium Nanoparticles On Carbon Supports

Ritubarna Banerjee
University of South Carolina

THE OXIDATION AND DECORATION CHEMISTRY OF PLATINUM AND PALLADIUM NANOPARTICLES ON CARBON SUPPORTS

by
Ritubarna Banerjee

Bachelor of Science
North Bengal University, 2000

Master of Science
North Bengal University, 2002

Master of Science
Arizona State University, 2009

Submitted in Partial Fulfillment of the Requirements

For the Degree of Doctor of Philosophy in

Chemical Engineering

College of Engineering and Computing

University of South Carolina

2016

Accepted by:

John R. Regalbuto, Major Professor

Christopher T. Williams, Committee Member

Miao Yu, Committee Member

Doug Blom, Committee Member

John Weidner, Committee Member

Cheryl L. Addy, Vice Provost and Dean of the Graduate School

ACKNOWLEDGEMENTS

I would like to take this opportunity to thank all the people without whom this PhD dissertation would not have been possible. I consider myself extremely lucky to have worked with them and hope to remain in touch with them forever in the future.

First and foremost, I would like to greatly acknowledge the guidance, support and constant encouragement from my PhD advisor, Prof. John R. Regalbuto. Having him as my mentor kept me constantly motivated to traverse the ups and downs of my research and I really appreciate all his help and brilliant ideas that helped channelize my research.

I would like to extend my gratitude to my PhD committee members for their valuable inputs during the different phases of my research. A special note of thanks to Dr. Doug Blom for his important suggestions and advice during all my electron microscopy sessions that form a vital part of my PhD.

I would like to thank my colleagues at the Center of Catalysis for Renewable Fuels (CReF) and my research group members for their help and useful scientific discussions, especially, Jadid Samad, John Tengco, Shuo Cao, Qiuli Liu and José L. Contreras-Mora.

Lastly, I would like to thank my family: my parents, Mr. Asim Mukherjee and Mrs. Monideepa Mukherjee for believing in me and supporting me, my loving husband, Dr. Sourav Banerjee for his patience, especially during the last phase of my research and my darling 5 year old daughter, Aishani Banerjee for her unconditional love.

ABSTRACT

Ultrasmall platinum and palladium nanoparticles supported on carbon are used in a wide variety of industrial catalytic processes including hydrogenation-dehydrogenation reactions, isomerization of hydrocarbons, ammonia and formic acid decomposition, the oxidation of carbon monoxide, alcohols and ammonia, and fuel cells. This dissertation covers three aspects of the chemistry of these ultrasmall, carbon supported nanoparticles.

In the first vein of work, the oft-observed discrepancy in Pd nanoparticle size estimation between chemisorption and other methods such as STEM and XRD is explored. It is demonstrated that lower-than-expected chemisorption uptake can stem from not only residual chloride, but also from the decoration of the Pd surface by the carbon support itself. The degree of decoration decreases with graphitization of the carbon supports due to stronger C-C interaction, whereas increased density of oxygen functional groups on the surface increases decoration, due to enhanced Pd-C interactions. A combined synthesis and chemisorption protocol featuring chloride free precursors and a mild oxidative pretreatment prior to chemisorption is established to eliminate the size discrepancy.

In the second vein, the ambient oxidation of ultra-small platinum nanoparticles was explored with a combination of powder XRD performed with a high sensitivity solid state detector, and aberration corrected electron microscopy with fast Fourier transform analysis. For the first time, the identity of the oxide phase is identified as Pt_3O_4, and the size window

of oxidation is accurately outlined: below 1.5 nm, nanoparticles exist only as oxides; from 1.5 to 2.5 nm, metallic and oxide phases occur, while above 2.5 nm, particles are completely metallic. Carbon supports of high microporosity give rise to large particle sizes at high metal loading, which stabilizes the particles against oxidation.

In the last avenue of research, the application of Strong Electrostatic Adsorption for the synthesis of Pt nanoparticles was tested for specialty carbons: multi-walled nanotubes, nanofibers, graphene nanoplatelets, etc. These materials displayed volcano-shaped uptake curves typical of electrostatic adsorption for both Pt anions at low pH and Pt cations at high pH. However, the regimes of uptake often did not correspond to the measured point of zero charge (PZC). It was seen that the PZC of many of the carbons could be changed with washing, and so was likely affected by residual impurities of the manufacturing process. This renders the measured PZC of these specialty carbons unreliable for predicting anion and cation uptake. On the other hand, the anion and cation uptake curves provide an "effective" PZC and do indicate the optimal pH for the synthesis of ultrasmall nanoparticles.

TABLE OF CONTENTS

LIST OF TABLES

LIST OF FIGURES

CHAPTER 1

INTRODUCTION

Catalysis has been used as an age old tool for decades in carrying out reactions in processes such as decomposition of alcohol by copper, iron and pumice stone, oxidation of coal gas by platinum and palladium, production of sulphuric acid using platinum and ammonia synthesis by osmium and iron [1, 2]. The economic contribution from catalysis is significant: all the attributes of catalysts translate to energy savings, less pollution, fewer side products, lower cost reactor materials, and hence to products which reduce global warming. It plays a very important role in affecting four sectors of the world's economy: petroleum, energy production, chemicals production, and the food industry. Some of the common applications of catalysts are as catalytic converters in automobiles for decreasing the emission of exhaust gas pollutants, fuel cells, Fischer Tropsch synthesis for producing synthetic fuels, hydrogenation in food processing, as enzymes in metabolism and catabolism, producing bulk chemicals and processing fuel feed stocks for harnessing energy [3-5]. Depending on whether the catalysts are in the same phase or different phase from the reactants, the reactions are classified as homogeneous or heterogeneous reactions.

1.1 Carbon Supports in Catalysis

The use of supports has long been appreciated in catalysis as it facilitates the formation of extremely small metal particles having a high proportion of atoms at the

surface; the particles have high thermal stability and the presence of the support allows the incorporation of beneficial additives, usually known as promoters. While planar supports like single crystals, films and facets facilitate the study of model reaction processes, practical applications demand the use of porous and high surface area supports.

Hence, the advent of carbon materials in catalysis. Carbon materials have been used as supports/catalysts for decades in heterogeneous catalytic reactions due to their desirable attributes of chemical inertness, stability, mechanical resistance, high surface area and optimum porosity [6-8]. This versatility of carbon affects not only the preparation, but also influences the resistance to sintering and the catalytic activity and selectivity of the catalyst and enables its application in the synthesis of chemical products [9], in fuel cell electrodes [10], hydrogenation-dehydrogenation reactions involving aliphatic and aromatic compounds [11,12], hydrodesulphurization of petroleum fractions or hydrogenation of carbon monoxide [13].

Depending on the sources from which it originates, carbon supports may contain various degrees of surface area, pores and surface groups and are classified as carbon blacks, activated carbons and graphitic carbons [Figure 1.1]. Carbon black consists of soot like particles that is virtually pure elemental carbon in the form of spherical, colloidal particles produced by incomplete combustion or thermal decomposition of gaseous or liquid hydrocarbons under controlled conditions [14]. The term activated carbon (also known as activated charcoal) defines a group of materials with highly developed internal surface area and porosity, and hence a large capacity for adsorbing chemicals from gases and liquids. The steps involved in the manufacturing process of activated carbons are carbonization (high temperature treatment to drive off volatile matter), followed by

physical or chemical activation to enhance the pore structure. Graphitic carbons generally have low surface area (10-50m^2/gm) and hence, are not generally used as catalyst supports. However, high surface area graphitic carbons can be manufactured by ball milling that has an enhanced surface area (600m^2/gm). These carbons are good as supports because of the unsaturated valences at the edge of the graphitic planes [15].

Apart from these generic forms of carbon, specialty carbons have also seized considerable amount of interest as catalyst supports since the discovery of carbon nanotubes [16]. Carbon nanotubes and nanofibers are graphitic filaments with diameters ranging from 0.4 to 500 nm and lengths in the range of several micrometers to millimeters. These are grown by the diffusion of carbon through a metal catalyst followed by subsequent precipitation as graphitic filaments [17].

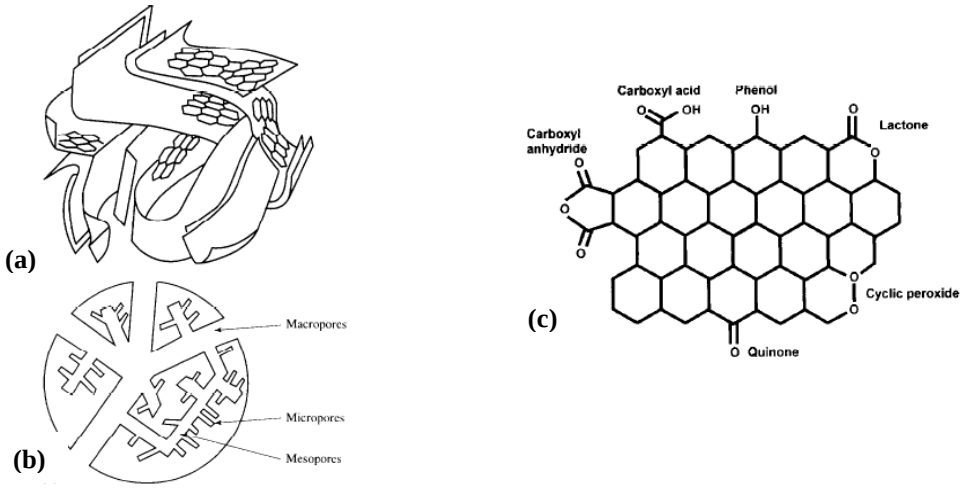

Figure 1.1 (a) Structure of activated carbon (b) an activated carbon granule (c) common surface oxygen groups on carbon surfaces

It has been seen during previous studies that the size of the metal nanoparticles is often governed by preparation methods, pretreatment conditions and the choice of supports

[18]. However, it is well documented that the role of the support is not merely that of a carrier; it may actually contribute catalytic activity and it may react to some extent with other catalyst ingredients during the manufacturing process. Further, the interaction between the active phase and the support phase can affect the catalytic activity [6]. The flexibility in the choice of carbon materials for catalyst supports is enormous owing to the huge differences in surface area, varying degrees of microporosity and the wide range of impurities and surface functional groups and as such, many details in the preparation, pre-treatment and post-treatment conditions are not adequately understood. The precise nature of carbon-oxygen structures is not entirely established but the results of many studies using different experimental techniques conclude that there may be several types of oxygen functional, as shown in Figure 1.1 [6]; the presence of these surface groups imparts the acid-base character to the carbons. These acid-base adsorption properties of carbons can be varied by different pretreatment conditions. The effect of support pretreatment on palladium catalysts supported on high surface area carbon black showed a substantial suppression of chemisorption surface area leading to larger particle sizes as compared to a surface average particle sizes obtained from Scanning Transmission Electron Microscopy [19]. In some other studies, it was shown that the presence of surface oxygen functional groups on the support favors the anchoring of metal nanoparticles [20, 21] whereas in other cases, it was found to be harmful for metal nanoparticle formation [22].

1.2 Science of Catalyst Preparation

Carbon supported platinum and palladium metals are used in a wide variety of industrial processes including hydrogenation of alkenes, hydrogenation of aromatics,

isomerization of hydrocarbons, ammonia decomposition, decomposition of formic acid, oxidation of carbon monoxide, oxidation of alcohols, oxidation of ammonia as well as in potential fuel cell applications. Typical heterogeneous catalysts in the industry consist of the transition metals deposited onto the inert support by a variety of deposition techniques. The deposition method is then, followed by drying/calcination and reduction to yield small metal nanoparticles. Through a variety of preparation methods, the ultimate goal is to obtain small metal nanoparticles with the maximum amount of metal atoms exposed on the surface, given the fact that the atoms at the center will be shielded from the reactant gases and hence, not take part in the reaction [23].

Some of the most commonly used catalyst preparation methods are dry impregnation, wet impregnation, strong electrostatic adsorption, deposition precipitation, ion-exchange, reactive adsorption [24]. In the impregnation method, the support is contacted with a liquid solution containing the precursor or metal ions. Depending on the volume of solution used, the method is termed Dry Impregnation (volume of impregnating precursor solution equal to the pore volume of the support) or Wet Impregnation (volume of impregnating precursor solution greater than the pore volume of the support). However, in these methods, a non-uniform metal precursor distribution may develop as the metal complex remains in solution and is carried to the support surface only on drying. The pH of the solution is not controlled before contacting with the support and as such, can change dramatically during impregnation. Deposition-precipitation uses excess solution whose pH is slowly and homogeneously increased to precipitate precursor at the support surface. In ion-exchange preparation, the cationic metal precursors are exchanged with counterions in a zeolite framework.

1.3 Strong Electrostatic Adsorption

One of the most recent techniques of catalyst preparation is Strong Electrostatic Adsorption (SEA) where strong interactions can be created between the support and precursor depending on the acidity of the impregnating solution. The method of Strong Electrostatic Adsorption (SEA) was first postulated by Brunelle [25] and has ever since been strongly implemented in the pioneering work of the Regalbuto group for both oxide as well as carbon supports [26, 27]. The theory behind SEA is to control the pH of the excess liquid so as to arrive at the optimal pH where the metal complex-surface interaction is the strongest [Figure 1.2]. While the surfaces of oxide supports contain hydroxyl groups, those of carbon supports contain aromatic Pi bonds that can protonate or deprotonate above or below a certain solution pH. The pH at which the hydroxyl groups or Pi-bonds are neutral is termed the *point of zero charge* (PZC). Below this pH, the groups protonate and become positively charged, and the surface can adsorb anionic metal complexes while above the PZC, the groups deprotonate and become negatively charged, and cations can be strongly adsorbed.

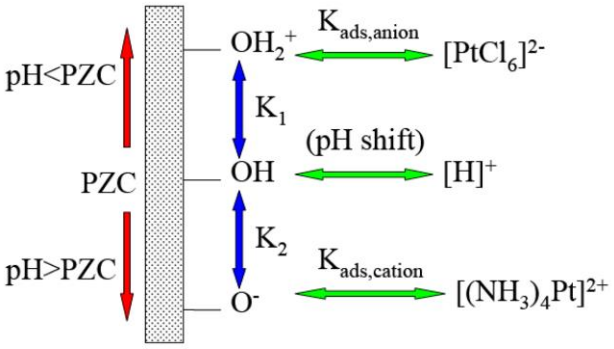

Figure 1.2 Strong Electrostatic Adsorption Mechanism depicting surface charging, protonation-deprotonation and adsorption

The SEA catalyst preparation process for platinum impregnation consists of the following steps:

1. **Point of Zero Charge (PZC) Determination:** The PZC of the support is first determined at high surface loading by measuring the final pH versus the initial pH. Based on the PZC, an anionic precursor, Chloroplatinic acid (or platinum hexachloride, PHC, $H_2[PtCl_6]$) is chosen for high PZC materials while a cationic precursor, tetraammineplatinum(II) chloride ([PTA, $Pt(NH_3)_4]OH_2$) is chosen for low PZC materials.
2. **Uptake Surveys to determine optimal pH:** Uptake surveys are conducted on the supports over a range of pH to determine the pH where the adsorption is the maximum. This pH then determines the point of maximum electrostatic adsorption.
3. **Adsorption at optimal pH**: Once the optimal pH is determined, this pH is used to adsorb the precursor onto the support followed by subsequent drying and reduction to obtain the metallic nanoparticles.

The SEA process described above is illustrated in Figure 1.3 depicting the adsorption of platinum onto carbon supports. In this case, the support is an activated carbon, DarcoG60 which has been oxidized with nitric acid to yield a low PZC support. The corresponding precursor to be used is then, the cationic complex, Platinum Tetrammine Hydroxide (PTA). The maximum adsorption occurred at a pH of 11 which was used to prepare the catalyst followed by the subsequent drying and reduction.

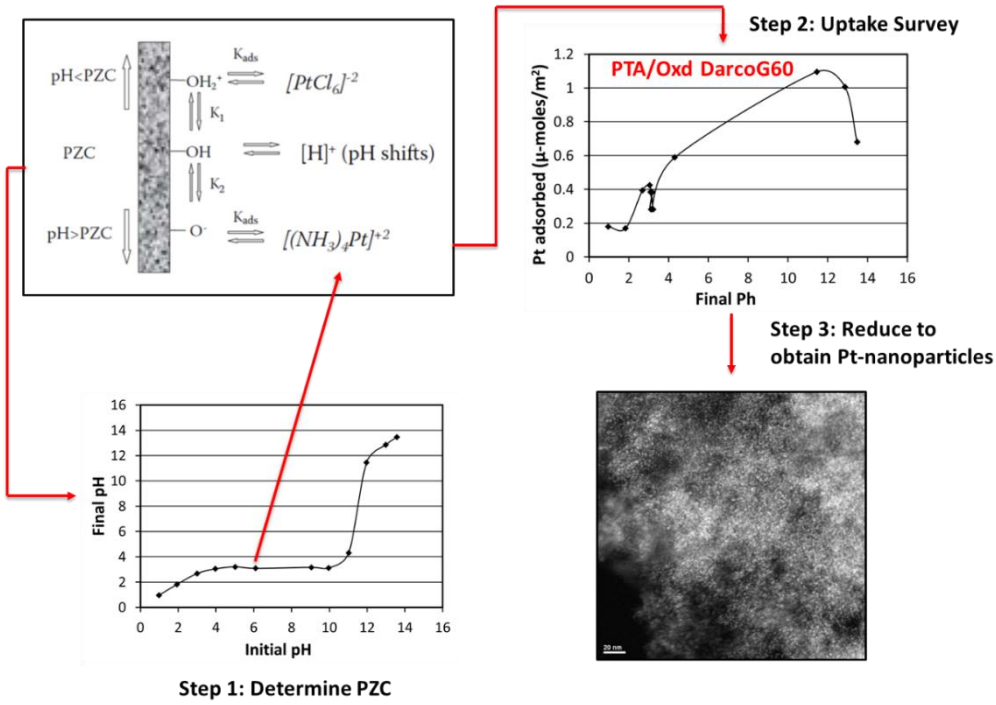

Figure 1.3 Adsorption of platinum on carbon supports by Strong Electrostatic Adsorption

1.4 Metal-Support Interactions

Metal-support interaction has long been the focus of scientific investigations. As mentioned before, supports can play a major role in hindering or favoring the activity of the catalyst. The earliest references of metal-support interactions were recorded in the 1950s. A direct outcome of such interactions may be stabilizing the metal nanoparticles by changing the electronic properties resulting from electron transfer between the metal and support or chemical bonding between metal and support. Schwab [28] discussed in his paper about electron transfer between metal nanoparticles and the support that was attributed to the driving force arising from changes in two Fermi Levels. Another implication of metal support interaction may be hindrance of the chemisorption surface of the metal nanoparticles caused by encapsulation of the metal nanoparticles by the support.

This was shown to be the case for the work of Nerhing and Dreyer [29] where the competitive dehydrogenation versus hydrogenolysis of cyclohexane was greatly favored over Pt/TiO_2 as compared to Pt/Al_2O_3, Pt/MgO, Pt/SiO_2 or Pt/C. In another paper, Pt/C supports have been examined where the metal support interaction was found to be dependent on the amount of surface oxygen groups [30].

In all the previous work, the support functional group compositions are generally analyzed using a combination of Temperature Programmed Desorption (TPD), X-Ray Photoelectron Spectroscopy (XPS) techniques. Different pre-treatment temperatures and functional groups affect the surface acidity as well as the functional group compositions. The catalysts are analyzed using BET Surface area, Transmission Electron Microscopy (TEM), Chemisorption, X-Ray Diffraction (XRD) measurements. As mentioned earlier, the fraction of metal atoms exposed on the surface: referred to as dispersion, is vital in determining the activity of a catalyst in the desired reaction. Dispersion and particle sizes are interchangeable and can be derived from one another if the particle geometry is known. The most common methods in the process are Chemisorption, XRD and TEM. However, it has been noticed that there is a suppression of the chemisorption surface of the Pd metal when carbon supports are used. As a result of this, there is a discrepancy in the Pd particle sizes obtained from chemisorption and XRD/STEM [31-33]. Apart from this noted discrepancy noted in carbon supports, there have also been findings that show that Pt metal nanoparticles, on exposure to air were partially oxidized and the fraction of metallic Pt was dependent on the size of the nanoparticles. For particles lesser than 1.5 nm in size, the Pt supported on silica and alumina were completely oxidized to platinum oxide(PtO) whereas the particles supported on carbon nanotubes existed as a mixture of PtO and metallic

platinum [34,35]. So, there is evidently an electronic or structural contribution from carbon that is responsible for stabilizing the Pt nanoparticles. In both cases, metal-support interactions are thought responsible for the observed phenomenon.

In view of all these discussions, the objective of this thesis is to study the effect on Pt and Pd nanoparticle size, phase and metal oxidation state of the various aspects of carbon, exploring the effect of surface area, surface functional groups, point of zero charge, etc. With this research, we hope to provide insight into three main areas: 1) an explanation of the observed particle size discrepancy between XRD/STEM and chemisorption in carbon supported palladium, 2) an understanding of the stabilizing mechanism of carbon in preventing the oxidation of ultrasmall metal nanoparticles vis-à-vis oxide supports, and 3) the application of the SEA method to specialty carbons such as nanotubes and nanofibers.

CHAPTER 2

CARBON DECORATION IN SUPPORTED PALLADIUM CATALYSTS: DISCREPANCY IN CHEMISORPTION AND STEM PARTICLE SIZES

2.1 Introduction

The key to designing effective catalysts is to maximize the number of active sites on the metallic surface so as to increase the effective surface area for adsorption of reactant gases during heterogeneous catalysis reactions. However, it has been noticed in the literature that during the preparation of catalysts on carbon supports that the chemisorption of hydrogen was substantially suppressed on the catalysts leading to a disagreement between particle sizes obtained by STEM/XRD and chemisorption [31, 33]. Krishnakutty and Vannice have the same observations for Pd dispersed on carbon black and attributed the suppression of hydrogen chemisorption to carbon contamination [33]. It was suggested that during the pre-treatment and synthesis, the C-atoms are found to occupy both the bulk interstitial and surface sites of the Pd nanoparticles. Some of this occurred due to the decomposition of the $Pd(acac)_2$ precursor decomposition while for some other cases, the pretreatment and synthesis steps were responsible for the carbon migration from the support. Five different types of Pd particles were proposed based on this theory, Figure 2.1: Type A: clean Pd particles that were free of bulk and surface carbon impurities, Type B: Pd particles completely encapsulated by carbon and incapable of adsorbing any hydrogen during chemisorption, Type C: Pd particles partially covered by carbon as well as having interstitial carbon exhibiting suppressed hydrogen chemisorption, Type D: Pd particles partially covered by carbon but with no interstitial carbon and Type E: Pd particles with clean surfaces but with interstitial carbon resulting in normal chemisorption.

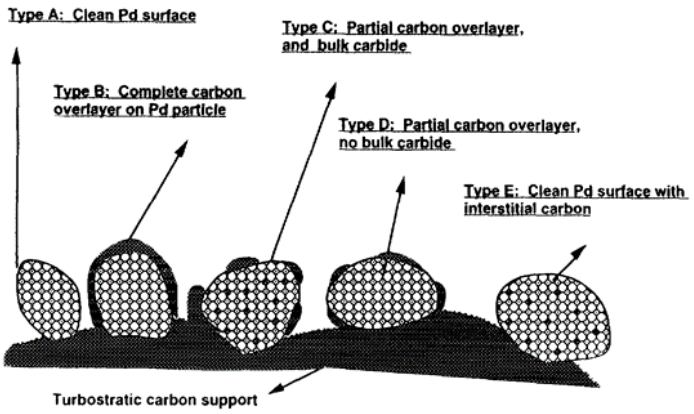

Figure 2.1 Pd particles on a high surface area carbon

The chemisorption and XRD/STEM discrepancy was also studied in some detail by the Regalbuto research group in a series of carbon supported Pd catalysts [31]. As seen from Figure 2.2, there is almost always a difference in the sizes between transmission electron microscopy (TEM)/X-ray diffraction (XRD) and chemisorption. Although this discrepancy has been more commonly noticed in carbon supported palladium nanoparticles, it has also been seen in platinum and ruthenium nanoparticles supported on carbon.

Carbon supported catalysts exhibiting a discrepancy between bulk sizing methods (XRD and/or EM) and chemisorption estimated particle size.

Catalyst system[a]	Metal loading (%)	Chemisorption size (nm)	XRD size (nm)	EM size (nm)
Pd/AC	7.8	131	20	49[b]
Pd/Graphite	8.5	57	25	24[b]
Pd/GNF	8.7	75	23	37[b]
Pd_{10Med}/C_{PPh2}	1.7	5.7	–	1–2
Pd_{12Med}/C_{PPh2}	2.1	12.8	–	2
Pd/C	5	8.5	6.7	5.9
CNF-Pt	2	4	v.s.[c]	–
CNF-Pd	2	18	13.6[d]	–
CNF-Ru	2	20	v.s.[c]	–
Pt/VC	19.2	12	2.7	2.2
Pt/VM	20	24	5.4	5.3

Figure 2.2 Discrepancy between Chemisorption and STEM Sizes [31]

In the same work, a series of carbon supported Pd nanoparticles with different pretreatments was prepared and analyzed using Temperature Programmed Oxidation. The TPO studies were based on the hypothesis that during the preparation process, the metal surface becomes coated with a partial or complete overlayer of carbon that blocks the active metallic sites for adsorption. Hence, the study aimed at designing an effective method for removing this surface carbon to expose the active metallic sites and recover the metal surface. Since the surface carbon on the palladium nanoparticles will burn off at lower temperatures compared to the bulk carbon support during the heat treatment in oxygen, oxidation peaks distinct from high temperature bulk carbon burn off were observed for all samples at around 250°C and 320°C [Figure 2.3]. The lower temperature of 250℃ was related to the surface carbon burn off while the higher temperature of 320℃ was attributed to the sub-surface carbon which would be more difficult to burn off compared to the surface carbon. A short oxidation at the latter temperature removed the decorating layer as the TPO peaks disappeared and the reduced metal surface was found to chemisorb at close to the expected capacity.

An additional observation from Figure 2.3 is that the carbon burn off peaks become less apparent with decrease in the size of the nanoparticles which is probably due to the smaller perimeters of carbon decoration. Secondly, for the smallest nanoparticle (4.6 nm), the intensity of the sub-surface carbon burn off peak is substantially higher than the surface carbon indicating that there is more sub-surface carbon as the particle size decreases.

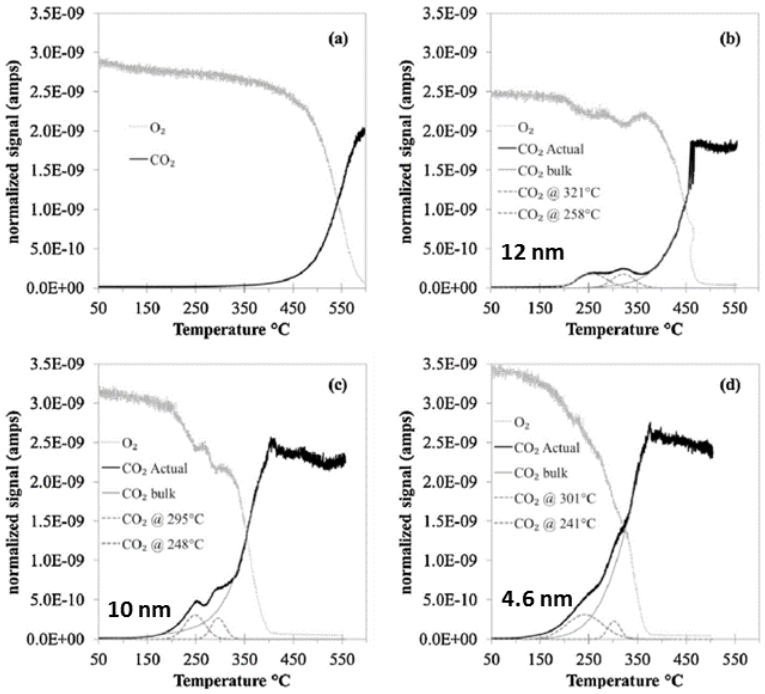

Figure 2.3 TPO profiles: (a) CP-97 carbon support control experiment, (b) Pd/CP97, (c) Pd/CP97-A, (d) Pd/CP97-C

Hence, in lieu of these preliminary studies, the purpose of this work was to perform a more systematic study to understand the effect of pre-treatment process, surface functionalization, precursors used and types of carbon supports on this discrepancy. The the goal of this section of the research is to employ different types of carbon originating from different sources: carbon black, activated carbon, graphitic carbon, etc. and subject them to different pretreatment and oxidizing conditions thereby modifying their surface functionalities and composition. Strong Electrostatic Adsorption (SEA) using different precursors (chloride and nitrate counter-ions) will be used followed to synthesize the metal nanoparticles. Once the metal particles supported on the carbon supports are obtained, the finished products will be subjected to an oxidative environment by ramping up the temperature. This process will burn off any surface carbon and we hope to recover the surface of the metal for hydrogen chemisorption.

2.2 Experimental

2.2.1 Pretreatments of carbon supports and PZC determination

With a target to studying the different types of carbon supports, a carbon black (VXC72) and activated carbon (DarcoG60) were chosen. The VXC72 and DarcoG60 carbons were obtained from Cabot Corporation. The carbons were first oxidized prepared by boiling them in nitric acid (>70%) at 90°C for 3 hours and cooling to room temperature. The mixture was filtered and washed with deionized (DI) water until the pH of the washing solutions reached that of DI water and was dried overnight at room temperature. This was then followed by heat treating each of the oxidized and uoxidized carbons to 300℃, 600℃ and 1000℃ for 16 hrs. The BET surface areas were determined from nitrogen adsorption-desorption isotherms with a Micromeritics 2020 ASAP instrument.

The point of zero charge (PZC) was determined with a pH probe by measuring the initial and final pH of a series of thick slurries at high surface loadings which generally gives a wide plateau over which the final pH remains constant even as the initial pH changes [36]. This constant pH reflects the PZC of the supports. Based on the PZC of the support, cationic or anionic precursors were chosen as is the standard protocol for performing strong electrostatic adsorption (SEA). For the low PZC oxidized VXC72 and Darco, the cationic precursor, tetraamminepalladium(II) chloride (PdTA, $[Pd(NH_3)_4]Cl_2$, Sima-Aldrich 99.999%) was used and for the high PZC unoxidized VXC72 and DarcoG60, palladium(II) chloride, $PdCl_2$ stabilized with excess HCl (PdTC, $[PdCl_4]^{2-}$, Sigma-Aldrich 99.9%) was used as the anionic precursor. Table 2.1 shows the pretreatment for the two types of carbon along with the corresponding BET surface areas, PZC and precursors used.

In order to study the effect of non-choride precursors on the types of carbon, a Timcal Timrex HSAG300 graphitic carbon was used along with oxidized VXC72and oxidized DarcoG60. Tetraamminepalladium(II) nitrate (PdTA, $[Pd(NH_3)_4](NO_3)_2$, Sima-Aldrich 99.999%) was used as the non-chloride precursor on the low PZC supports.

Table 2.1 Pretreatment, PZCs and surface areas of (a) VXC72 (b) DarcoG60

(a)

Treatment	Oxidized	PZC	Precursor	BET SA (m^2/gm)
Untreated	No	8.2	Palladium Tetrachloride	231
Heat 300°C	No	8.3		201
Heat 600°C	No	8.3		227
Heat 1000°C	No	10		183
Untreated	Yes	2.3	Palladium Tetrammine	185
Heat 300°C	Yes	2.3		220
Heat 600°C	Yes	2.3		232
Heat 1000°C	Yes	2.5		150

(b)

Treatment	Oxidized	PZC	Precursor	BET SA (m^2/gm)
Untreated	No	8.1	Palladium Tetrachloride	627
Heat 300°C	No	9.1		649
Heat 600°C	No	10.2		702
Heat 1000°C	No	11.1		683
Untreated	Yes	1.7	Palladium Tetrammine	599
Heat 300°C	Yes	2.8		559
Heat 600°C	Yes	3.2		654
Heat 1000°C	Yes	3.8		589

2.2.2 X-Ray Photoelectron Spectroscopy (XPS) of supports

An XPS analysis was performed on the bare supports that were unoxidized or oxidized as well as heat treated to probe their surface composition. XPS measurements were conducted using a Kratos AXIS Ultra DLD XPS system equipped with a monochromatic Al K source. The monochromatic Al K source was operated at 15 keV and 120 W. For all the supports, the survey scan and O1s signals were primarily monitored. The peak position and peak area obtained from XPS are used to evaluate the composition, while the peak shape provides the information about chemical shifts or chemical bonds of the elements.

2.2.3 Adsorption surveys and catalyst preparation

Adsorption surveys were conducted for all the series of oxidized, heat treated samples after the precursors were chosen based on the PZC. Solutions over an entire range of pH (1-14) were prepared at the required concentration (200 ppm). The high PZC unoxidized supports were weighed out to obtain the desired 500 m^2/L surface loading and the low PZC oxidized supports weighed out for 1000 m^2/L and added to the solutions which were shaken vigorously for about an hour. The solutions were then, filtered into centrifuge tubes and initial and final concentrations were determined in an ICP-OES. The difference in the concentrations provided a measure of the uptake of palladium. Once the optimal pH of adsorption was determined, the supported Pd catalyst was prepared with a metal loading of 2.5 wt% for the unoxidized VXC72 and a weight loading of 10-11 wt% for the unoxidized and oxidized Darco. This was followed by oven drying in static air at 120°C for 16 hrs and then, reduction at 150-180°C in flowing10% H_2 balance He for 1 hr at

determined from temperature programmed reduction with a ramp rate of 2.5°C/min.

2.2.4 Catalyst characterization

The supported catalysts were then characterized to determine the particle sizes using X-RAY Diffraction (XRD), Scanning Transmission Electron Microscopy (STEM) and Chemisorption. A Rigaku Miniflex-II equipped with a D/teX Ultra silicon strip detector was used to perform powder XRD on the supported Pt particles. Diffraction patterns were recorded over a range of 10°–80° 2Θ using Cu-Kα radiation (k = 1.5406 Å) that was operated at 30 mA and 15 kV [37]. XRD patterns were obtained for all metal free supports in addition to the supported metals. Background stripping and deconvolution of peaks contributed by Pd and carbon support were done in PDXL 2.0 provided by Rigaku, using Split Pseudo-Voigt function for the peaks. The full width at half maximum (FWHM) values were input together with a shape factor of 0.94 in the Scherrer equation to estimate particle size.

The Aberration-corrected JEOL 2100F scanning trans-mission electron microscopy (STEM) was used to do Z-contrast imaging. Sample preparation involved ultrasonicating the sample in ethanol and adding a drop to a copper TEM grid with a thin holey carbon coating.

Pulse Chemisorption of the samples was performed using Autochem 2020. The process involved hydrogen titration of oxygen pre-covered Pd surfaces. A pretreatment step included drying at 120℃ followed by reduction in 10% hydrogen at 200℃. The catalyst was then contacted with 10% oxygen in helium at40℃ for 30 min to oxidize the surface Pd to PdO. Then, it was titrated with pulsed 10% hydrogen in argon to form water and surface Pd with chemisorbed hydrogen. The assumed overall stoichiometry is 0.667

Pd:1 H_2. Particle sizes were estimated from chemisorption assuming hemispherical geometry. Since chemisorption is a surface technique, it is compared to surface average STEM sizes and XRD, being a volume /bulk technique is compared to the volume average STEM sizes.

2.2.5 Temperature Programmed Oxidation (TPO) for palladium surface recovery

A custom TPX System fitted with an Inficon Transpector 2 Mass Spectrometer was used to perform TPO studies. The catalyst samples were loaded and a moisture removal pretreatment was introduced at 120℃ in flowing He till the water signals levelled out and diminishes. Following this, TPO was done by flowing 10% oxygen in helium at 20 sccm while heating the catalysts to a temperature of 450℃ with a ramp of 5◦C/min. The carbon dioxide and oxygen signals were primarily monitored and the spectrum from 1-50 amu was recorded. A control TPO experiment using only the support was also carried out using the same conditions for comparison. Once the optimum TPO conditions were determined, an additional step was introduced in the chemisorption protocol only for the as-required catalysts for burning off the surface carbon on the palladium metal nanoparticles [31].

2.3 Results and Discussion

2.3.1 PZC variations with pretreatment temperatures

As observed from Table 2.1, both the process of surface oxidation as well as heat treating the carbons to various temperatures alters the PZC. While surface oxidation for both the VXC72 and the DarcoG60 decreases the PZC, heating the carbons seems to increase the PZCs. In order to understand the PZC variations, XPS experiments were performed on all the carbons as mentioned earlier and the survey spectrum and O1s signals

were primarily observed. Fig 2.4 shows that for the carbon blacks, increasing the pretreatment temperature to 300˚C initially decreases the surface oxygen content but further heating to 600˚C increases the surface oxygen concentration. This may be due to bulk oxygen trapped in the carbon lattice that reaches the surface during the heat treatments. However, further increase to 1000˚C causes a decrease in the oxygen content. Oxidizing the carbon however causes a considerable increase in the oxygen content that can be directly linked to the decrease in PZC due to the increased acidic oxygen functionalities on the surface. For both the oxidized and unoxidized VXC72, heating upto 1000˚C for 16 hrs decreases the oxygen content. It is observed that removal of surface oxygen has a direct effect on increasing the PZC for the VXC72 which is more dramatic for the unoxidized VXC72. A separate heat treatment was conducted for the unoxidized VXC72 by heating in 1000˚C for 32 hrs which was found to remove the surface oxygen completely. This net decrease in oxygen content with increase in pretreatment temperatures is true for all the carbons, oxidized or un-oxidized. As has been observed numerable times in the literature, this decrease in surface oxygen content can be related to increases in the PZC [38].

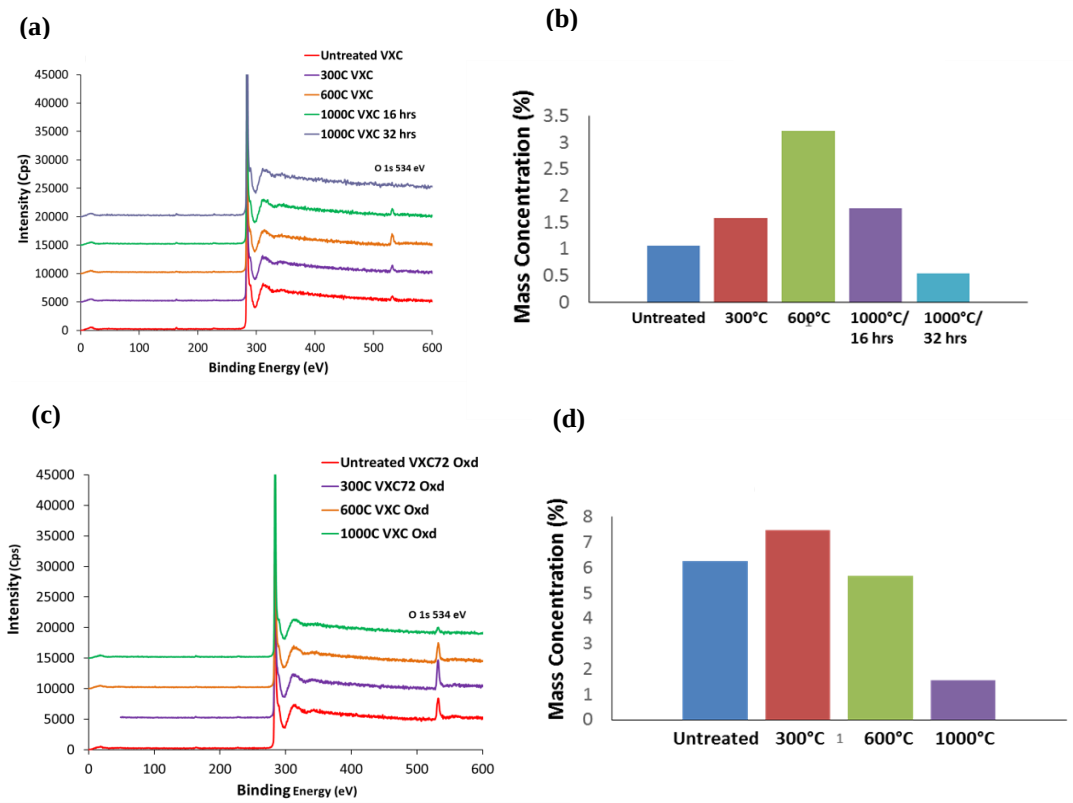

Figure 2.4 (a) XPS survey spectrum (b) Mass concentration of oxygen of unoxidized VXC72 and (c) XPS survey spectrum (d) Mass concentration of oxygen of oxidized VXC72

Figure 2.5 similarly shows the same trends for the activated carbon, DarcoG60. Similarly, it is noticed that heat treatment for the DarcoG60 increases the PZC dramatically. It is seen that for the activated carbons, there is a dramatic decrease in the surface oxygen content on heating which makes the surface less acidic and in the process, increases the PZC. It is also noticed that the change in PZC with surface oxygen content is more pronounced in the case of Darco as compared to the VXC72.

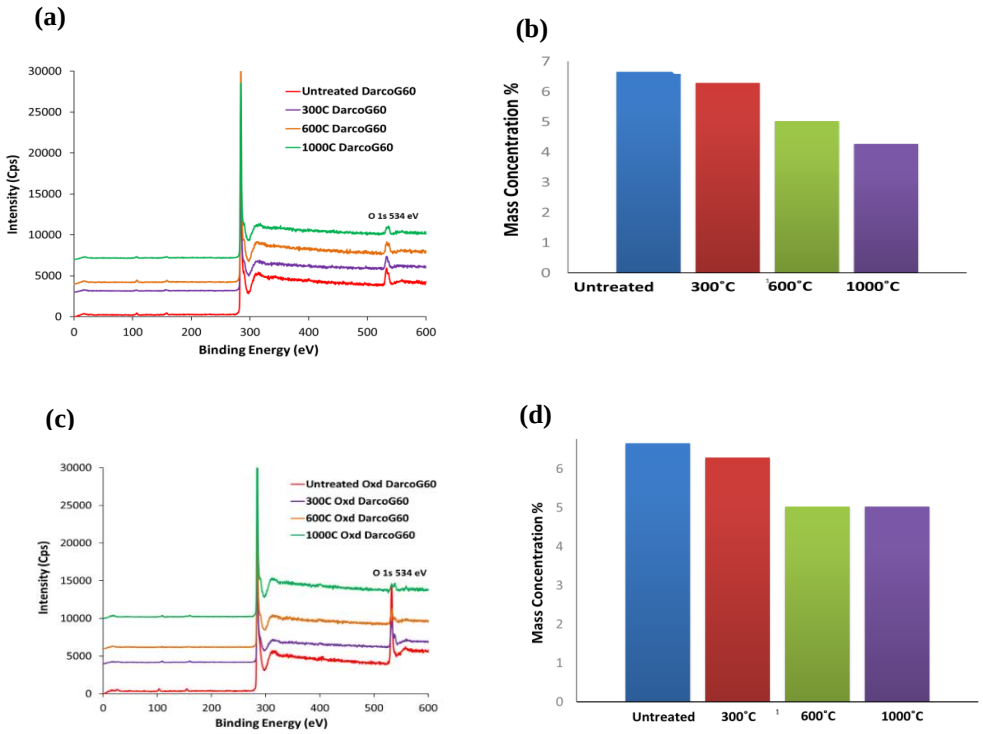

Figure 2.5 (a) XPS survey spectrum (b) Mass concentration of oxygen of un-oxidized DarcoG60 and (c) XPS survey spectrum (d) Mass concentration of oxygen of oxidized DarcoG60

2.3.2 Trends in adsorption surveys

Once the surface areas and PZC of the support are determined, a precursor is chosen and uptake experiments are performed to determine the maximum adsorption pH. As expected, the uptake for all the series of carbons using SEA was volcanic in nature: the uptake increased as the pH was moved further away from the PZC but decreased at high pH due to high ionic strength. Also, for each of the unoxidized VXC72 and DarcoG60, the uptake did not change much with pretreatment temperature, Figure 2.6 yielding similar metal loadings. The color codes in the plot designate the pretreatment temperatures.

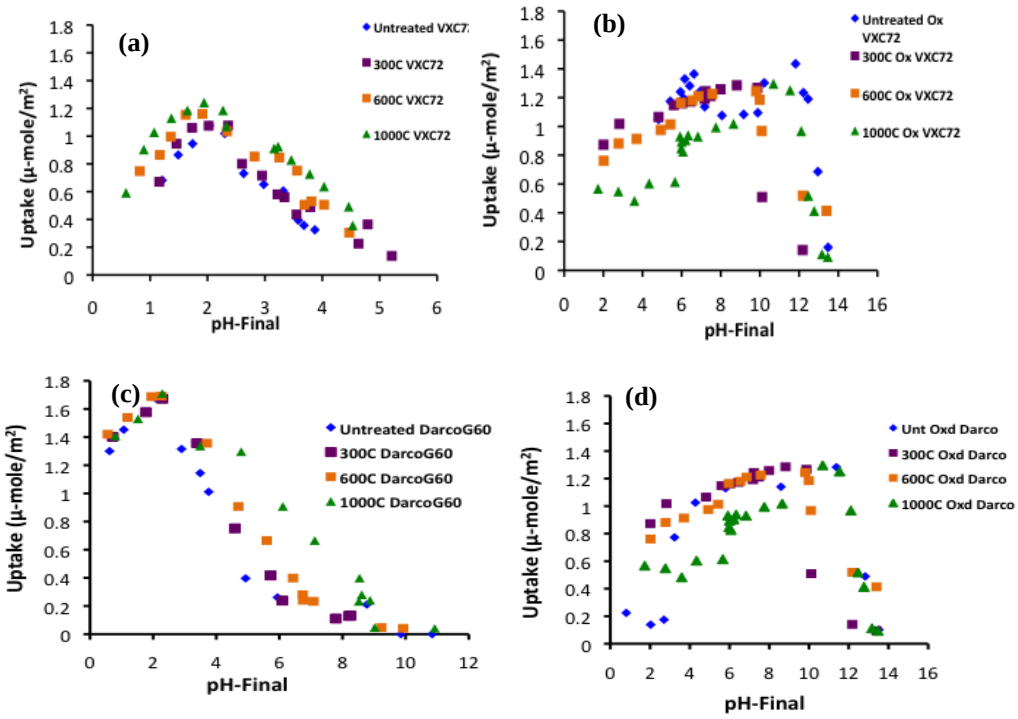

Figure 2.6 Uptake Plots (a) Unoxd VXC72 (b) Oxd VXC72 (c) Unoxd Darco (d) Oxd Darco

2.3.3 Understanding the STEM/Chemisorption discrepancy

Once the optimal pH of adsorption was determined, the supported Pd catalyst was prepared with a metal loading of 2.5 wt% for the unoxidized VXC72 and a weight loading of 10-11 wt% for the unoxidized and oxidized Darco. This was followed by drying at 110°C overnight and reduction at 150-180°C in 10% flowing hydrogen to yield the metal nanoparticles. The reduction temperatures were determined by conducting Temperature Programmed Reduction (TPR) experiments on the series of carbon. The figures 2.7-2.10 below shows the STEM images for the series of carbons along with their particle sizes. Fig 2.11 are the XRD patterns of the same.

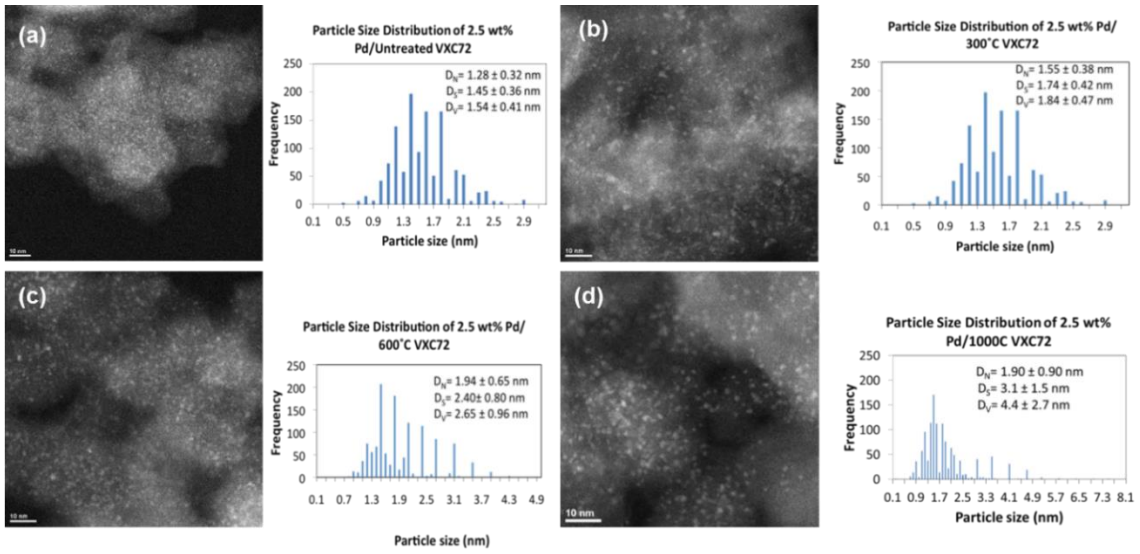

Figure 2.7 STEM images for unoxidized VXC72 (a) without pretreatment (b) heat treatment at 300˚C (c) at 600 ˚C and (d) 1000 ˚C

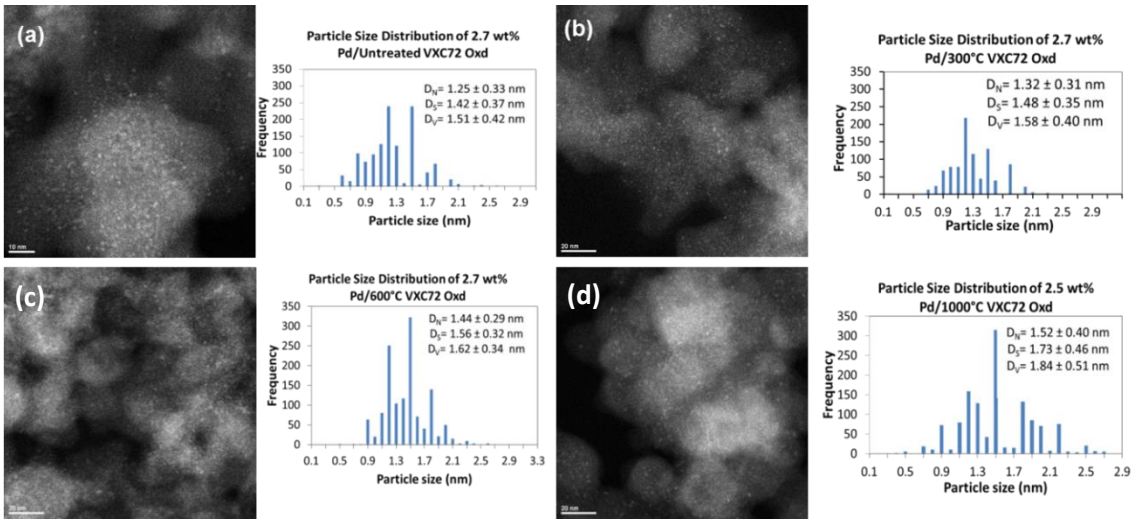

Figure 2.8 STEM images for oxidized VXC72 (a) without pretreatment (b) heat treatment at 300˚C (c) at 600 ˚C and (d) 1000 ˚C

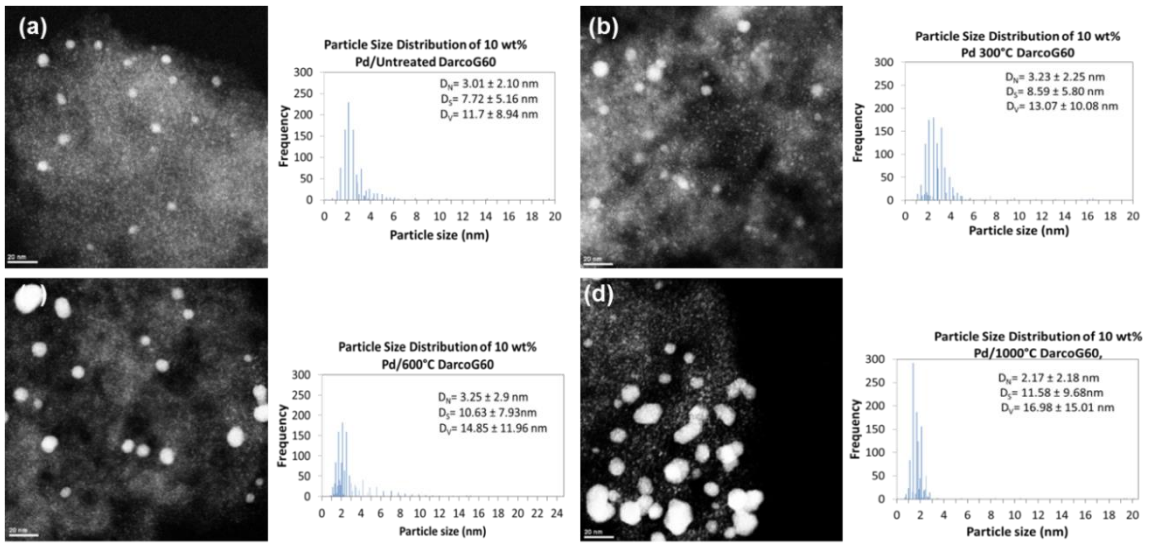

Figure 2.9 STEM images for unoxidized Darco (a) without pretreatment (b) heat treatment at 300˚C (c) at 600 ˚C and (d) 1000 ˚C

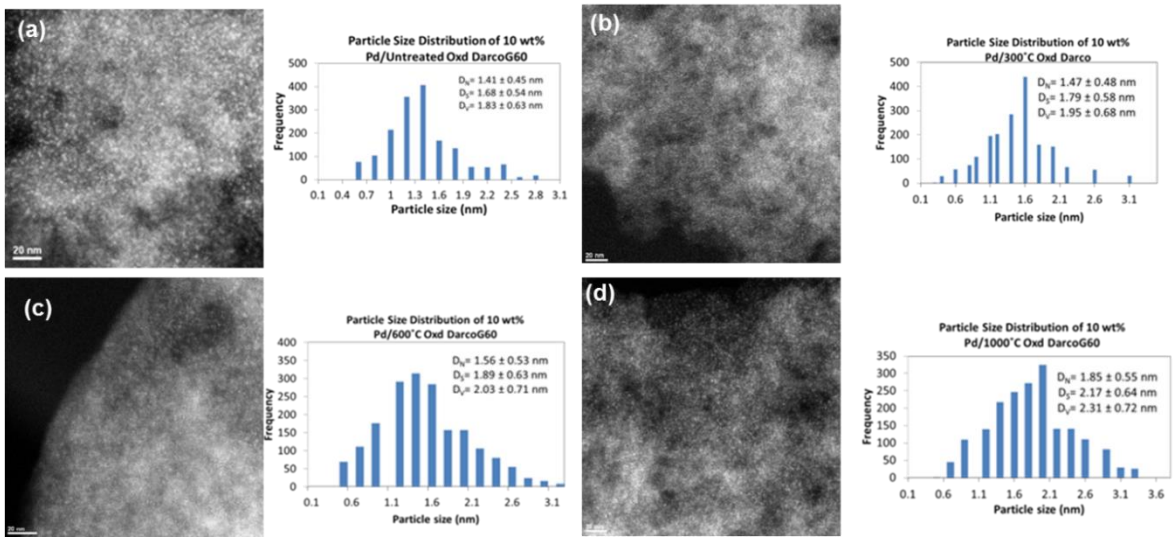

Figure 2.10 STEM images for oxidized Darco (a) without pretreatment (b) heat treatment at 300˚C (c) at 600 ˚C and (d) 1000 ˚C

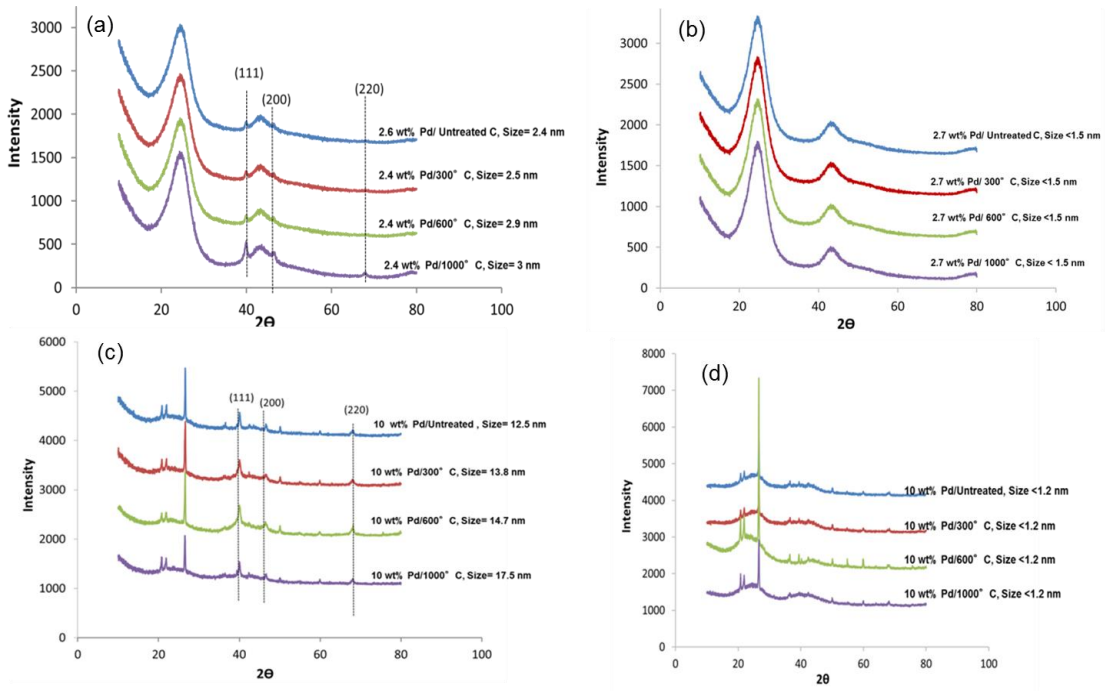

Figure 2.11 XRD patterns for (a) unoxidized VXC72 (b) oxidized VXC72 (c) unoxidized Darco and (d) oxidized Darco

From the characterization, it is evident that XRD and STEM volume average sizes match fairly well with each other. All the carbons except the unoxidized Darco series gave small particles that were 2.5 nm or lesser in size. Unexpectedly, the entire series of heat treated unoxidized Darco gave large particles with wide standard deviations. For each of the carbons, increase in pre-treatment temperatures from room temperature to 100℃ led to an increase in particle size. This can be related to the decrease in the oxygen groups on the surface with increasing heat treatment as observed in the XPS plots (Figure 2.5) which causes sintering of the particles.

Both XRD and STEM confirmed that large particles with wide standard deviations were obtained for the unoxidized Darco (Figures 2.9 and 2.11c). However, as soon as the support is oxidized, the particle sizes decrease [Figures 2.10 and 2.11d]. To check if the

pore structure of unoxidized Darco had an affect on the large particle size, a pore analysis study was conducted. It was found that both the oxidized and unoxidized Darco were predominantly microporous. Heat treatment of the unoxidized Darco does not change the pore size distribution or the micropore volume, area etc. The average pore width was 2.3 nm and remained the same after oxidation. So, it is not apparent from this study that pore size can have an effect on the particle size for the unoxidized Darco. Figure 2.12 shows the pore size distribution of unoxidized and oxidized Darco.

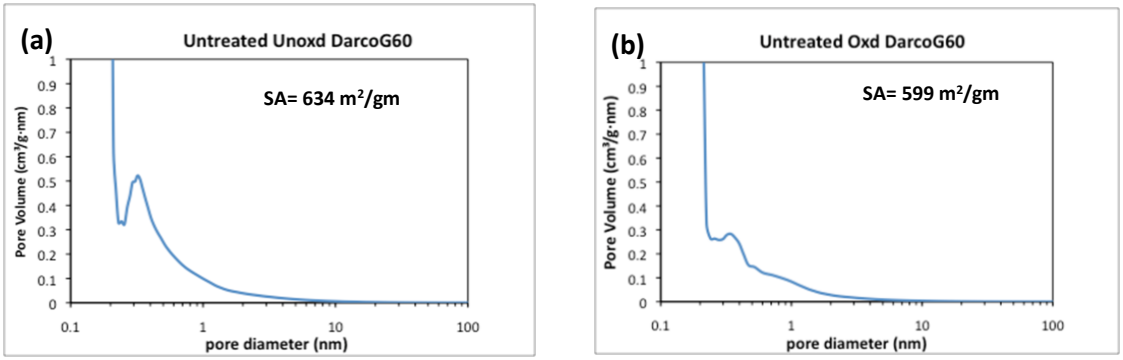

Figure 2.12 Pore distribution for (a) unoxidized (b) oxidized Darco

The other hypothesis at hand to explain the large particle sizes of Darco is the phenomenon of deposition precipitation at the surface of the Darco. It has been seen in the literature [38] that although the global pH of the solution may be regulated, the local pH in the vicinity of a surface may increase due to interactions between the complex precursor ion species (in this case, $PdCl_4^{2-}$) leading to a protonation of the support surface. This local pH increase may cause the complex ion to deposit on the support leading to larger particles. Hence, in this case, a greater amount of HCl may be required to stabilize the PdTC complex in solution.

Table 2.2a and b shows a comparison of the particle sizes for the two types of carbons. It can be clearly seen that XRD and STEM volume average sizes are not in unreasonable agreement. However, there appears to be a substantial disagreement between Chemisorption and STEM surface average sizes. The chemisorption sizes are seen to be larger than the STEM surface average sizes which indicates that the active sites in the metal nanoparticles are blocked and this causes a suppression of the oxygen-hydrogen chemisorption, thus, leading to larger particle size estimates.

Table 2.2 Particle size from XRD, Chemisorption and STEM for VXC72 and DarcoG60

Carbon Type	Pretreatment Temperature (˚C)	XRD Particle Sizes (nm)	STEM Volume Average Particle Sizes (nm)	Chemisorption Particle Sizes (nm)	STEM Surface Average Particle Sizes (nm)
Un-oxidized VXC	0	2.4	1.5 ± 0.4	3.3	1.5 ± 0.4
	300	2.5	1.8 ± 0.4	3.5	1.7 ± 0.4
	600	2.9	2.7 ± 0.9	3.6	2.4 ± 0.8
	1000	3	4.4 ± 2.7	3.9	3.1 ± 1.5
Oxidized VXC	0	<1.5	1.5 ± 0.4	6.3	1.4 ± 0.4
	300	<1.5	1.6 ± 0.4	6.4	1.5 ± 0.4
	600	<1.5	1.6 ± 0.3	6.4	1.6 ± 0.3
	1000	<1.5	1.9 ± 0.5	6.5	1.8 ± 0.5
Un-oxidized Darco	0	12.5	11.7 ± 8.9	8.1	7.7 ± 5.2
	300	13.8	13.1 ± 10.1	8.6	8.6 ± 5.8
	600	14.7	14.9 ± 11.9	11.4	10.6 ± 7.9
	1000	17.5	16.9 ± 15.0	12.6	11.6 ± 9.7
Oxidized Darco	0	<1.5	1.8 ± 0.6	3.2	1.7 ± 0.5
	300	<1.5	1.9 ± 0.7	3.5	1.8 ± 0.6
	600	<1.5	2.0 ± 0.7	3.9	1.9 ± 0.6
	1000	<1.5	2.3 ± 0.7	4.1	2.2 ± 0.6

In order to develop a better understanding of this discrepancy and relate it to the surface oxygen groups and pre-treatment conditions, a ratio of the Chemisorption derived and STEM Surface average sizes was plotted for the different carbons against the pre-

treatment temperatures in Figure 2.13. In the figure, the straight line at the STEM/Chemisorption ratio of 1 depicts the ideal No-discrepancy line. Any points above this line would then, be related to higher chemisorption values than STEM and thus, show the level of discrepancy. It is observed that the discrepancy for both the carbons: VXC72 and DarcoG60 is the highest when they are oxidized. It is also seen that increase in pretreatment temperature for each of the oxidized and un-oxidized series decreases the discrepancy. The latter observation agrees well with the former in that the amount of oxygen groups on the surface decreases with increase in heat treatment temperatures [Figure 2.5] and hence, the lesser oxidized carbons show lower amount of discrepancy. The reason behind the greater discrepancy exhibited by oxidized carbons may be attributed to the lone pair of electrons around the C=O bonds (in carboxylic acid or anhydride groups) that are shared with the 4d orbitals of the Pd leading to strong Pd-C interaction that enhances the carbon decoration [39].

An additional observation is that the unoxidized Darco that gave large particles with wide standard deviations did not show any discrepancy. This is probably due to the higher activation energy required for diffusion of carbon atoms onto the surface of large palladium nanoparticles as compared to smaller ones. It was also observed that the degree of discrepancy was the highest for VXC72 (carbon black) than the DarcoG60 (activated carbon). The effect of carbon support to the degree of discrepancy will be discussed in detail later.

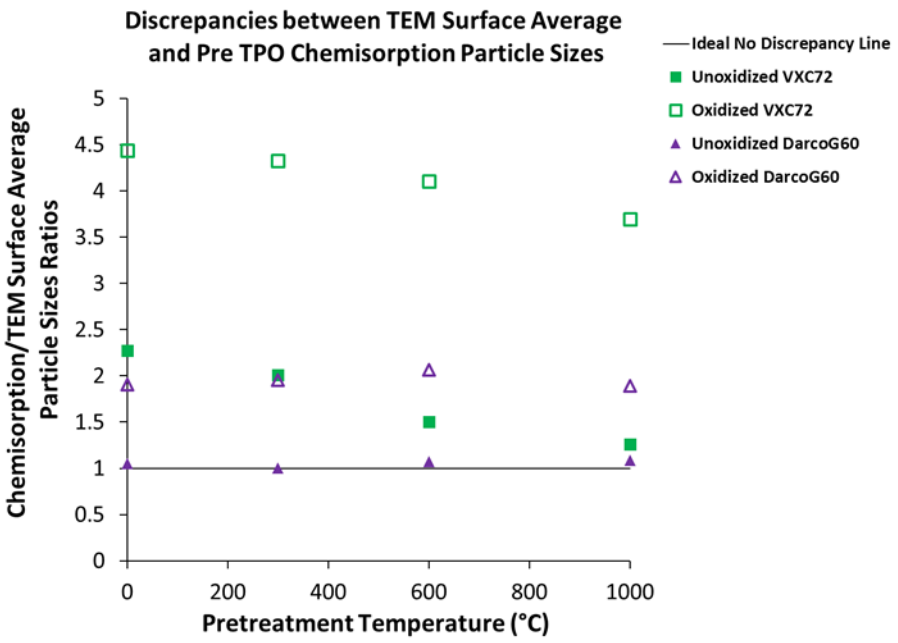

Figure 2.13 Pre TPO Chemisorption/STEM particle sizes variations with temperature: showing the discrepancy

The next step was to resolve the discrepancy between the two characterization techniques and based on the previous work [31], it was inferred that if there is a carbon layer on the surface or subsurface, we should be able to burn off the layer with treatment in oxygen while ramping up the temperature. The basis of these studies is that the carbon layer on the palladium metal surface will burn off at a lower temperature when compared to the carbon from the bulk carbon support. TPO studies were thus, conducted on all the series of supported Darco and VXC72 samples. The catalyst samples were loaded in a custom TPX System fitted with an Inficon Transpector 2 Mass Spectrometer. Moisture was removed by heating at 200◦C and flowing He, until the water signal is diminished. TPO was done immediately afterwards, with a ramp of 5◦C/min, flowing 10% oxygen in helium at 20 sccm. Figure 2.14 shows two representative plots for TPO studies conducted on the highest (2.5%Pd/ untreated oxd VXC72) and lowest (10%Pd/ Unoxd Darco) discrepancy

samples. Figure 2.14a and c are the two control experiments showing the TPO experiments done on VXC72 and DarcoG60 respectively without ant metal to show the bulk carbon burn offs. The red curves designate the oxygen that is being consumed during the reaction and the purple curves are due to the carbon dioxide burn offs. The bulk carbon is seen to burn off at about 220℃ for both the carbons. Figures 2.14b and d show the TPO peaks for the two catalysts. As was seen in prior TPO studies in the group, Fig 2.3 (b, c and d), there were two distinct burn off peaks noted for carbon dioxide at 250°C and 320°C which decreased with the particle sizes and was much less apparent for the smallest particles of 4.6 nm shown in Fig 2.3d. Following the same trend, it is seen that in Figure 2.14b (2.5%Pd/untreated oxidized VXC72), the carbon burn off peaks are not apparent since the particle sizes are too small (<2.5nm). However, there is oxygen consumption at 275°C which shows that there is carbon dioxide formed. An explanation for this may be that there is very little carbon on the metal surface but most of it may probably be on the sub surface. The sub surface carbon burns off at a higher temperature than the surface carbon as expected. As seen from Table 2.2, no discrepancy was expected from the unoxidized Darco that formed the large particles (>12 nm) because the STEM surface average values agreed pretty well with the chemisorption sizes. This was confirmed by TPO studies that showed no surface or sub surface carbon dioxide emission during the TPO (Fig 2.14d).

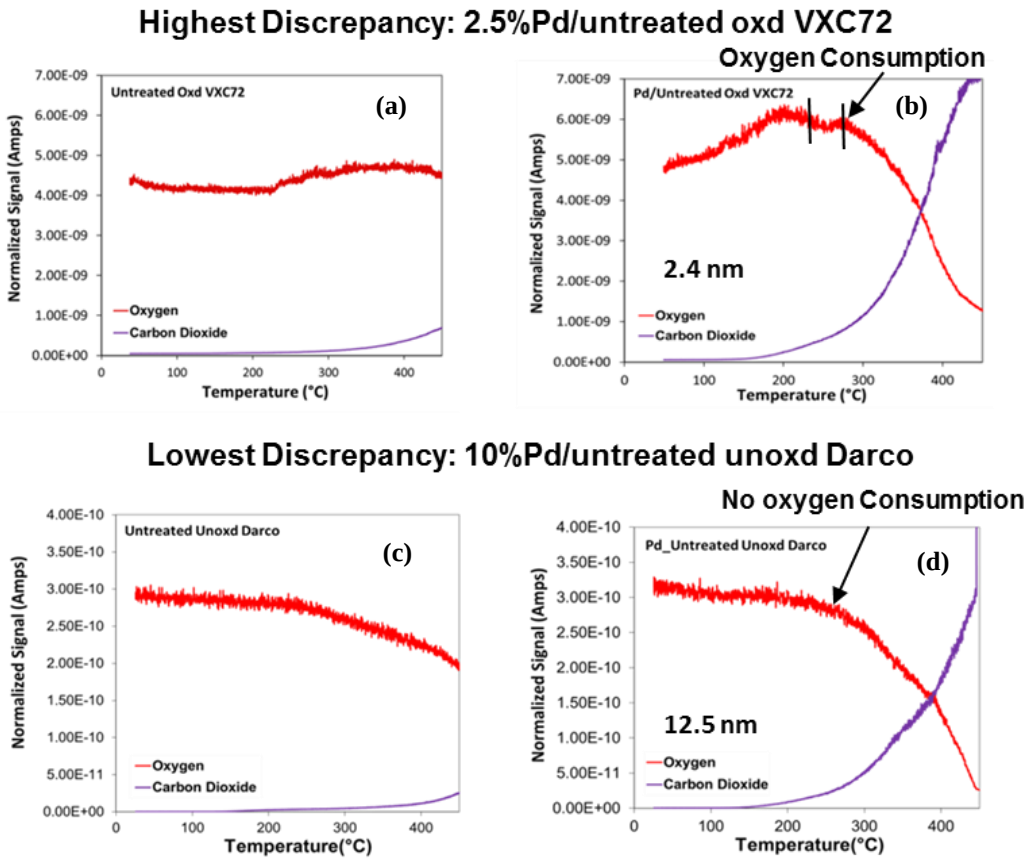

Figure 2.14 Temperature Programmed Oxidation (TPO) studies for (a) oxd VXC72 (control experiment) (b) Pd/oxd VXC72 (c) unoxd Darco (control experiment) (d) Pd/unoxd Darco

Table 2.3 below shows the post TPO changes in chemisorption particle sizes after the TPO treatments. The post TPO chemisorption sizes decrease for all the catalysts and the decrease is about 50-60% for the highest discrepancy oxidized VXC72 samples. This confirms again that although the carbon burn offs were not apparent in Figure 2.14b, there was a carbon layer that was burnt off during the TPO. For the unoxidized Darco samples, there was no change in the sizes since the discrepancy did not exist.

Table 2.3 Pre and Post TPO Chemisorption sizes and their comparison with STEM sizes for VXC72 and DarcoG60

Carbon Type	Pretreatment Temperature (℃)	Pre-TPO Chemisorption Size (nm)	Post TPO Chemisorption Size (nm)	STEM Surface Average Particle Sizes (nm)
Unoxidized VXC	0	3.3	3.5	1.5 ± 0.4
	300	3.5	2.4	1.7 ± 0.4
	600	3.6	2.1	2.4 ± 0.8
	1000	3.9	3.1	3.1 ± 1.5
Oxidized VXC	0	6.3	3.8	1.4 ± 0.4
	300	6.4	3.1	1.5 ± 0.4
	600	6.4	2.4	1.6 ± 0.3
	1000	6.5	2.7	1.8 ± 0.5
Unoxidized Darco	0	8.1	7.2	7.7 ± 5.2
	300	8.6	7.3	8.6 ± 5.8
	600	11.4	10.9	10.6 ± 7.9
	1000	12.6	11.1	11.6 ± 9.7
Oxidized Darco	0	3.2	1.4	1.7 ± 0.5
	300	3.5	2	1.8 ± 0.6
	600	3.9	2.2	1.9 ± 0.6
	1000	4.1	2.6	2.2 ± 0.6

This is further confirmed in Figure 2.15 that shows the plot of post TPO Chemisorption-STEM ratios against pre-treatment temperatures. Although the discrepancy reduced after the pretreatment for all the carbons, the decreasing trends with increase in pretreatment temperature is still existent. Although the discrepancy seemed to almost disappear for the oxidized Darco, it was still considerable for the oxidized VXC72. It is seen that burning off the surface carbon does not recover the chemisorption surface completely. It may be possible that there are other factors contributing to the discrepancy.

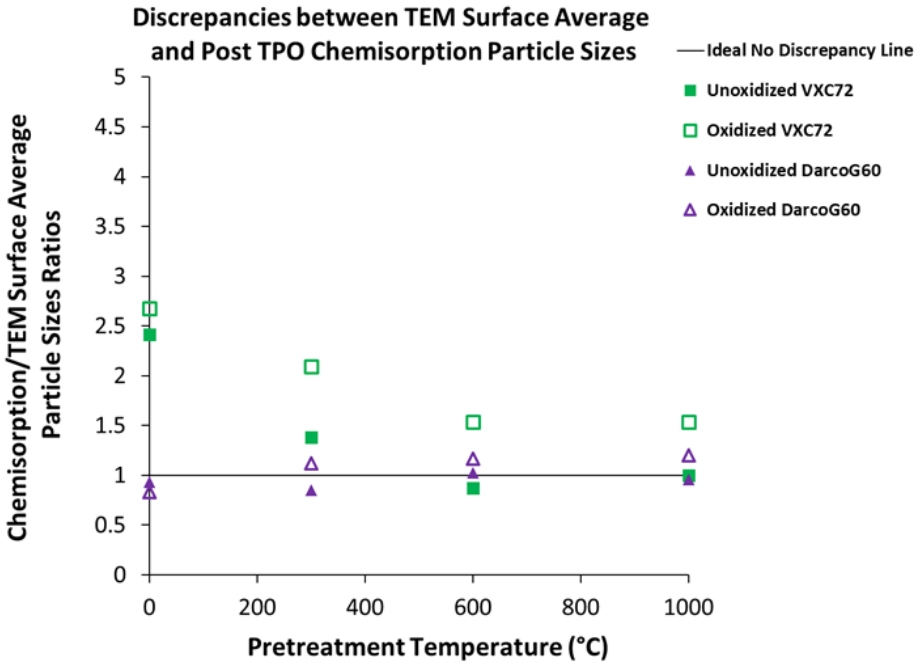

Figure 2.15 Pre TPO Chemisorption/STEM particle sizes variations with temperature: showing the discrepancy

After having looked at the discrepancy in terms of surface oxygen groups and pre-treatment, the next study was conducted to see the effect of using non-chloride precursors to check the effect of chloride contaminating the surface. For this study, three different carbons were selected: oxidized VXC72 (carbon black), oxidized DarcoG60 (activated carbon) and TimrexHSAG300 (graphitic carbon). PdTA (with Cl^- counter-ion) was compared with PdTA (with NO^{3-} counter-ion). Figure 2.16 shows the STEM images of the Pd on the oxd VXC72, oxd Darco and Timrex supports using both the nitrate and chloride pecursors. There was no noticeable differences in the STEM surface average sizes between the using the two different precursors on either of the three supports.

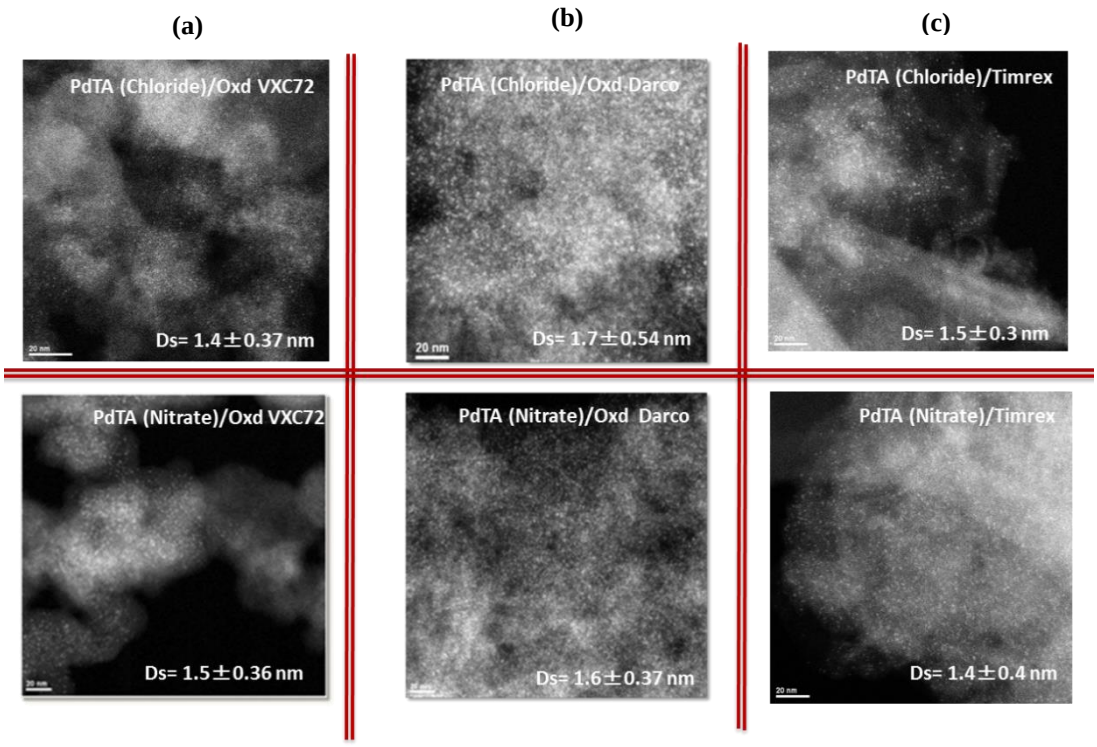

Figure 2.16 STEM images showing surface average sizes for chloride and nitrate precursors on (a) oxidized VXC72 (b) oxidized DarcoG6 and (c) TimtexHSAG300 carbon supports

Figure 2.17 shows a plot of the Chemisorption/STEM ratio for the different types of carbons using the nitrate vs the chloride precursors. For each of the carbons, comparing the pre-TPO chemisorption/STEM ratio shows 20-50% reduction in the discrepancy when using a nitrate precursor as compared to using a chloride precursor. For the chloride precursors used earlier, it was already seen earlier for the oxidized VXC72 and DarcoG60 and in Figure 2.17) that TPO treatment gave a 50% reduction in the discrepancy. This was also seen for the Timrex support where the discrepancies reduced after the carbon burn off for the chloride precursors. Hence, using a non-chloride precursor coupled with carbon burn off treatments should ideally recover the entire surface on all the carbon supports.

This was found to be true as shown in Figure 2.17 for the carbon supports when comparing the post TPO ratio with the nitrate precursors. Although SEA should ideally filter away the chloride anions, it appears that some residual chloride still remains on the metal and/or carbon, post filtration that is responsible for covering up the surface. Evidences have been seen in the literature [40] that while synthesizing platinum catalysts supported on carbon xerogels using Strong Electrostatic Adsorption (SEA), Cl^- ions issued from the incomplete decomposition/removal of the metal precursor, Chloroplatinic Acid (CPA, H_2PtCl_6) partially block the Pt catalytic sites. Prolonged, high reduction temperatures may remove the chloride from the metal surface, at risk of sintering the particles. The simplest solution, if possible, is to avoid the use of chloride as the balancing ion in precursors, using nitrate or hydroxide salts instead.

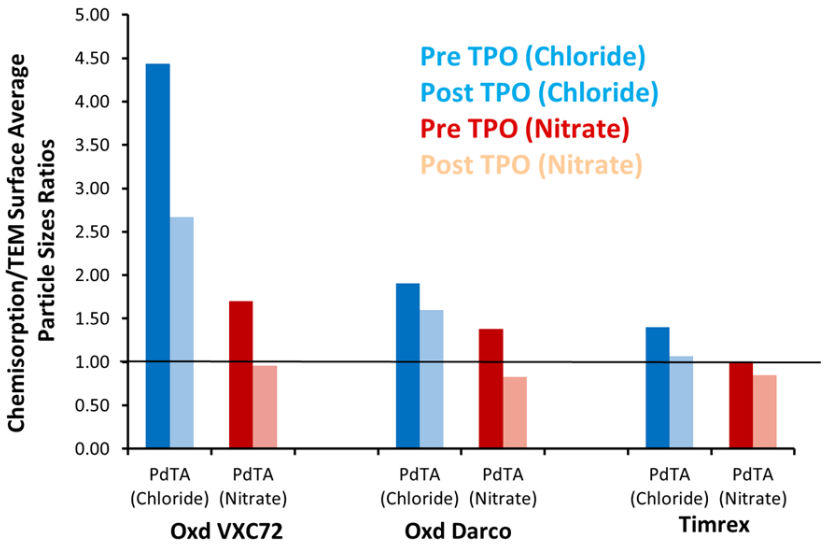

Figure 2.17 Chemisorption particle size comparison using nitrate vs chloride ions for oxidized VXC72, oxidized Darco and Timrex

On the basis of this discussion, Figure 2.18 represents a schematic for the proposed theory that causes the STEM/Chemisorption particle size discrepancy: carbon decoration and/or chloride contamination. The decomposition of the precursor may be initiated during drying and hence, chloride contamination may happen both during drying and reduction. There are mixed opinions in the literature about the stage at which carbon decoration occurs [31, 33]. While Krishnakutty and Vannice claim that the reduction process is responsible for the carbon decoration, Tengco et al have shown that reduction in hydrogen does not cause carbon decoration.

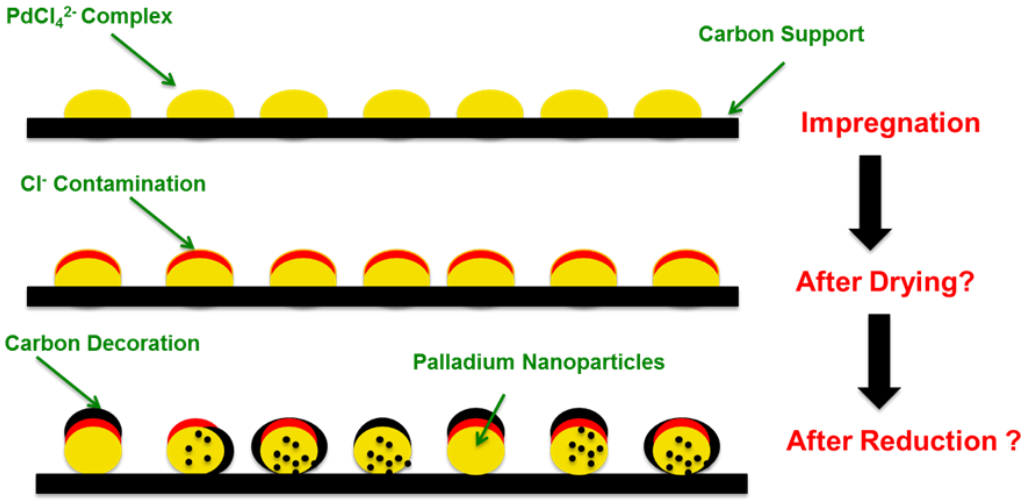

Figure 2.18 Schematic illustration of carbon decoration and chloride poisoning in carbon supported palladium nanoparticles

An additional observation from Figure 2.17 is that the degree of discrepancy is dependent on the type of support, order being: Oxd VXC72> Oxd Darco> Timrex. It is suggested here that the degree of graphitization and the surface oxygen groups may be responsible for this effect. As seen from Figure 2.19a, the degree of graphitization increases

in the order: Oxd VXC72 < Oxd Darco < Timrex whereas Figure 2.19b shows that the trend in surface oxygen groups caries as: Oxd Darco> Oxd VXC72>Timrex. While it has been mentioned before that surface oxygen groups increase the discrepancy by enhancing the Pd-C interaction that causes carbon decoration, graphitization is seen to decrease the discrepancy [Figure 2.19a]. Timrex with the highest degree of graphitization has the least discrepancy. It is suggested here that increase in graphitization causes an enhanced C-C interaction due to the long range ordering of the graphitic basal planes which easily overcomes the Pd-C interactions. The following conclusions can be thus drawn for the three different supports:

(a) **Oxd VXC72:** Carbon black with no graphitization and high number of oxygen groups: strongest Pt-C interaction: **highest degree of carbon decoration**

(b) **Timrex:** Graphitic carbon with very few oxygen groups: C-C interaction much stronger than Pd-C interaction due to long range ordering and absence of oxygen groups: **lowest degree of carbon decoration**

(c) **Oxd Darco**: Activated carbon with partial graphitization and high number of oxygen groups present: **Intermediate degree of carbon decoration**

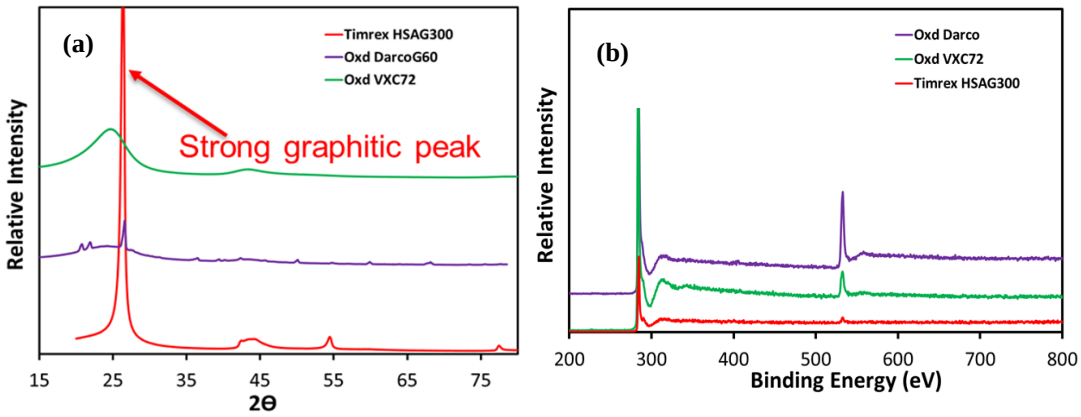

Figure 2.19 (a) XRD of the carbon supports showing degree of graphitization (b) XPS survey scans for the carbon supports showing oxygen content

2.4 Conclusion

A systematic study was performed to understand the effect of carbon supports, surface functional groups, heat treatments and precursors on the STEM/XRD and Chemisorption discrepancies. While the degree of discrepancy decreased with graphitization of the carbon supports due to stronger C-C interaction, increase in oxygen functional groups on the surface increased the discrepancy due to enhance Pd-C interactions. TPO was able to recover only about 50% of the metal surface and the remaining 50% was accounted to be chloride contamination which could be avoided by using nitrate or any other non-chloride precursors. Hence, the steps for reducing the discrepancy involves using non-chloride precursor and introducing a carbon burn off step in oxygen prior to chemisorption.

CHAPTER 3

DETECTION OF AMBIENT OXIDATION OF ULTRA-SMALL SUPPORTED PLATINUM NANOPARTICLES WITH BENCHTOP POWDER X-RAY DIFFRACTION

Abstract:

State of the art X Ray Diffractometers with solid state detectors can detect ultra-small nanoparticles down to 0.5 nm. Ultra-small Pt nanoparticles oxidize spontaneously in ambient atmosphere below 2.5 nm. Below ~1.5 nm, only the oxide phase prevails; in between 1.5-2.5nm, there is a combination of metal and oxide and above 2.5 nm, it is in metallic state.

3.1 Introduction

High metal dispersion, or equivalently, small particle size, is often desired in supported metal catalysts to maximize the number of catalytically active sites per mass of metal. When dealing with ultra-small nanoparticles, however, characterization becomes challenging for particles less than about 2 nm in diameter. Powder x-ray diffraction instruments equipped with conventional scintillation detectors fail to detect particles smaller than about 2.5 nm due to instrumental error and metal peak broadening leading to low signal to noise ratios [41, 37]. These small sizes can be accessed with synchrotron XRD due to the intense beam generated by the synchrotron sources [34, 42-44], however, the cost and limited access to synchrotron sources is frequently prohibitive [45-47].

In recent years semiconductor detectors have become a state of the art option in many benchtop XRD instruments. These are approximately two orders of magnitude more sensitive than traditional scintillation counters; this enhancement is achieved by increasing the active aperture area for detection and increasing the count rate by using a smaller pixel pitch of 0.1 mm [48]. In a previous paper [37], we demonstrated that a benchtop XRD instrument equipped with such a silicon slit detector was able to detect Au nanoparticles as small as 1 nm at low weight loadings, meaning that common powder XRD can now be

significantly extended to the rich regime of particle sizes from 1- 2.5 nm. In the present paper, we demonstrate that this heightened sensitivity enables the same benchtop instrument to detect the spontaneous, ambient oxidation of ultra-small (1-2 nm) Pt nanoparticles, previously observed by XRD only at synchrotron sources.

Supported Pt catalysts find broad applications in industrial processes in exhaust treatment, hydrocarbon hydrogenation, hydrogenolysis and fuel cell applications [49-52]. There are several reports of the spontaneous oxidation of small, initially reduced Pt nanoparticles on various supports (carbon, alumina, silica etc.) upon exposure to ambient air [34, 53-56]. The most definitive of them [34] utilizes synchrotron radiation for characterization by x-ray absorption (EXAFS and XANES) as well as XRD. In the synchrotron XRD patterns, the Pt oxide is evidenced by a low-2θ shoulder on the Pt (111) peak, identified only as "PtO". For both carbon and alumina supported nanoparticles, a combination of metal and oxide phases existed below 2 nm and for the smallest (1.5 nm) particles supported on alumina, the particles were almost completely oxidized. In the other reports [53-56], x-ray diffractometers with scintillation counters were employed and only the metallic fcc Pt phase was identified, while evidence for oxidation was based on XPS. In all papers the relative amount of metallic Pt was found to increase with increasing particle size.

To demonstrate the ability of a benchtop diffractometer with a Si slit detector to clearly identify the oxidation of ultra-small Pt particles, nanoparticles were synthesized over a variety of carbon and silica supports using strong electrostatic adsorption (SEA) which is known to yield small particle sizes with tight size distributions [57, 58]. To

corroborate the XRD results, z-contrast STEM imaging was used for particle sizing in addition to FFT analysis for phase identification.

3.2 Experimental

3.2.1 Carbon and Silica Supports

The variety of carbon blacks, activated and graphitic carbons and carbon xerogels employed with varying surface areas and points of zero charge (PZC) are summarized in Table 3.1. The BET surface areas were determined from nitrogen adsorption-desorption isotherms with a Micromeritics 2020 ASAP instrument. Oxidized VXC72 was prepared by boiling VXC72 obtained from Cabot Corporation in nitric acid (>70%) at 90°C for 3 hours and cooling to room temperature. The mixture was filtered and washed with deionized (DI) water until the pH of the washing solutions reached that of DI water and was dried overnight at room temperature. Timrex HSAG300 and Darco G60 were obtained from Timcal and Cabot Corporation respectively. The carbon xerogels were obtained from the Université de Liège, Belgium. The organic aqueous gels were synthesized by polycondensation of resorcinol and formaldehyde in water using sodium carbonate that was used as basification agent followed by physical activation by carbon dioxide to tailor the carbon particle size and porosity [58].

The silica supports, also listed in Table 1, were Aerosil 300 obtained from Evonik and SBA-15 that were prepared using a modified protocol from Zhao et al [59]. The as-prepared SBA-15 high surface area (761 m^2/g) sample was calcined for 6 hours at 823K and 1173K to generate two lower surface area silica supports (468 m^2/g and 288 m^2/g). The catalysts are denoted by support type (C – carbon, CX – carbon xerogel, and S – silica),

followed by their surface area. For example, C-659 is the 659 m^2/g DarcoG60 carbon support.

Table 3.1 Supports and Precursors

Support Name	Surface Area (m^2/gm)	Abbreviation	PZC	Precursor	Weight Loading (%)
Oxidized VXC72	170	C-170	2.4	$Pt(NH_3)_4^{2+}$ (PTA)	2.7
Timrex	280	C-280	4	$Pt(NH_3)_4^{2+}$ (PTA)	2.4
DarcoG60	659	C-659	8.5	$Pt(Cl_6)^{2-}$(PHC)	10
Carbon Xerogels	679	CX-679	10	$Pt(Cl_6)^{2-}$(PHC)	6.9
Carbon Xerogels	1723	CX-1723	9.5	$Pt(Cl_6)^{2-}$(PHC)	17.3
SBA-15	288	S-288	4.4	$Pt(NH_3)_4^{2+}$ (PTA)	5.4
SBA-15	761	S-761	3.9	$Pt(NH_3)_4^{2+}$ (PTA)	10
SBA-15	468	S-468	3.9	$Pt(NH_3)_4^{2+}$ (PTA)	5.5
Aerosil	330	S-330	3.9	$Pt(NH_3)_4^{2+}$ (PTA)	5

3.2.2 Preparation of supported platinum nanoparticles

Strong electrostatic adsorption [57, 25, 60] was used to adsorb Pt complexes onto the supports. For the low and mid PZC oxidized VXC72, Timrex, SBA-15 and Aerosil supports, the cationic precursor, tetraammineplatinum(II) chloride ([PTA, $Pt(NH_3)_4]OH_2$, 99.999%) was used and for the high PZC carbon xerogels and DarcoG60, chloroplatinic acid (or platinum hexachloride, PHC, $H_2[PtCl_6]$, 99.9%) was used as the anionic precursor. The precursors used for the supports and the metal weight loadings are summarized in Table 1. The high PZC supports were weighed out to obtain the desired 500 m^2/L surface loading and the low and mid PZC supports weighed out for 1000 m^2/L. PTA and PHC solutions at the required concentration were then contacted with the respective carbon supports for an hour at the optimal pH of 12 for PTA and 2.8 for PHC, after which the

catalyst slurry which was filtered, dried in ambient air overnight, and then oven dried in static air at 120°C for 16 hrs. The dried supports were reduced in a flowing 10% H_2 balance He for 1 hr at temperatures determined from temperature programmed reduction (listed in Table 3.2), with a ramp rate of 2.5°C/min. The weight loadings as determined by an ICP-OES and are listed in Table 3.1. A 20% Pt/C commercial carbon from Premtek prepared by dry impregnation was also employed in the study. Most samples were air exposed for 2-4 weeks.

3.2.3 Characterization

A Rigaku Miniflex-II equipped with a D/teX Ultra silicon strip detector was used to perform powder XRD on the supported Pt particles. Diffraction patterns were recorded over a range of 10°–80° 2θ using Cu-Kα radiation (k = 1.5406 Å) that was operated at 30 mA and 15 kV using Bragg–Brentano geometry. A slit width of 0.2 and scan rate of 0.5°/min was used for all scans for both detectors. XRD patterns were obtained for all metal free supports in addition to the supported metals. Fityk 0.9.8 version software [24] was employed for background subtraction and deconvolutions using psuedo-Voigt shapes to take the peak asymmetry into account. The full width at half maximum (FWHM) values were input together with a shape factor of 0.94 in the Scherrer equation to estimate particle size [37].

High and low magnification images of the catalysts was obtained with an aberration-corrected JEOL 2100F scanning transmission electron microscopy (STEM) using Z-contrast imaging. Fast Fourier Transform (FFT) analysis of the high resolution STEM images was done using ImageJ software while particle size analysis was performed

using Particule2 software. Sample preparation involved ultrasonicating the sample in ethanol and adding a drop to a copper TEM grid with a thin holey carbon coating.

3.3 Results and Discussion

3.3.1 XRD analysis

The powder XRD patterns obtained for the air exposed catalysts are shown in Figure 3.1 (a through j) for the carbon supports C-170, C-659, C-280, CX-679, CX-1723, a commercial 20% Pt on VXC72 and the silica supported S-288, S-330, S-488, S-761 catalysts respectively. The full patterns from the support and catalyst are shown along with the background subtractions and deconvoluted patterns in the insets. The background subtractions were not perfect for reasons also cited in [34]; attenuated sampling depth due to the presence of the heavy Pt phase, and changes to the support during reduction. The first effect is seen for the carbon xerogel and Vulcan XC72 (carbon black) samples in Figures 3.1d, e and f, where the intensity of the carbon background from 20-30º 2θ is greatly diminished for the metal loaded sample (the same volume of material was used for every comparison); this appears as a shoulder at 27º 2θ. The second effect is seen in the samples with graphitic peaks, especially the high surface area graphite Timrex sample of Figure 3.1b and to a lesser extent in the DarcoG60 sample of Figure 3.1c, where it appears the reduction has further graphitized the carbon. Even with these "glitches" [34], the signal/noise ratio of the background subtracted patterns in Figure 3.1 compare very favorably to those obtained from the synchrotron diffractometer (see Figure 6 of [34]).

In the deconvolutions, metallic fcc Pt peaks are seen most clearly in the three samples with largest metal Pt particle size, the 10Pt/C-659 (Fig. 3.1c), 17.3Pt/CX-1723 (Fig. 3.1e), and 20Pt/VXC72 (Fig. 3.1f). Clear peaks are seen for the (111), (200) and

(220) reflections at 39.7, 46.2, and 67.5º 2θ, respectively. Additionally, the 17.3Pt/CX-1723 pattern is fit by assuming a bimodal distribution of Pt particles size, which is confirmed by its STEM particle size distribution (discussed in the next section). In the remaining samples, which are comprised of the smallest Pt particles, the Pt (220) peak is significantly diminished or in many cases even absent; this is not unexpected for the ultra-small sizes being analyzed here, as higher order reflections require many unit cell volumes of sample. Size estimates of the metallic Pt phase were estimated from the Scherrer equation and are summarized in Table 3.2. These range from 3.6 nm for the largest particles (17.3Pt/CX-1723 in Fig. 3.1e) to 0.5 nm for the smallest (5.5Pt/S-468 in Fig. 3.1i). It is noted that the latter size estimate is much lower than the typical size limit of about 2 nm discernable with diffractometers fitted with scintillation counters. In a previous work 1.3 nm particles were clearly observed with a solid state detector for a 1 wt% Au/carbon sample [37]. Here, the metal weight loading is 5 times higher, and the very broad peaks fitted to the Pt (111) and Pt (200) reflections are clear, assuming that the Pt oxide phase has been fit well. That is now discussed.

In all the deconvolutions, a large peak to the left of the Pt (111) peak appears in all patterns. For the samples with the two largest particle sizes, the 17.3Pt/CX-1723 sample (Fig. 3.1e) and the 20Pt/VXC72 sample (Fig. 3.1f), this peak appears as a left hand shoulder on the Pt (111) peak. In many of the other samples, the area of this peak approaches in size or even swamps the metal peaks and is consistent with oxidation occurring to a greater extent over smaller particles. It is interesting to note that upon close inspection of the scintillation XRD data of references [53] and [54], a left hand shoulder on the Pt(111) peak appears for the smallest particles analyzed, specifically, in the Pt/CNT sample in Figure 2

of [53] and the two lower patterns in Figure 2 of [54]. The presence of Pt oxide was demonstrated in both of these works by XPS, but the relatively poor signal/noise from the scintillation counter, however, appears to have prevented the conclusive identification of this phase by XRD.

The oxide phase in the synchrotron XRD work, identified only as "PtO," was not associated with a particular oxide phase given the high degree of disorder [41]. The relatively good signal/noise in the deconvolutions presented here in fact allows a suggested assignment. The position of the main non-fcc Pt peak that occurs at 35.9° 2θ, per the JCPDS database, corresponds to the highest intensity reflection of Pt_3O_4, the (210). The absence of the second most intense Pt_3O_4 peak, the (110) at 22.5° 2θ, (48% of (210) for a random, large sample) might be explained by the sampling depth problem mentioned earlier; in Figure 3.1, all the carbons and silicas have a support feature in the 20-30° 2θ range which changes significantly with addition of Pt, and this would prevent the broad, low intensity (110) peak from being isolated in the subtracted patterns. Perhaps the strongest feature in support of a Pt_3O_4 assignment are the deconvolutions which feature a broad hump in the 50-70° 2θ range, particularly in Figs. 3.1i and j, and to a lesser extent in Figs. 3.1a, b, and c. In these five cases the data can only be fit with the inclusion of the Pt_3O_4 bcc (211), (222) and (320) reflections at 39.49, 57.08 and 59.64° respectively, with relative intensities about two thirds to one-half of those given in the JCPDS file for a large random sample. The rest of the samples do not exhibit these higher order peaks. This might be explained by preferred orientation of the Pt oxide phase skin residing on a metal core. For the 6.9Pt/CX-679 carbon sample (Fig. 3.1d) and the 5Pt/S-330 silica sample (Fig.

3.1h), virtually all of the intensity can be attributed to the Pt_3O_4 (210) peak. The thickness of the Pt_3O_4 phase ranged between 0.6 and 1.1 nm, and is listed in Table 3.2.

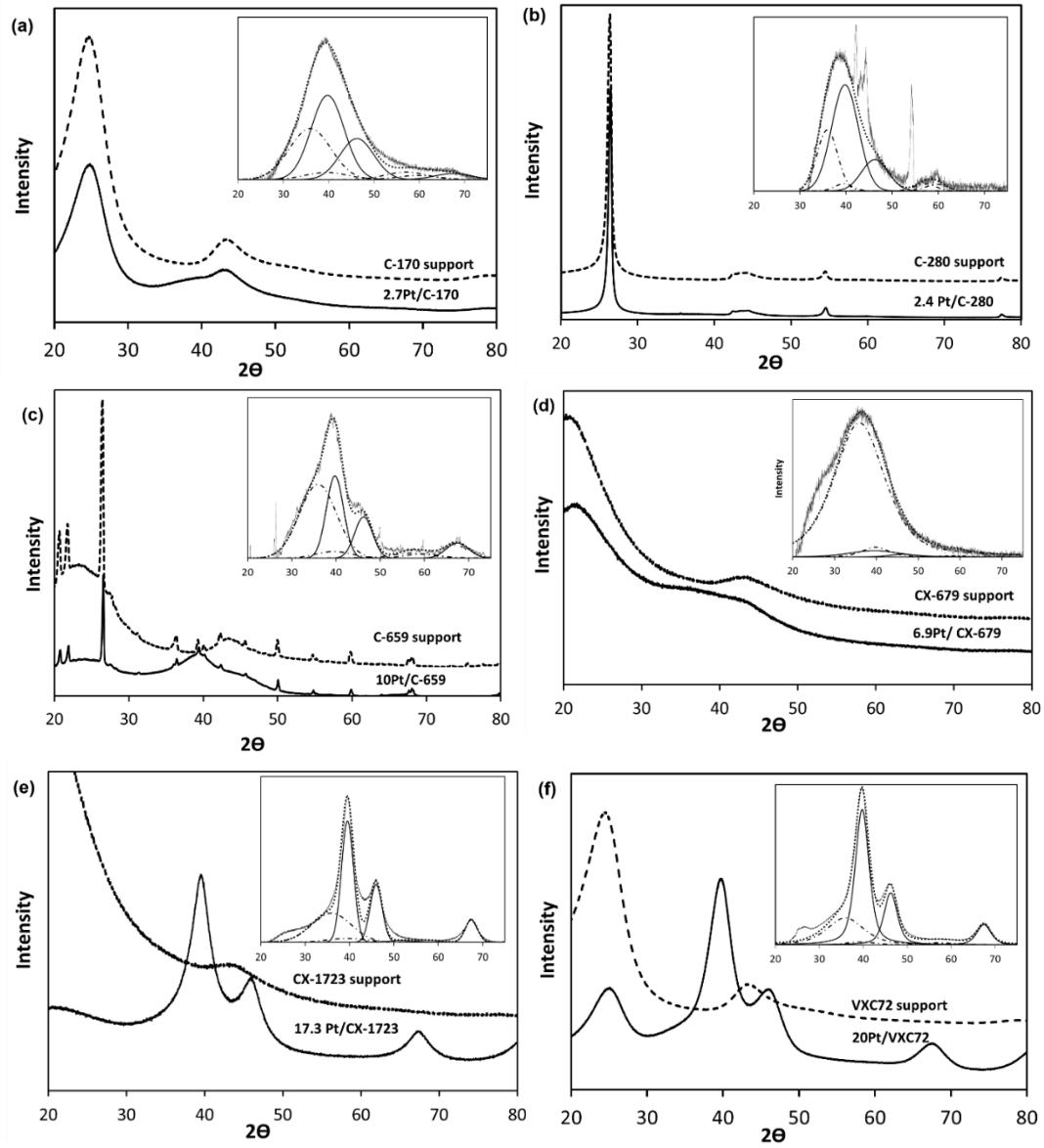

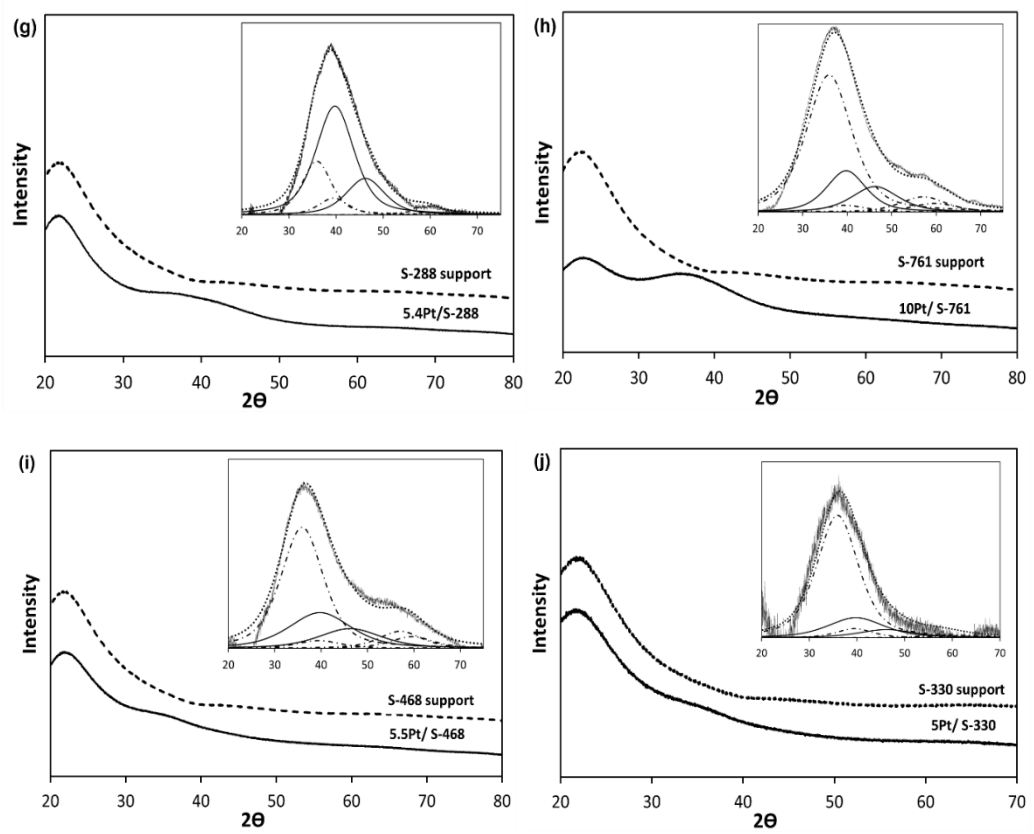

Figure 3.1 XRD Profiles with deconvoluted patterns in the inset for (a) 2.7Pt/C-170 (b) 2.4Pt/C-280 (c)10Pt/C-659 (d) 6.9Pt/CX-679 (e) 17.3Pt/CX-1723 (f) 20Pt/VXC72 (g) 5.5Pt S-288 (h) 10Pt S-761 (i) 5.4Pt S-468 (j) 5Pt S-330

Table 3.2 XRD and STEM particle sizes

Catalyst	Reduction Temperatures (℃)	XRD Sizes (nm)			STEM Volume Average Sizes (nm)
		Pt	Pt_3O_4	$Pt+Pt_3O_4$	
2.7Pt/C-170	200	1.0	0.8	1.8	1.5±0.3
2.4Pt/C-280	200	1.0	0.9	1.9	1.6±0.2
10Pt/C-659	200	1.8	0.9	2.7	2.2±0.4
6.9Pt/CX-679	250	1.1	0.6	1.7	1.5±0.4
17.3Pt/CX-1723	250	3.4	1.1	4.5	3.9±1.5
20Pt/VXC72 (Commercial)		2.4	0.9	3.3	4.3±1.6
5.4Pt/S-288	700	0.9	0.6	1.5	1.2±0.2
5Pt/S-330	250	1.1	0.7	1.8	1.6±0.5
5.5Pt/S-468	350	0.5	0.8	1.3	1.1±0.2
10Pt/S-761	350	0.8	0.7	1.5	1.5±0.2

3.3.2 STEM imaging and FFT analysis

To corroborate the XRD data, aberration-corrected z-contrast STEM analysis was performed on all the samples. These are shown in Figure 3.2, in the same order as Figure 3.1. Particle size distributions were obtained by counting from 800-1000 particles on each sample. The STEM volume-averaged sizes (for most appropriate comparison with XRD values) are given in Table 3.2. The SEA method yielded small sizes ($\leq$ 2.2nm) for all supports except the high surface area CX-1723, with sizes for the silica samples (Figures 3.2g-j) being a bit smaller than for the carbon supports.

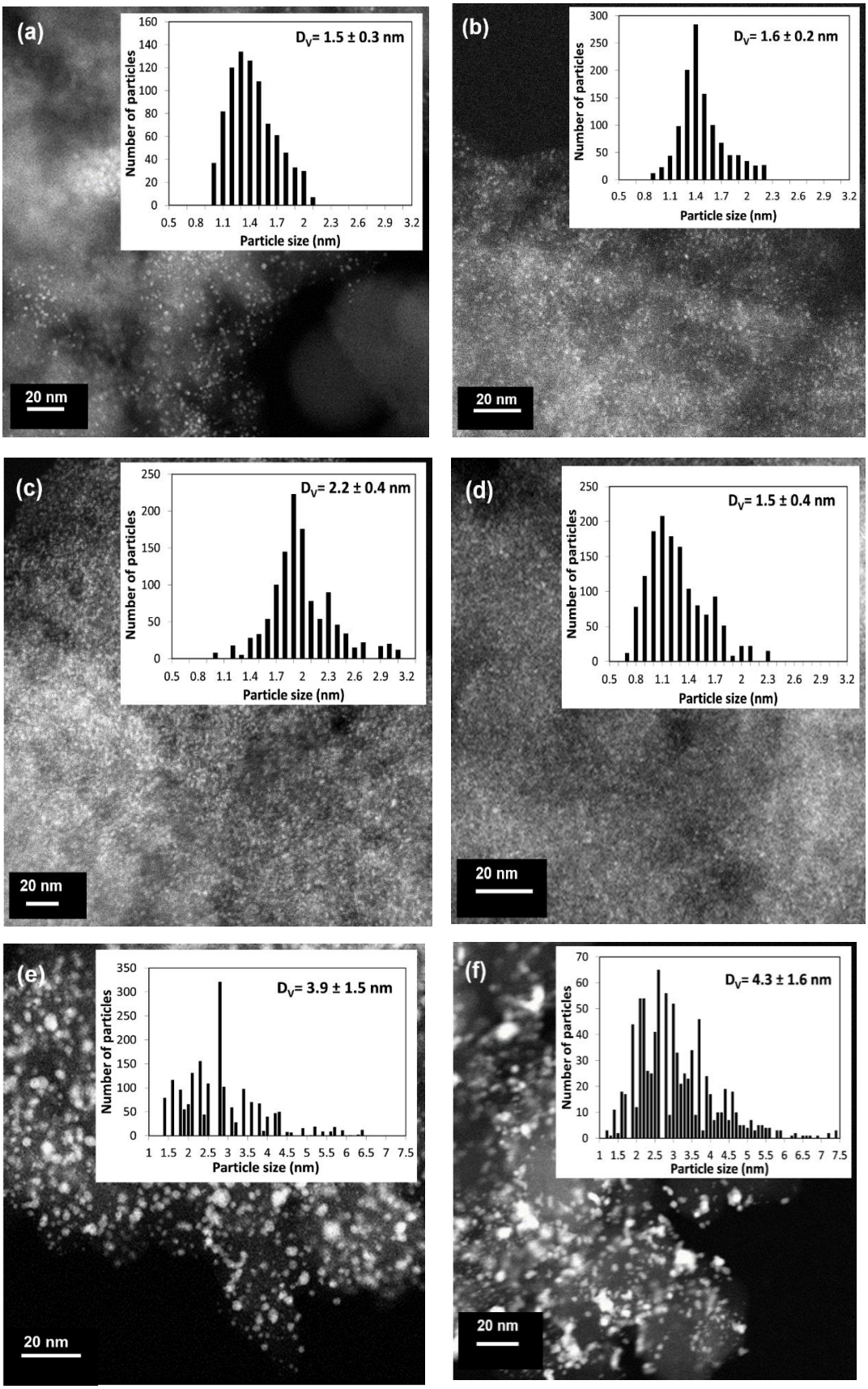
(a)
D_V= 1.5 ± 0.3 nm
Number of particles
Particle size (nm)
20 nm
(b)
D_V= 1.6 ± 0.2 nm
Number of particles
Particle size (nm)
20 nm
(c)
D_V= 2.2 ± 0.4 nm
Number of particles
Particle size (nm)
20 nm
(d)
D_V= 1.5 ± 0.4 nm
Number of particles
Particle size (nm)
20 nm
(e)
D_V= 3.9 ± 1.5 nm
Number of particles
Particle size (nm)
20 nm
(f)
D_V= 4.3 ± 1.6 nm
Number of particles
Particle size (nm)
20 nm

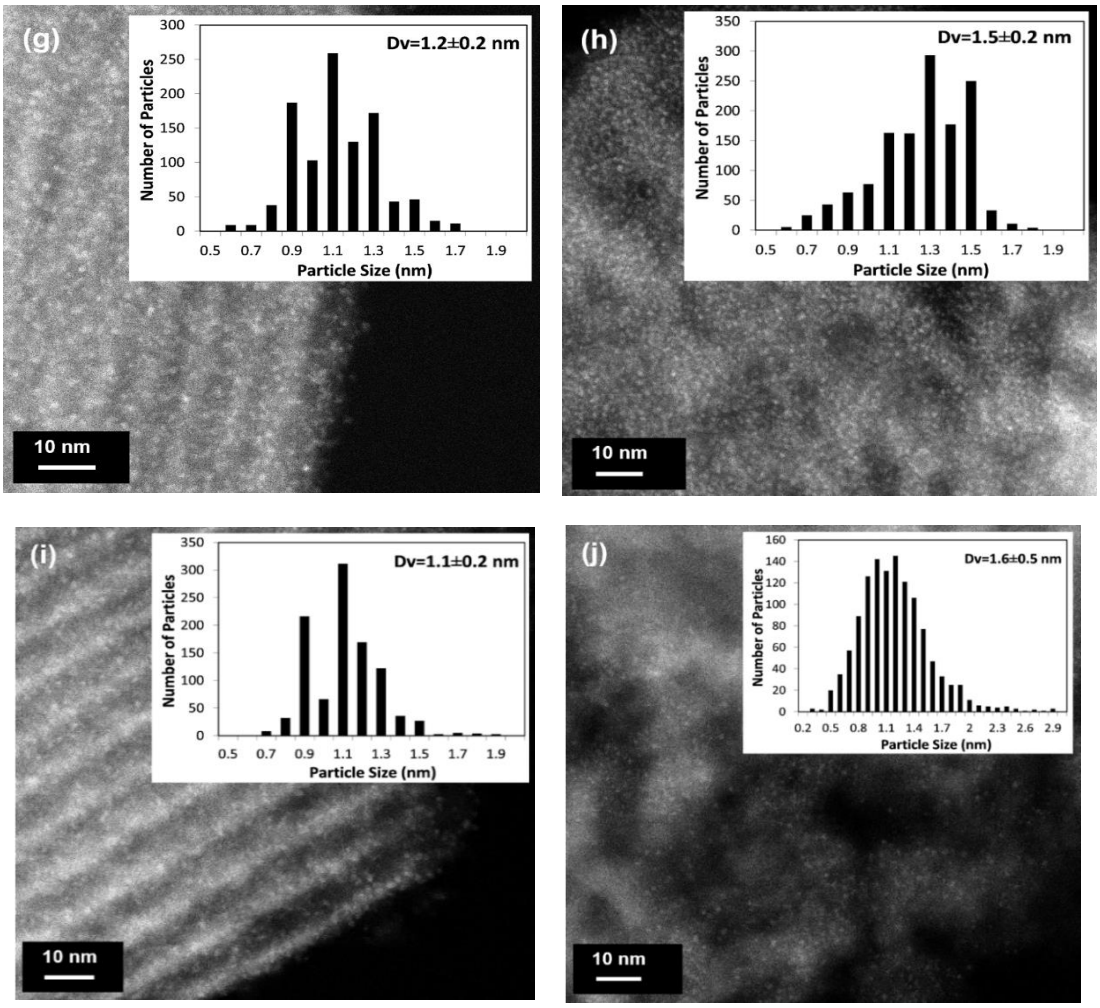

Figure 3.2 STEM images with particle size distributions for (a) 2.7Pt/C-170 (b) 2.4Pt/C-280 (c) 10Pt/C-659 (d) 6.9Pt/CX-679 (e) 17.3Pt/CX-1723 (f) 20Pt/VXC72 (g) 5.5Pt S-288 (h) 10Pt S-761 (i) 5.4Pt S-468 (j) 5Pt S-330

A simplistic notion of nanoparticle oxidation is that each nanoparticle is comprised of a metal core and oxide shell. The overall average size of Pt nanoparticles would then be the sum of the Pt metal and oxide shell thicknesses. A comparison of this sum to the STEM-estimated sizes, seen in Table 3.2, is not in unreasonable agreement. However, a more refined analysis of the extent of oxidation versus particle size was performed with FFT analysis of individual, atomically resolved particles. Measuring the reciprocal lattice vectors using their FFT is a common method for determining precise atomic spacings [62].

High resolution HAADF STEM imaging was possible with the three different sets of carbon supported catalysts: 2.7 Pt/C-170, 10% Pt/C-659 and 20%Pt/VXC72. Figure 3.3 shows representative images of 10% Pt/C-659 where the atomic resolution can be clearly seen along with the corresponding FFT patterns of three labelled particles to the right. The FFT pattern reveals 0.23 nm and 0.25 nm d-spacings corresponding to the most intense reflections from the crystalline planes (111) of Pt with an fcc cubic structure (JCPDS Card no: 00-004-0802) and (210) planes of Pt_3O_4 (JCPDS Card no: 01-089-2356) with a bcc cubic structure [63] respectively. Representative particle 1 (size~1.5 nm) showed only the Pt_3O_4 phase, particle 2 (size~ 2.2 nm) was found to have a combination of Pt and Pt_3O_4 phases and particle 3 (~2.6 nm) showed only metallic platinum. Since FFT analysis is done only on the top slice of the HRTEM images and due to the extremely small sizes of these ultra-small nanoparticles, only the strongest reflections from each phase could be analyzed successfully.

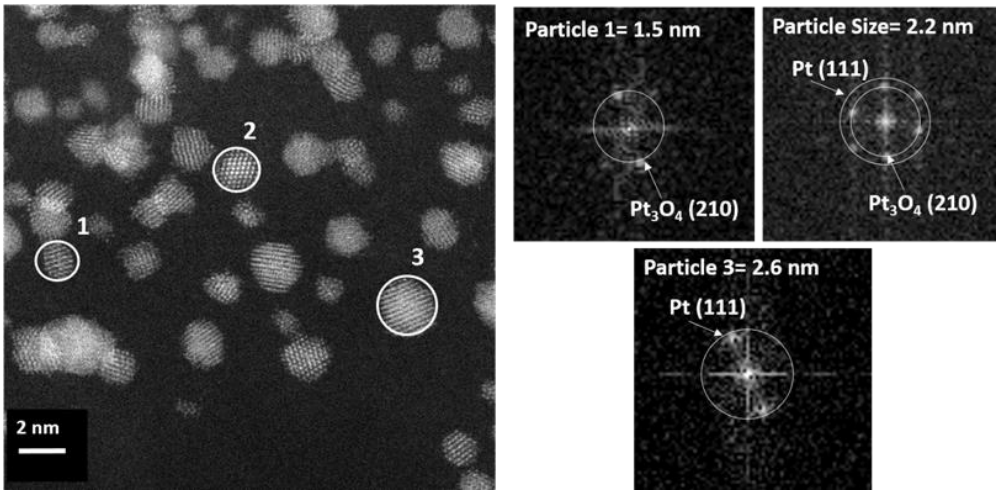

Figure 3.3 HRTEM images with inset FFT patterns for particle size distributions for 10Pt/C-659 after air exposure

Analyzing a total of 70 particles for the three different catalysts showed a clear trend in oxidation with particle size. Figure 3.4 gives a histogram of the sizes along with their corresponding composition. The oxide phase was observed exclusively up to 1.5 nm, and as high as 1.8 nm, while from 1.6 to 1.7 nm both pure oxide and metal core/oxide shell particles were observed. From 1.8 to 2.4 nm, only metal/oxide particles were detected. From 2.5 to 2.7 nm, metal/oxide and metal particles were detected, while above 2.7 nm, only the metallic phase was observed. Based on the statistics from Figure 3.4, it was concluded that particles from 1.6 to 2.7 nm are normally core metal/shell oxide; below 1.6 nm they exist at pure oxides, and above 2.7 nm, as metal.

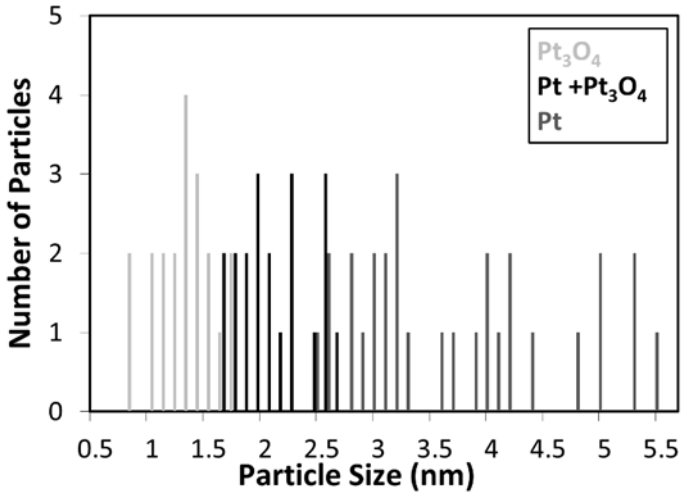

Figure 3.4 Particle Size distributions for the Pt- metal and oxide phases

The oxidation dependence on size is illustrated in Figure 3.5 and calls for a different interpretation of the deconvoluted XRD data. For samples with the smallest average nanoparticle sizes, the majority of the particles exist as oxide only, while only the largest particles in the distribution contain a small core of metal. For catalysts with the largest average particle size, the majority of particles are metallic, and while the smallest particles in the distribution exist as metal cores/oxide shells.

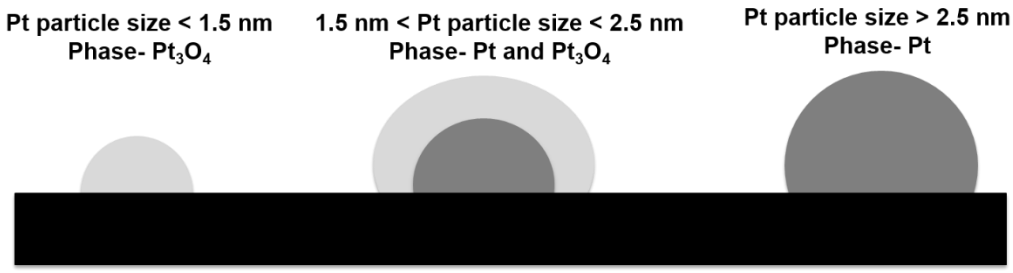

Figure 3.5 Illustration of phases in carbon supported platinum with changing particle sizes

3.4 Conclusion

This paper demonstrated the capability of a solid state Si-strip detector in detecting the spontaneous oxidation phenomenon in ultra-small platinum nanoparticles. The dramatic effect of platinum nanoparticle size on their oxidation under ambient atmospheric conditions was established. Platinum nanoparticles smaller than 2.5 nm have an inherent susceptibility to oxidation : below 1.5 nm, they exist only in the oxide phase; in the range of 1.5 to 2.5 nm, they exist in a combination of both metallic and oxide phases while above 2.5 nm, it is all metallic. The oxide phase was determined to be Pt_3O_4. With this work, the authors establish that solid state detectors make powder XRD a much more cheaper and time efficient alternative to the expensive and time consuming synchrotron techniques and low resolution conventional scintillation detector based XRD techniques.

CHAPTER 4

THE ROLE OF CARBON SUPPORTS IN THE AMBIENT OXIDATION OF ULTRASMALL PLATINUM NANOPARTICLES

Abstract:

Ultrasmall carbon supported platinum nanoparticles have often been shown to undergo partial oxidation on exposure to ambient air. In this work, it is hypothesized that the micropores in carbon play an important role in affecting the degree of oxidation. It was found that carbon supports with higher microporosity gave larger metal particles at high metal weight loadings whereas the particle sizes remained independent of microporosity at low weight loadings. Lower oxide contents were found for larger metal particles leading to the conclusion that micropores controlled the oxide content indirectly by controlling the particle sizes at high weight loadings.

4.1 Introduction

Porous carbon materials have long been used as supports in heterogeneous catalysis due to their highly developed internal surface area and pore structure that makes them act as excellent adsorbents in solvent media during the catalyst synthesis process [64-67]. However, there has been some debate about the advantages and disadvantages of support structure and porosity in catalytic reactions [68-70]. While the effective distribution of expensive catalytic metals in the pore structure enables maximizing the surface to volume reaction during chemical reactions [71], support porosity can also pose serious mass transfer limitations during the transport of reactants to reach the active metal sites [68].

During the synthesis of carbon supported platinum nanoparticles, it has been reported in the literature that ultra-small supported nanoparticles of Pt tend to be oxidized either completely or partially when exposed to air at room temperature following the reduction [34, 54, 55]. Due to the equally broad usage of platinum oxides compared to their metal counterpart, in industrial catalytic processes like carbon monoxide oxidation, nitric

oxide reduction, hydrocarbon hydrogenation and methanol oxidation [72-76], it is crucial to understand surface composition of platinum and the chemical and structural nature of the oxide phases formed on Pt surfaces. It has been found that while the Pt_3O_4 phase of platinum is the active phase during carbon monoxide oxidation and nitric oxide reduction reactions, the PtO_2 phase is inactive [77]. The oxidation phenomenon is found to be extremely sensitive to the size of the nanoparticles and was more common for smaller nanoparticles (< 1.5 nm) but less prevalent for larger nanoparticles (> 3nm) which behaves mostly like bulk platinum that is extremely difficult to oxidize even at elevated temperatures [55, 77]. In-situ synchrotron studies by Miller et al [34] have shown that the extent of platinum oxidation was both size and support dependent. While 97% PtO was prevalent on the Pt/ Al_2O_3 catalyst with particle sizes of 2.1 nm, only 79% PtO was found on the Pt/CNT catalysts with 1.6 nm particle sizes, 67% on the Pt/ Al_2O_3 with particle sizes of 2.1 nm and 33% on the Pt/ Al_2O_3 with particle sizes of 3.3 nm. In other words, the PtO fraction decreased with increasing particle size. Additionally, the platinum nanoparticles completely oxidized on the oxide support whereas the carbon nanotubes had a combination of both the metal and oxide phases.

In a recent work by the authors [78], state of the art X Ray Diffractometers with solid state detectors was used to detect the ambient oxidation of ultra-small Pt nanoparticles supported on carbon and silica. Below ~1.5 nm, only the oxide phase prevails; in between 1.5-2.5 nm, there is a combination of metal and oxide and above 2.5 nm, it is in metallic state.

In this paper, it is hypothesized that the microporosity of carbon supports play an important role in affecting the degree of oxidation of ultra-small platinum nanoparticles.

However, obtaining phase and structural information at such small length scales (< 1.5 nm) can be a challenging task. In order to prove this hypothesis, three different characterization tools are employed: State –of-the-art benchtop X-Ray diffractometers equipped with Si-strip detectors (XRD), Scanning Transmission Electron Microscopy (STEM) and X-Ray Photoelectron Spectroscopy (XPS).

4.2 Experimental

4.2.1 Materials

The supports and precursors used and the catalysts prepared along with their as-determined BET surface areas and PZCs are summarized in Figure 1. Different types of high purity carbons were obtained: carbon black (VXC7), activated carbons (DaroG60), graphitic carbon (Timrex HSAG300) and carbon xerogels. Oxidized VXC72 (PZC 2, BET area: 170 m^2/g) was prepared by boiling VXC72 obtained from Cabot Corporation in nitric acid (>70%) at 90°C for 3 hours and then, cooling it down to room temperature. The mixture was filtered and washed with deionized water until the pH of the washing solution reached 5 and was dried overnight at room temperature. Timrex HSAG300 (BET area: 236 m^2/g) and Darco G60 (BET area: 659 m^2/g) were obtained from Timcal and Cabot Corporation respectively. The carbon xerogels were obtained from the Université de Liège, Belgium. The organic aqueous gels were synthesized by polycondensation of resorcinol and formaldehyde in water using sodium carbonate that was used as basification agent followed by physical activation by carbon dioxide to tailor the carbon particle size and porosity [58].

The BET surface areas and pore size distributions were obtained using nitrogen adsorption-desorption isotherms at 77.5K with a Micromeritics 2020 ASAP instrument. It has been mentioned in the literature that measurements of micropore volume by nitrogen adsorption may give erroneous isotherms due to the low temperature and pressures at which the adsorption takes place and the quadrupole moment of the diatomic nitrogen molecule that produces specific interactions at the gas-solid interface [79, 80]. For the carbons C-170, C-280, C-659 argon adsorption-desorption isotherms at 77.5K was conducted. For the carbon xerogels, the micropore and macro-meso pore distributions and corresponding pore volumes for the xerogels were obtained from nitrogen desorption [58] and mercury porosimetry techniques respectively [81]. The micropore volumes for the xerogels were calculated from t-plots using the Dubinin–Radushkevich equation whereas for all the other supports, the Harkin's Jura thickness equation was used [82].

Two other high surface area carbons KJ600 and BP2000 were used for the study. The micropore volumes were obtained from the literature (listed in the discussions section).

4.2.2 Preparation of carbon supported platinum nanoparticles

Table 4.1 shows a summary of the carbon supported catalysts prepared by Strong Electrostatic Adsorption (SEA) [25, 57, 83]. Based on the SEA protocol, a cationic precursor, Tetraammineplatinum(II) chloride ([PTA, $Pt(NH_3)_4]OH_2$, 99.999%) was chosen for the low PZC supports while an anionic precursor, Chloroplatinic acid (or platinum hexachloride, PHC, $H_2[PtCl_6]$, 99.9%) was used for the high PZC supports. The required concentrations of the precursor solutions were then, contacted with the supports for an hour followed by filtration and subsequent drying in ambient air overnight and

drying in an oven at 120°C for 16 hrs. The resultant weight loadings were determined from the uptake of platinum ions in an ICP-OES and are tabulated in Table 4.1. The catalysts are denoted by their platinum weight loadings followed by support type (C – carbon and CX – carbon xerogel), followed by their surface area. For example, 2.7Pt/C-170 denotes 2.7 wt% Pt on 170 m^2/gm oxidized VXC72 carbon support. The dry impregnated samples were then reduced in a flowing 5 % H_2 balance He for 1 hr with a ramp rate of 2.5°C/min at different reduction temperatures based on Temperature Programmed Reduction (TPR). The reduction temperatures are listed in Figure 2. Another set of 6% metal loading catalysts were prepared for all the xerogels and a 10% metal loading for the xerogels, CX-1162 and CX-2234.

The catalysts supported on the high surface area KJ600 and BP2000 carbons have been prepared by SEA earlier and have been added to the Table 4.1 [57].

Table 4.1 Summary of supports, precursors and catalysts

Support Name	**Surface Area (m^2/gm)**	**Abbreviation**	**PZC**	**Precursor**	**Catalyst**
Oxidized VXC72	170	C-170	2.4	$Pt(NH_3)_4^{2+}$ (PTA)	2.7Pt/C-170
Timrex	280	C-280	4	$Pt(NH_3)_4^{2+}$ (PTA)	2.5Pt/C-280
DarcoG60	659	C-659	8	$Pt(Cl_6)^{2-}$(PHC)	10Pt/C-659
Carbon Xerogels	679	CX-679	10	$Pt(Cl_6)^{2-}$(PHC)	6Pt/CX-679
Carbon Xerogels	1162	CX-1162	10.1	$Pt(Cl_6)^{2-}$(PHC)	6.4Pt/CX-1162
					10Pt/CX-1162
					12.8Pt/CX-1162
Carbon Xerogels	1723	CX-1723	9.5	$Pt(Cl_6)^{2-}$(PHC)	17.3Pt/CX-1723
					6.5Pt/CX-1723
Carbon Xerogels	2234	CX-2234	10	$Pt(Cl_6)^{2-}$(PHC)	6.5Pt CX-2234
					10.3Pt CX-2234
					16.4Pt/CX-2234
KJ600	1189	C-1189	9.4	$Pt(Cl_6)^{2-}$(PHC)	27Pt/C-1189
BP2000	1474	C-1474	9.5	$Pt(Cl_6)^{2-}$(PHC)	28Pt/C-1474

4.2.3 Catalyst Characterization

Powder X-Ray Diffraction (XRD) and Scanning Transmission Electron Microscopy (STEM) measurements were used to characterize the set of samples. XRD measurements were made using a Rigaku Miniflex-II equipped with D/teX Ultra silicon strip detector that can detect nanoparticles down to 0.8 nm [78, 37]. Diffraction patterns were recorded over a range of 20°–80° 2θ using Cu-Kα radiation (k = 1.5406 Å). XRD patterns were captured for all the carbon supported catalysts and compared to reference spectra using PDXL 2.0 (Rigaku Corporation) software and background subtractions and deconvolutions were done using Fityk 0.9.8 version Software [61].

Z contrast images were obtained using an aberration-corrected JEOL 2100F scanning transmission electron microscope (STEM) equipped with a 200Kv field emission gun and a double tilt holder for tilting the sample across a range of angles (±20°). High angle annular dark-field (HAADF) STEM images were acquired on a Fischione Model 3000 HAADF detector with a camera length such that the inner cut-off angle of the detector was 50 mrad [84].

4.2.4 X-Ray Photoelectron Spectroscopy (XPS)

X-Ray photoelectron spectroscopy (XPS) was used to probe the elemental composition and the chemical state of the air exposed platinum nanoparticles. XPS measurements were conducted using a Kratos AXIS Ultra DLD XPS system equipped with a monochromatic Al K source. The monochromatic Al K source was operated at 15 keV and 120 W [30]. The peak position and peak area obtained from XPS are used to evaluate

the composition, while the peak shape provides the information about chemical shifts or chemical bonds of the elements.

In order to evaluate the effect of increasing air exposure on the platinum nanoparticles, the xerogel supported catalysts were probed in ultra-vacuum in the XPS chamber under the following conditions: (a) after in-situ reduction in hydrogen for 1 hr at 200℃ (b) after short time air exposure (c) after long time air exposure. In addition, the 6.9Pt/CX-679 catalyst was probed in EHV chamber in the XPS (a) after in-situ reduction in hydrogen for 1 hr at 200℃ (b) after short time air exposure (c) after long time air exposure (d) after oxidation in oxygen for 1 hr at 350℃.

4.3 Results and Discussion

4.3.1 Microporosity of supports

The pore size distributions and micropore volumes of the carbon supports are shown in Figure 4.1. Figure 4.1a shows that C-170, C-280, C-659 are predominantly microporous with a very small amount of mesopores whereas Fig 4.1b and c shows that the xerogels are comprosed of micro, meso and macro pores. The micropore volumes of the carbons are plotted in increasing order in Fig 4.1d with C-280 having the lowest and CX-2234 having the highest micropore volumes. Two additional high surface area carbons, C-1189 (KJ600) and C-1474(BP2000) known to be microporous from the literature have also been to this figure for a more detailed study [85, 86, 91].

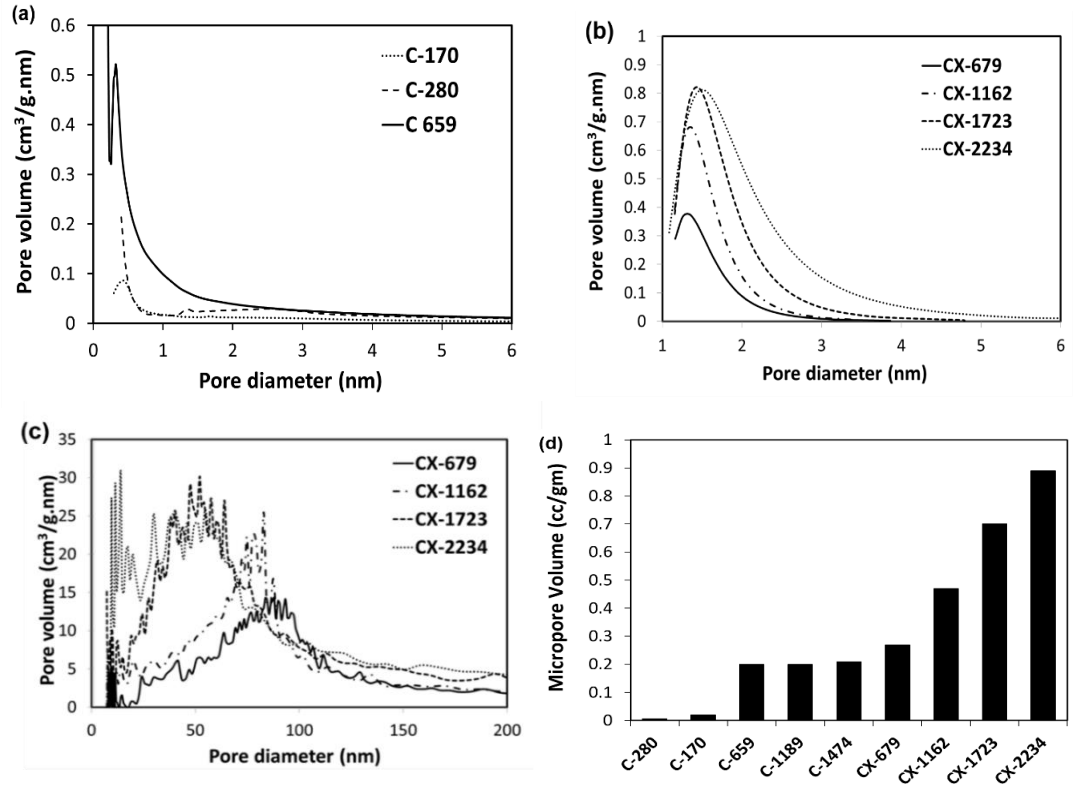

Figure 4.1 (a) Pore size distributions of C-170, C-659 and C-236 with argon desorption (b) Micropore size distributions of Carbon xerogels with nitrogen desorption (c) Meso and Macropore Size distributions of xerogels using mercury porosimetry (d) Micropore volumes for carbons

As mentioned earlier, the xerogels were synthesized by polycondensation of resorcinol and formaldehyde in water using sodium carbonate that was used as basification agent followed by physical activation by carbon dioxide to tailor the carbon particle size and porosity [58]. In order to obtain an idea about the surface distribution between micropores inside the nodules and the surface outside the nodules for the carbon xerogels, the bulk density was calculated from Hg porosimetry and N_2 adsorption, which helps to calculate the external surface per volume of sample. The purpose is to check if the surface of the nodules change by erosion during the activation process. The surface per volume

must be used in this case and not the surface by mass since the mass of the nodules changes upon activation. Table 4.2 shows that the activation process leads to an increase of the total surface due to the formation of micropores inside the nodules only. The external surface per volume of sample remains constant. For the CX-2234 support, it was not possible possible to discriminate mercury that enters the pores from mercury that goes between the powder particles.

Table 4.2 Change in external surface per volume of the sample due to activation in carbon xerogels

Support	S_{ext} (m^2/gm)	Bulk Density (gm/cm^3)	S_{ext} (m^2/cm^3)
CX-679	155	0.58	90
CX-1162	196	0.49	96
CX-1723	258	0.36	93
CX-2234	483	NA	NA

4.3.4 Strong Electrostatic Adsorption on Carbon Supports

In earlier work done in the Regalbuto group [57], it has been shown that the Pt concentration of 180 ppm corresponds to about a 10% excess of one monolayer of Pt (1.6 µmol/m^2) for the employed surface loading of 500 m^2/L. A PTA concentration of 312 ppm corresponds to about a 10% excess of one monolayer of Pt (0.84 µmol/m^2) for a surface loading of 2000 m^2/L. From Figure 4.2, C-659 (PZC 8) had the standard uptake of 1.6 µmol/m^2 however, the carbon xerogels (PZC ~10) , CX-679, CX-1124, CX-1723 and CX-2234 have much lower uptakes ~0.5 µmol/m^2 . As seen in Table 4.2, the external surface per volume remains constant in these xerogels while the internal micropore surface increases. The lower uptake of CPA may be attributed to a high micropore volumes of the xerogels (0.3-0.9 cc/gm) compared to Darco (0.2 cc/gm). It has been seen in the literature

that platinum hexachloride anion has an octahedral geometry [87]. Based on the solvation chemistry, the hydrated $[PtCl_6]^{2-}$ has an approximate size of ~ 1 nm [88] which may cause some hindrance while attempting to access the micropores. From the micropore size distribution of the xerogels, Figure 4.1a and b, it is clear that the xerogels have a higher volume of micropores than the other carbons. For the PTA adsorption on the low PZC carbons, C-170 and C280, the adsorption maxima was 0.6-0.8 µmol/m^2 close to that predicted for a monolayer (0.84 µmol/m^2). Table 4.1 shows the weight loadings for the catalysts that were prepared using SEA. Although all the catalysts were used for the analysis, only representative catalysts: 2.7Pt/C-170, 2.4Pt/C-280, 10Pt/C-659, 6Pt/CX-679, 12.8Pt/CX-1162, 17.3Pt/CX-1723, 16.4Pt/CX-2234 have been shown in this paper. The remaining catalysts: 6.4Pt/1162, 6.5Pt/CX-1723, 6.5Pt/CX-2234, 10Pt/CX-1162 and 10.3Pt/CX-2234 can be found in the supplementary material.

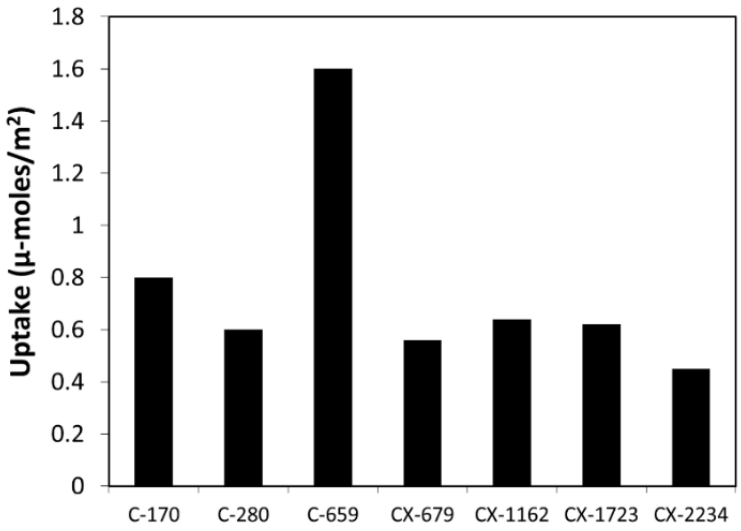

Figure 4.2 Platinum Uptake Comparisons for the different carbon supports

4.3.5 Detection of ambient oxidation in platinum nanoparticles

After drying and reduction, all the carbon supported catalysts were air exposed for a minimum of 2 weeks and then characterized with XRD and STEM. Figure 4.3 and 4.4 show the powder XRD patterns and STEM images respectively for representative catalysts as mentioned in section 3.2 supported on C-170, C-280, C-659, CX-679, CX-1162, CX-1723 and CX-2234 along with the deconvolutions on the inset. All other XRD and STEM data can be found in the supplementary material. The inset of Figure 4.3 shows the deconvoluted peaks that were fit using the Fityk software after the support background was subtracted from the supported catalyst signal. From JCPDS data, the fcc Pt occur as sharp peaks at 2θ values of 39.76°, 46.24° and 67.45° for (111), (200) and (220) reflections respectively whereas the Pt_3O_4 peaks are seen at 2θ values of 35.93 °, 39.49°, 57.08° and 59.64° for the (210), (211), (222) and (320) reflections respectively. From Figure 4.3, a Pt_3O_4 phase is distinctly recognized for the (210) reflection which appears as a shoulder to the (111) Pt peak. The support subtracted signal after deconvolution could only be fit by assuming reflections for a Pt_3O_4 phase. Thus, all the deconvolutions in Fig 4.3 show a combination of both the metal and oxide phases. The imperfections in the signal after support subtraction, details of peak assignment and absence of higher order peaks for the smallest nanoparticles have been discussed in detail in another paper by the same author [78].

Size estimates for both the phases are estimated using the Scherrer equation and are compared with the STEM volume average sizes in Table 4.3. Based on a simplistic model that the Pt_3O_4 phase resides as a thin skin on the platinum nanoparticle core, Table 4.3 shows that the Pt and oxide phases add up to compare fairly well with the

STEM volume average sizes. The metallic fcc Pt peaks are seen as humps very clearly even in the subtracted signal for the three samples with largest metal Pt particle size, the 10Pt/C-659 (Fig. 4.3c), 17.3Pt/CX-1723 (Fig. 4.3f), and 16.4Pt/CX-2234 (Fig. 4.3g). For all the other catalysts, the particle sizes are less than 2 nm and the Pt_3O_4 peak, heavily swamped by the metal peak is detected only after a deconvolution. Hence, all the peaks were deconvoluted to reveal both the oxide and metal phases distinctly. The 17.3Pt/CX-1723 and 16.4Pt/CX-2234 samples were deconvoluted to reveal a bimodal distribution of the metal nanoparticles. This is further confirmed by the STEM images in Figure 4.4e and g respectively.

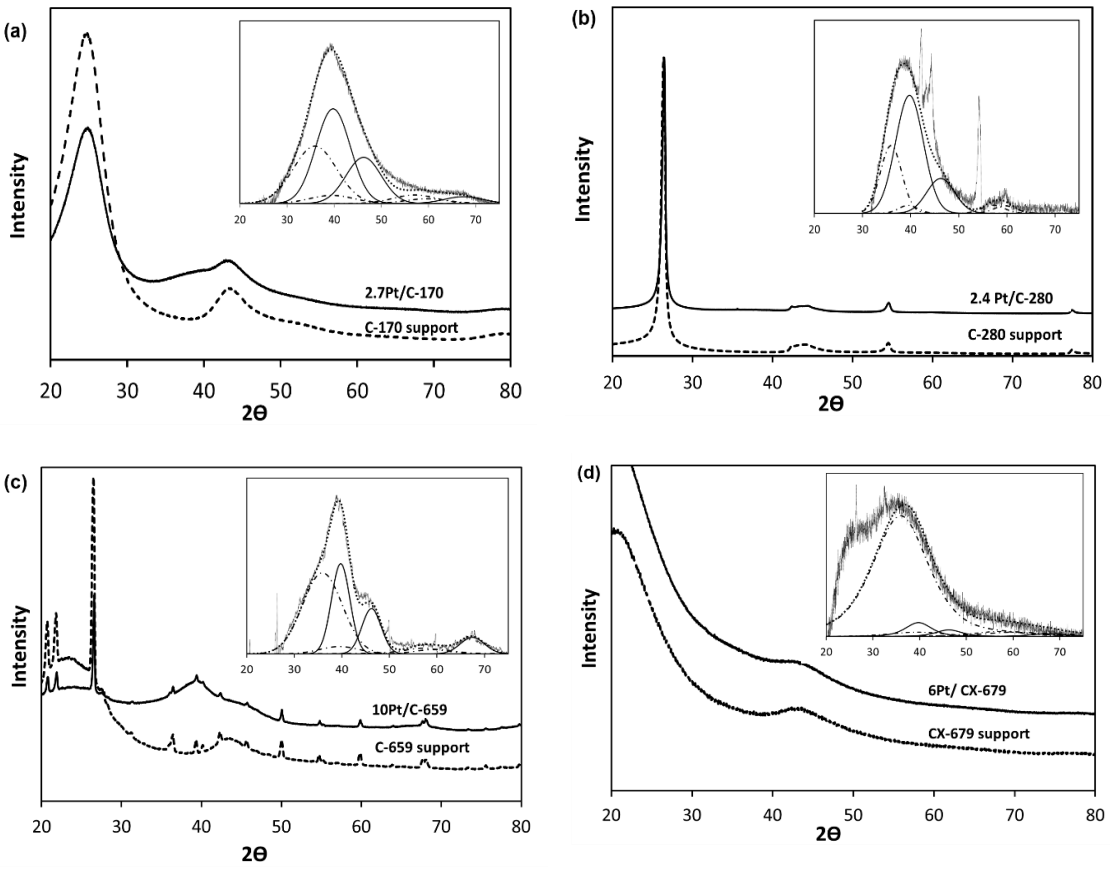

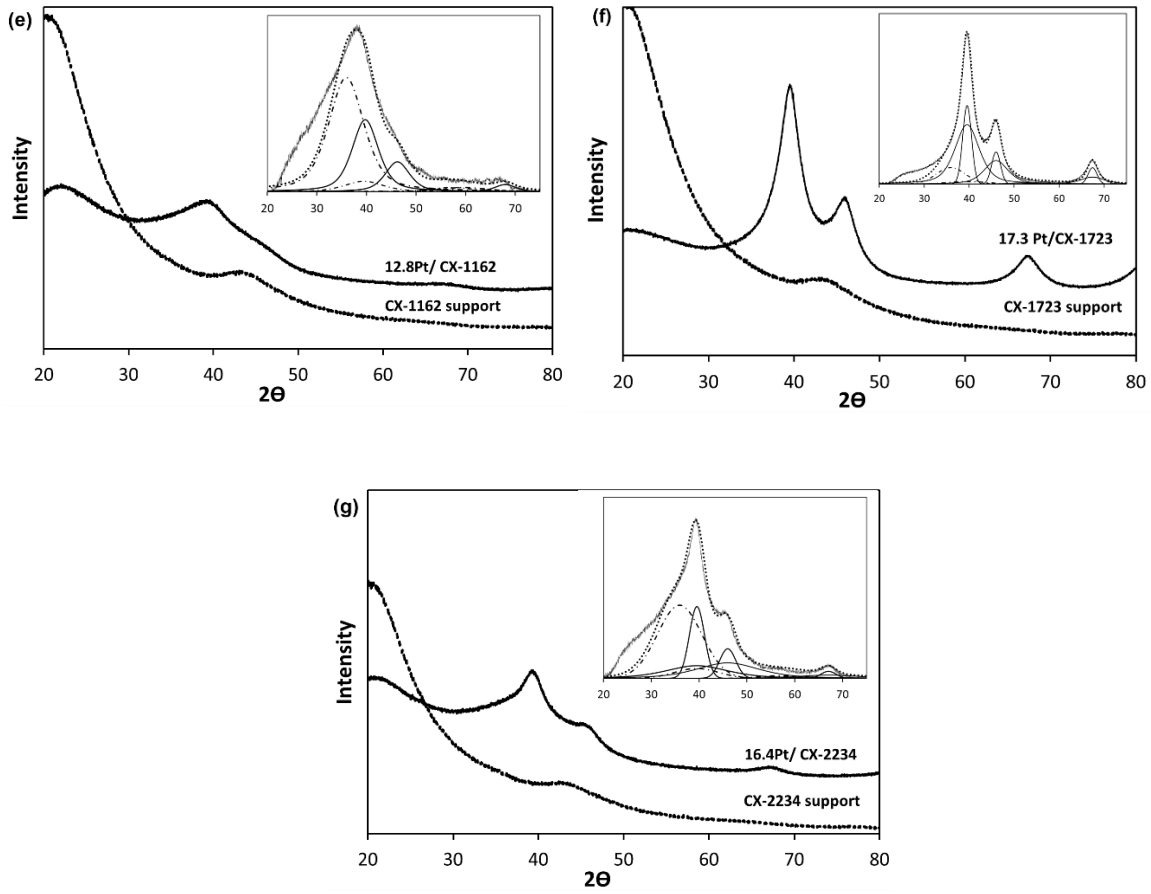

Figure 4.3 XRD Profiles with deconvoluted patterns in the inset for **(a)** 2.7Pt/C-170 **(b)** 2.4Pt/C-280 **(c)**10Pt/C-659 **(d)** 6Pt/CX-679 **(e)**12.8Pt/CX-1162 **(f)** 17.3Pt/CX-1723 **(g)** 16.4Pt/CX-2234

Table 4.3 XRD and STEM particle sizes

Catalyst	XRD Sizes (nm)			STEM Volume Average Sizes (nm)
	Pt	Pt_3O_4	$Pt+Pt_3O_4$	
2.7Pt/C-170	0.9	0.8	1.7	1.5±0.3
2.4Pt/C-280	1.1	1.0	2.1	1.6±0.2
10Pt/C-659	1.8	0.9	2.7	2.2±0.4
6Pt/CX-679	0.8	1.1	1.9	1.4±0.5
6.4Pt/CX-1162	1.3	0.6	1.9	1.5±0.4
10Pt/CX-1162	2.0	0.7	2.7	1.7±0.4
12.8Pt/CX-1162	1.4	1.0	2.4	1.9±0.4
17.3Pt/CX-1723	3.6	1.1	4.7	3.9±1.5
6.5Pt/CX-1723	1.4	0.8	2.2	1.5±0.4
6.5Pt/CX-2234	1.0	1.0	2.0	1.4±0.5
10.3Pt/CX-2234	2.2	0.7	2.9	1.8±0.4
16.4Pt/CX-2234	1.6	0.8	2.4	2.8±1.0

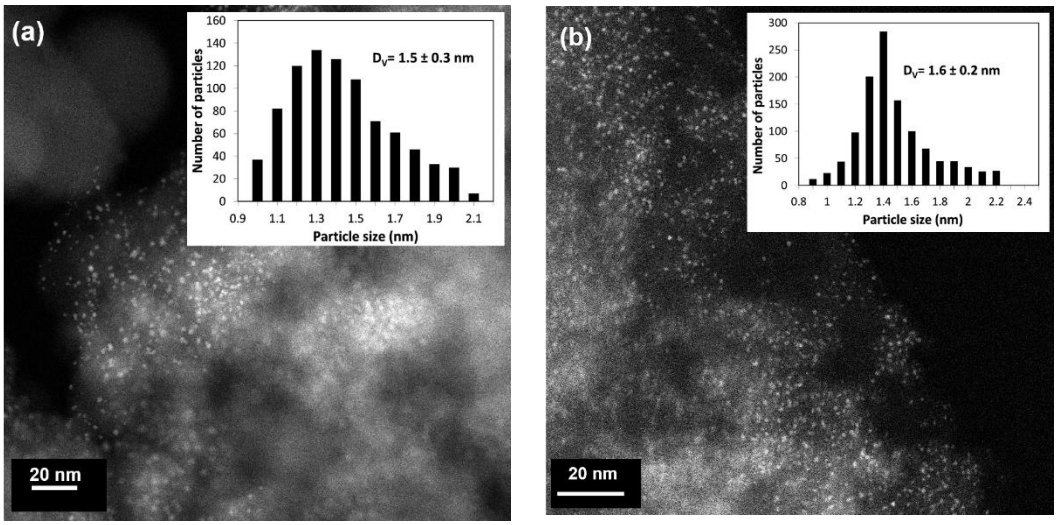

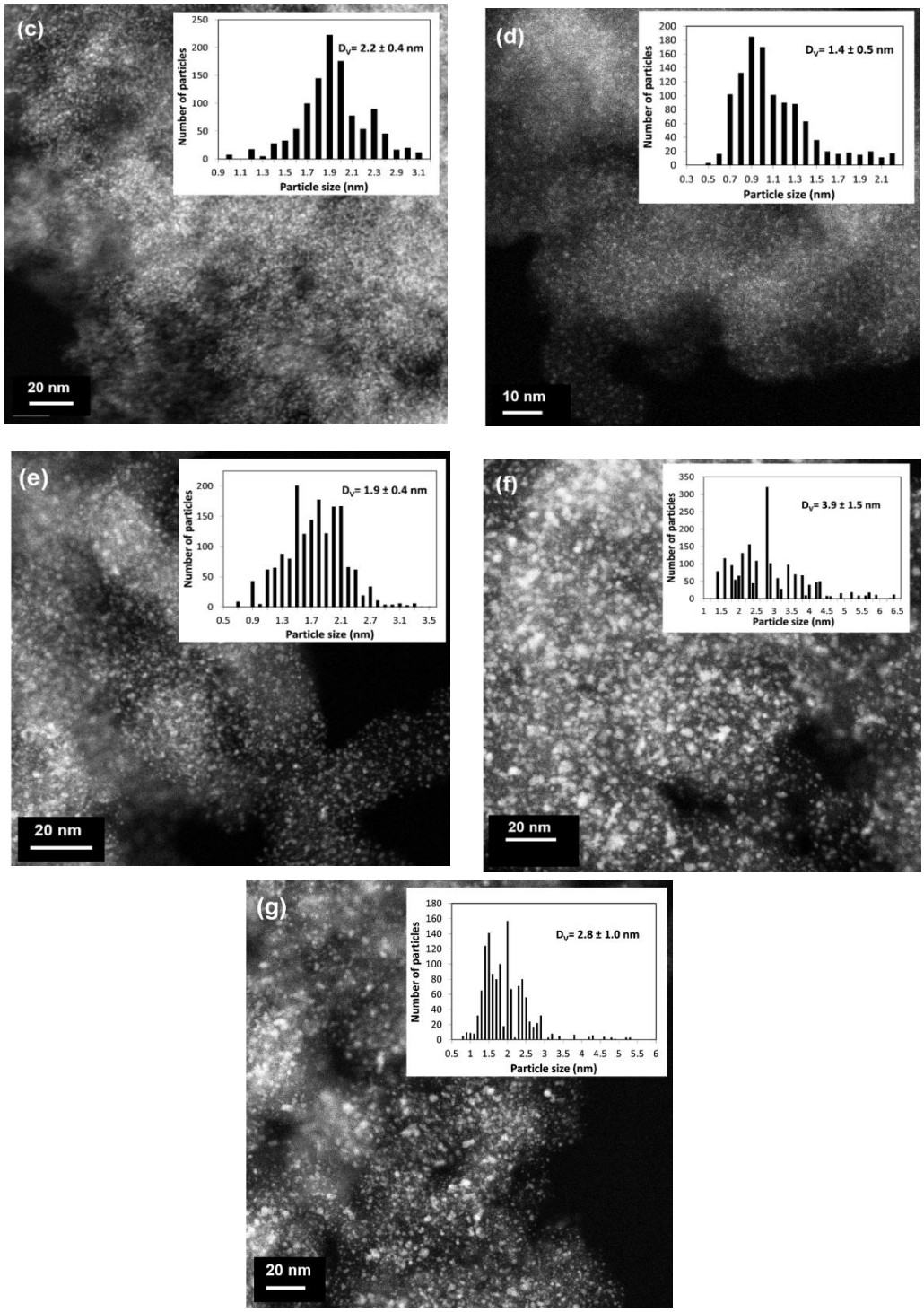

Figure 4.4 STEM images with particle size distribution histograms in the inset for **(a)** 2.7Pt/C-170 **(b)** 2.4Pt/C-280 **(c)** 10Pt/C-659 **(d)** 6Pt/CX-679 **(e)**12.8Pt/CX-1162 **(f)** 17.3Pt/CX-1723 **(g)** 16.4Pt/CX-2234

XRD and STEM analysis were able to show that all the nanoparticles showed both the metal and oxide phases, though the intensity of the phases were variable. It would thus, be interesting to derive a relationship between the extent of oxidation and particle size with an FFT analysis of individual, atomically resolved particles. HAADF STEM imaging has been performed with the catalysts: 2.7 Pt/C-170, 10% Pt/C-659 in another work [78] which revealed 0.23 nm and 0.25 nm d-spacings corresponding to the most intense reflections from the crystalline planes (111) of Pt with an fcc cubic structure (JCPDS Card no: 00-004-0802) and (210) planes of Pt_3O_4 (JCPDS Card no: 01-089-2356) with a bcc cubic structure respectively. A representative image of the analysis is shown in Figure 4.5. It was concluded from this work that platinum nanoparticles smaller than 2.5 nm had an inherent susceptibility to oxidation : below 1.5 nm, they existed only in the oxide phase; in the range of 1.5 to 2.5 nm, they existed in a combination of both metallic and oxide phases while above 2.5 nm, it was all metallic. Based on the STEM histograms in Figure 4.4, it is seen that all the catalysts have nanoparticles that traverse this sensitive size domain: so, they would all contain a mixture of both metal and oxide.

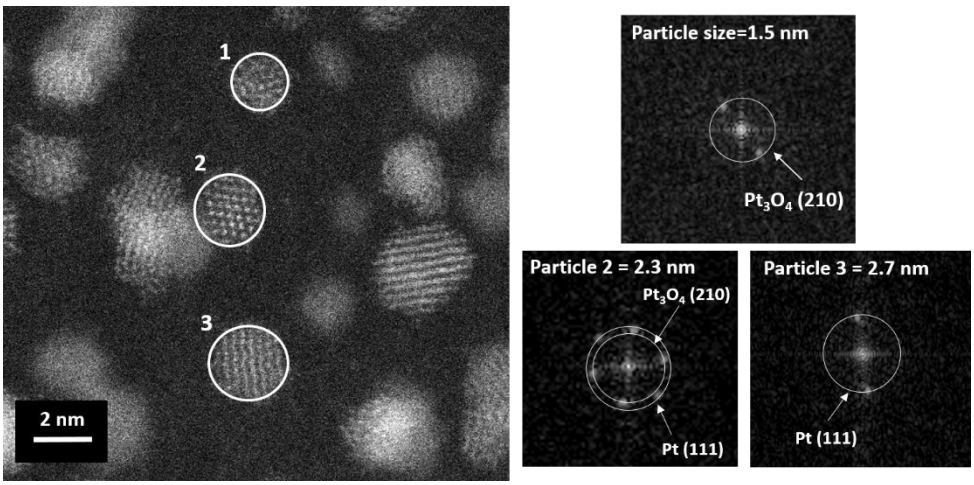

Figure 4.5 HRTEM images with inset FFT patterns for 10Pt/C-659 after air exposure

4.3.6 Quantification of oxide in platinum particles using X-Ray Photoelectron Spectroscopy (XPS)

XPS was used to determine the oxidation state of the platinum nanoparticles. Although XPS is a technique used to characterize the surface composition (within 0-10 nm) of a material, the nanoparticles in question here, are all small enough such that most of their atoms are surface atoms. Hence, XPS would reflect the bulk oxidation state for these catalysts quite well [54]. Figure 4.6 shows the Pt 4f XPS peaks for the representative air exposed catalysts that have been deconvoluted using XPS peak 4.1 software. All the nanoparticle spectra were referenced to the binding energy (BE) of the C 1s peak at 284.8 eV. All the samples were reduced in-situ in H_2 at 200°C for 1 hr to determine the position of the Pt $4f_{7/2}$ and $4f_{5/2}$ peaks. The fits of the XPS spectra were done after the subtraction of a Shirley background using an asymmetric line-shape-function of the XPS Peak 4.1 software. The obvious asymmetry of the Pt4f peak was fit with a mixed Gauss-Lorentzian function. The signal was deconvoluted using three doublets corresponding to metallic Pt (Pt $4f_{7/2}$ ~ 71.1 eV), PtO (Pt $4f_{7/2}$ ~ 72.3 eV), and PtO_2 (Pt $4f_{7/2}$ ~ 73.8 eV) .The maximum width (fwhm) of each component was held constant at 1.2 eV for Pt^0, 1.7 eV for PtO and 1.9 eV for PtO_2 [77]. The continuous line depicts Pt(0), dashed lines show Pt(II) and dot-dashed lines refer to the Pt (IV) peaks. Although the XRD results clearly depict the existence of a Pt_3O_4 species, the resolution of the laboratory XPS system is incapable of distinguishing between the binding energies of Pt_3O_4 from PtO_2. Moreover, as has been mentioned before in the literature [89, 90], an intermediate binding energy between that of PtO and PtO_2 is expected for the Pt_3O_4 species since the Pt oxidation state in Pt_3O_4 is in between the two species. Hence, all fits in this paper were done using Pt^0 and a combination

of the two oxides. As confirmed by XRD and STEM in Section 3.3, Figure 8 also confirms the presence of metal and oxide for all the samples.

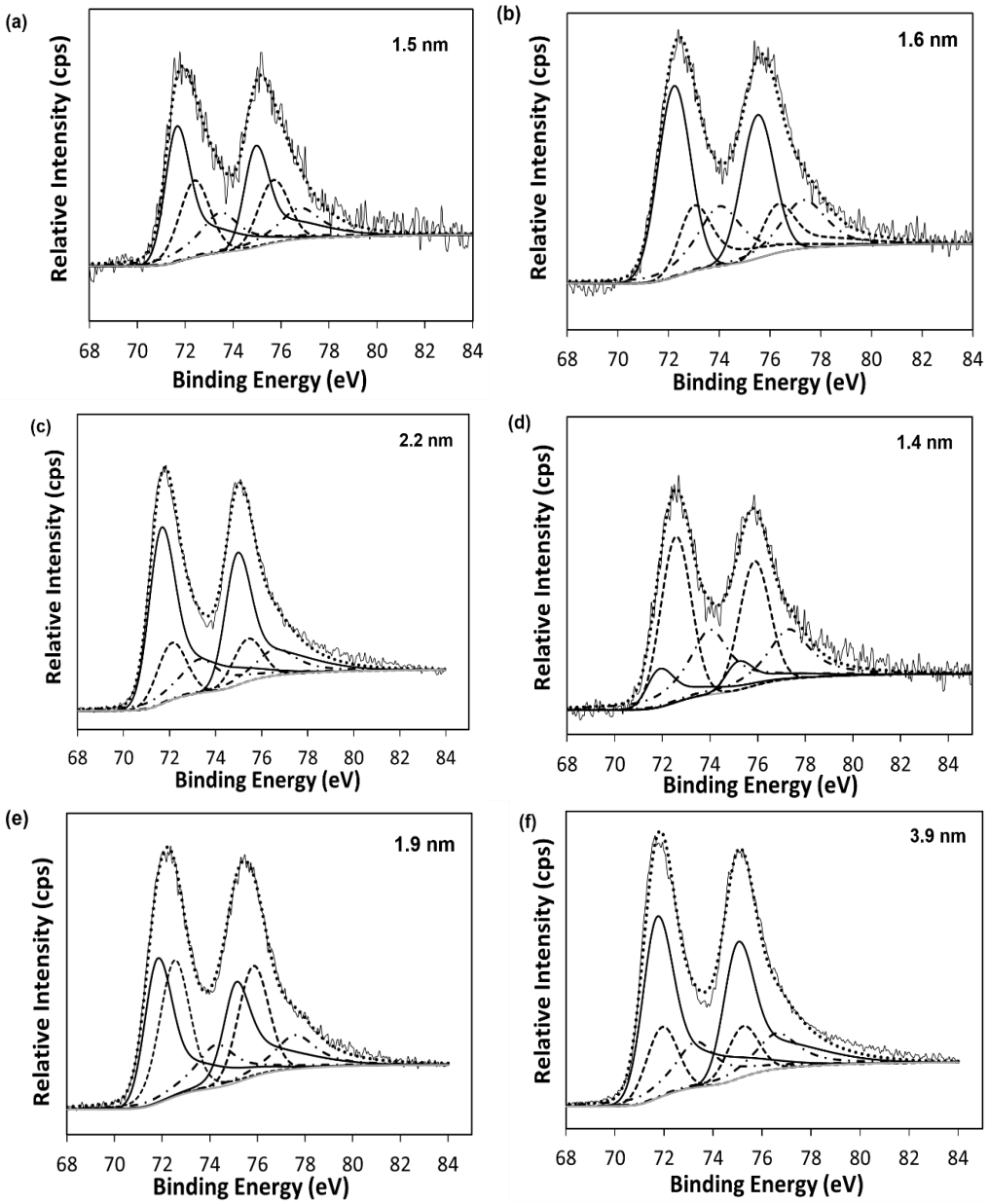

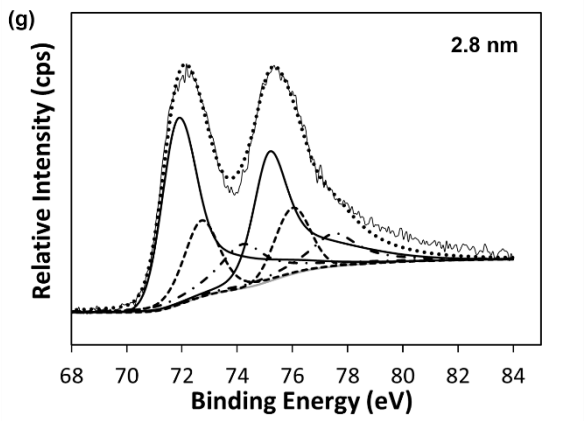

Figure 4.6 Deconvoluted XPS spectra with STEM Volume average sizes in the inset for (a) 2.7Pt/C-170 (b) 2.4Pt/C-280 (c)10Pt/C-659 (d) 6Pt/CX-679 (e)12.8Pt/CX-1162 (f) 17.3Pt/CX-1723 (g) 16.4Pt/CX-2234

An in-situ XPS experiment was performed on the 6.9Pt/CX-679 sample to compare the binding energy shifts of the Pt 4f and the corresponding O1s shifts with different pretreatments. The catalyst samples that were compared are the short time air exposed catalyst, the long time air exposed catalysts, in-situ reduced and in-situ oxidized catalysts. Figure 4.7 shows the binding energy shifts of the Pt 4f and O1s with the different pretreatments. In situ reduction for 1 hr in H_2 at 200°C was conducted to determine the position of the reference Pt 4f peak and the corresponding O1s peaks. It is noticed that the intensity of the O1s peak in the in-situ reduced catalyst is higher than the intensity of the bare CX-679 support without any metal. This may be due to the presence of trapped oxygen in the carbon support that may travel to the surface during the reduction treatment at 200℃ in hydrogen. This O1s peak is therefore, taken as the reference for comparison with the other catalysts.

Figure 4.7a depicts obvious positive shifts in the Pt4f peak positions with increased air exposures, the shift being the maximum when it is oxidized in-situ in oxygen in the

UHV chamber. However, the short time and long time air exposed samples show a positive shift which is in between the binding energies for the in-situ reduced and in-situ oxidized catalysts which confirms the presence of platinum oxide. The long time exposed samples shows a shift of about +0.6 eV more than the in-situ reduced Pt compared to a shift of about +1eV for bulk platinum with (111) crystal surfaces. This is possibly due to the fact that smaller nanoparticles have a different morphology and are comprised of a combination of (111) and (100) surfaces which would also cause a difference in their chemical shifts [77] A small positive binding energy shift (~0.4 eV) is observed in the overnight air exposed sample.

Figure 4.7b shows a comparison of the corresponding O1s XPS peaks. The shifts compare very well with the Pt4f peaks and the short and long time air exposed samples have shifts that are in between the two extremes: no platinum oxide for the in-situ reduced sample and platinum oxide in the in-situ forced oxidation sample. Hence, the O1s peaks can be deconvoluted to give a combination of the two peaks due to the presence of oxygen from the reduced catalyst support and the oxide from the platinum oxide formed (Figure 4.8)

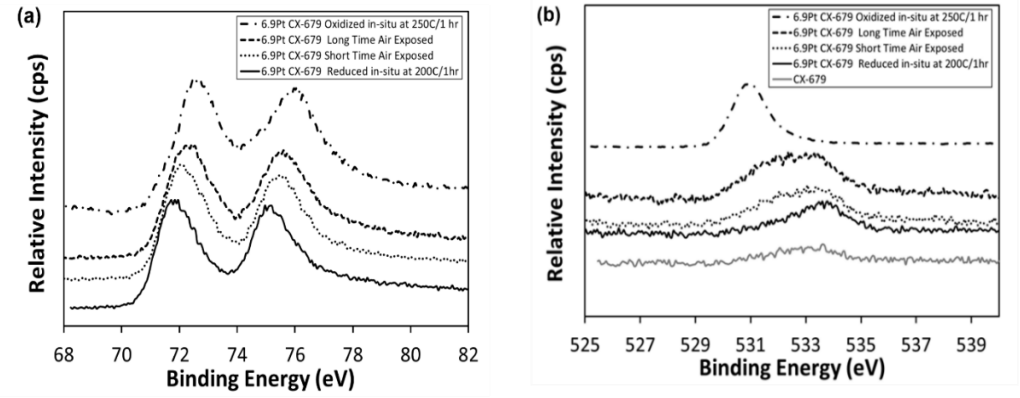

Figure 4.7 XPS binding energy shifts for (a) Pt4f and (b) O1s after different treatments for the 6.9Pt/CX-679 catalyst

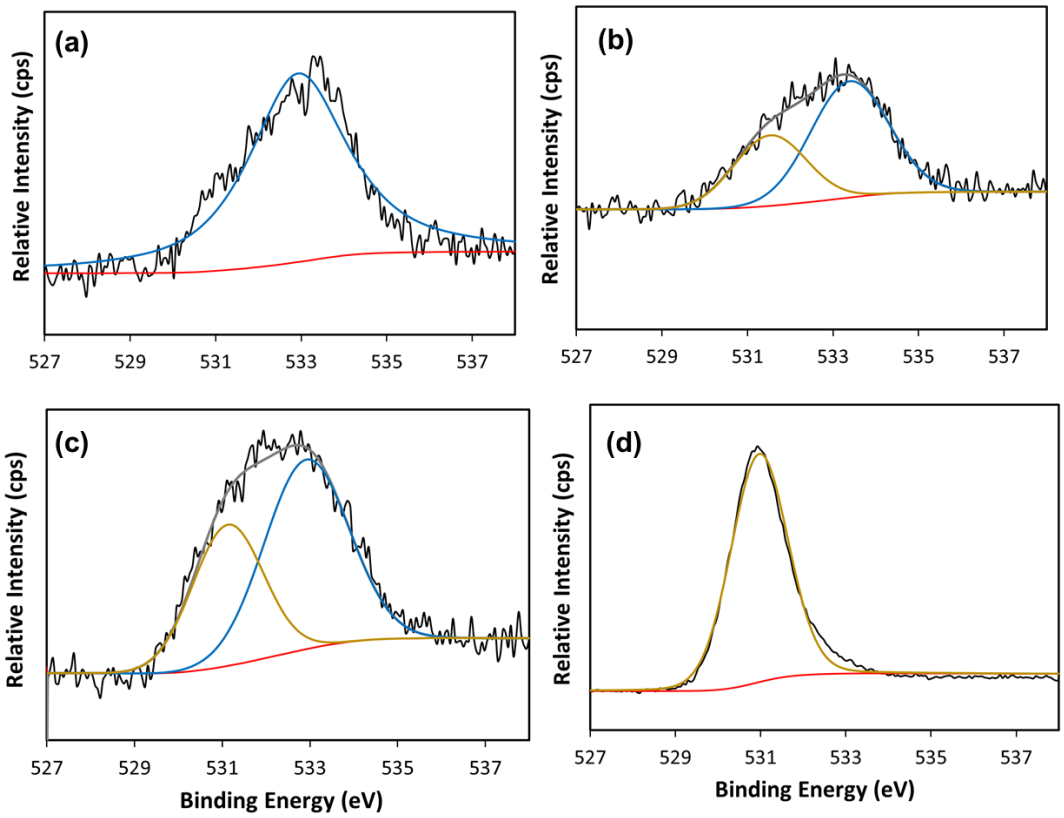

Figure 4.8 XPS binding energy deconvolutions for the O1s peaks of the 6.9Pt/CX-679 catalyst (a) after in-situ reduction in hydrogen at 200℃ (b) after short time air exposure (c) after long time air exposure (d) after in-situ oxidation in oxygen at 250℃

The platinum and platinum oxide content were determined from XPS data and are tabulated in Table 4.4. In order to test our hypothesis that micropore volumes may be responsible for causing the oxidation in the platinum nanoparticles, the micropore volumes and STEM volume average sizes were also included in the table. The oxide content represents the sum of the Pt (II) and Pt (IV) oxide phases. The oxide content for the metal nanoparticles range from ~ 29% to ~87%.

Figure 4.9 is a variety of plots showing the variation of nanoparticle size with metal loading (4.8a) and micropore volume (4.9b) and oxide content as determined from XPS

plotted as a function of nanoparticle size (4.9c) and micropore volume (4.9d). The general trend in Figure 4.8a is a sharp upturn in nanoparticle size with increased metal, with the exception of the two high surface area carbons with low micropore volumes, C-1189 and C-1474. The largest two particle sizes are for the highly loaded, high microporosity supports (17.3Pt/CX-1723 and 16.4Pt/CX-2234). This suggests a relationship between high microporosity and large particle size at high metal loading. This is seen more clearly in Figure 4.9b, in which particle size is plotted versus micropore volume. The sizes lie in a somewhat narrow range for most of the samples with the exception, again, of the two high metal loading, high microporosity catalysts. For the three sets of xerogel samples at the highest micropore volumes of 0.47, 0.70, and 0.89 cc/gm, the trend of increasing particle size with increasing metal loading is especially apparent.

The variation of oxide content with nanoparticle size is shown in Figure 4.9c. There is a simple, clear trend of increasing oxide content with decreasing particle size, independent of support, as was shown in Chapter 3. The phenomenon for oxide content dependence on nanoparticle size has already been described in the literature [54, 55, 77, 78]. Figure 4.9d, in which oxide content is plotted versus micropore volume, helps refine this dependence on weight loading and micropore volume, again seen most clearly for the xerogel series. The four samples with the highest oxide content are the xerogels with low metal loading, substantially below the precursor monolayer limit. The xerogel samples synthesized at loading closer to the monolayer limit are those which have higher metal loading (Fig. 4.9a) and higher particle size (Fig. 4.9b). In fact, the 10Pt/C-659 sample, with larger-than-average particles of 2.2 nm, is also near the precursor monolayer limit.

In view of the above discussion, it is surmised that the primary variable determining oxide content is metal particle size. The role of the microporosity of the carbon on metal stabilization is only indirect; in fact, precursors adsorbed into micropores at high surface density (near monolayer coverage) yield the largest particles, and it is the large size which stabilizes the particles to oxidation. This study appears to be the first to demonstrate the deleterious effect of microporosity on particle size at high metal loading, and is somewhat counterintuitive, as small pores might normally be thought to stabilize the smallest particles. It could be that the Pt-Pt interactions in forming nanoparticles are stronger than the carbon material and the pores break as the particles grow. It will be the subject of future study to compare the effect of micropores of carbon to those of oxide supports.

Table 4.4 Summary of micropore volumes, STEM volume average sizes and oxide content of the catalysts

Catalyst	Total Micropore Volume (cc/gm)	STEM Volume Average Sizes (nm)	Percentage of Oxide
2.7Pt/C-170	0.02	1.5	48
2.4Pt/C-280	0.006	1.6	73
10Pt/C-659	0.15	2.2	29
6Pt/CX-679	0.27	1.4	87
6.4Pt/CX-1162	0.47	1.5	87
10Pt/CX-1162	0.47	1.7	44
12.8Pt/CX-1162	0.47	1.9	40
17.3Pt/CX-1723	0.7	3.9	32
6.5Pt/CX-1723	0.7	1.5	85
6.5Pt/CX-2234	0.89	1.4	86
10.3Pt/CX-2234	0.89	1.8	39
16.4Pt/CX-2234	0.89	2.8	33
27Pt/C-1189	0.2	1.8	-
30Pt/C-1474	0.21	1.7	-

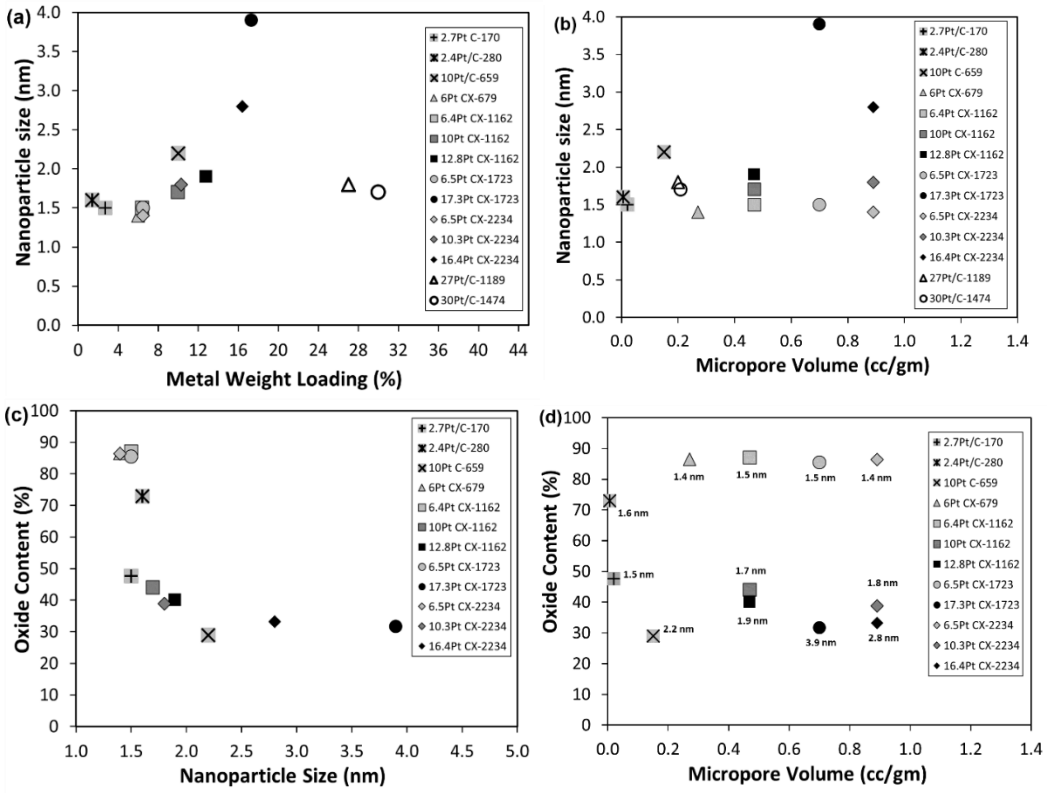

Figure 4.9 Variation of Nanoparticle size with (a) metal weight loading (b) micropore volume; variation of oxide content with (c) nanoparticle size (d) micropore volume for all the catalysts

4.4 Conclusion

A variety of characterization techniques, XRD, STEM, XPS show that the spontaneous oxidation of ultrasmall platinum nanoparticles is dependent mainly on the size of the Pt nanoparticles, consistent with Chapter 3. The microporosity of the carbon support plays an indirect role at high metal weight loadings, where the accumulation of high amounts of metal precursor leads to large, oxidation-resistant particles.

CHAPTER 5

RATIONAL SYNTHESIS OF PLATINUM NANOPARTICLES ON SPECIALTY CARBONS USING STRONG ELECTROSTATIC ADSORPTION

5.1 Introduction

Carbon materials in the form of fibers and tubes are of great significance as catalyst supports owing to their high specific surface area, mechanical strength and flexibility. Carbon nanofibers could be grown by passing carbon feedstock over nanosized metal particles at high temperatures which is similar to the growth process of carbon nanotubes. However, nanofibers differ in their geometry from concentric nanotubes containing an entire hollow core and can be visualized as regularly stacked truncated conical or planar layers along the filament length, Figure 5.1 [92]. Figs 5.2a and b show the TEM images of a nanofiber that exposes only basal planes versus fibers that show only the graphite edge being exposed, that is often referred to as fishbone/herringbone nanofibers. Since the parallel fibers always contain a hollow core, they are often referred to as carbon nanotubes [93].

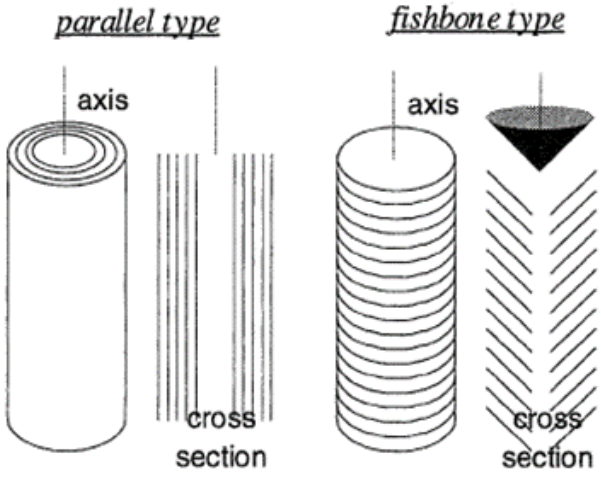

Figure 5.1 Schematic Comparison of the various types of carbon nanofibers

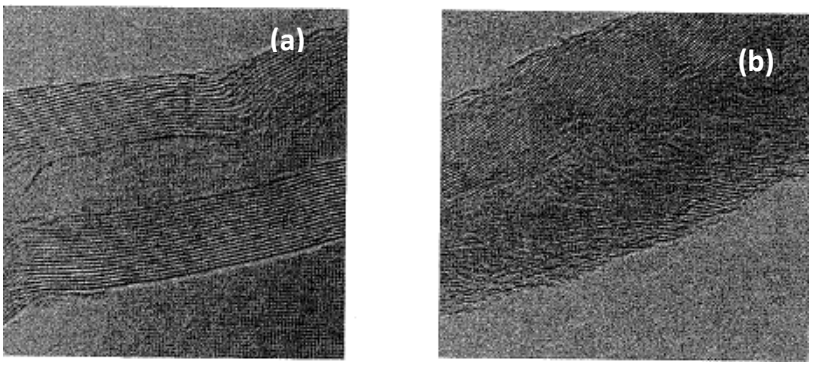

Figure 5.2 Carbon nanofibers showing (a) basal planes (b) herringbone fibers

Despite the desirable attributes of the nanofibers/nanotubes, their hydrophobicity, chemical inertness and surface impurities hinder commercial utilization and hence, they need to be chemically modified to overcome the limitations. The most common way to activate the surface is oxidation using nitric acid, sulphuric acid or a combination of both. The oxidative treatment enhances the hydrophilicity and as a consequence, the wettability of the support. It has been seen that the ends of oxidized MWCNT are opened by nitric acid oxidation resulting in an increase in surface area by about a factor of about 2, Figure 5.3 [94].

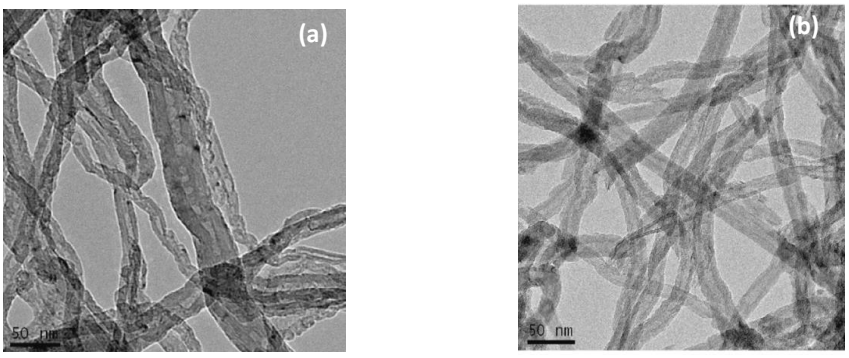

Figure 5.3 TEM image of (a) as-received MWCNT, (b) 15M HNO3 treated MWCNT

Carbon nanofibers have been extensively used as catalyst support materials during the past years. Planeix and co-workers prepared Ru/C catalysts based on carbon nanotubes in an arc-discharge experiment [95]. The average Ru-particle size shown by TEM was 3.5 nm. Such catalysts showed a much higher selectivity towards the hydrogenation of cinnamaldehyde compared to conventional Ru/C catalysts which was accounted to a strong metal-support interaction in the former case. Pd nanoparticles have been introduced via ion-exchange with a Pd-ammonia complex at pH=5-6 [96]. The metal loading achieved was about 3wt% with a particle size of 1.5 nm. However, the drying process induced extensive sintering in the nanoparticles.

Apart from all the different impregnation methods used, literature review has shown that the SEA method can be successfully used to synthesize palladium nanoparticles around 1 nm on carbon nanotubes [97]. All the nanotubes were oxidized in nitric acid or mixtures of nitric acid and sulphuric acid to introduce varying degrees of oxygen functionalities and make the surfaces more hydrophilic so that a polar solvent can be used. Since the metallic dispersion is highly dependent on the surface composition and porous structure/ surface area of the support, the acid pre-treatment is beneficial for the impregnation as it creates more functional groups for the metal to anchor.

Pt nanoparticles tethered to functionalized carbon nanotube supports have been studied during various stages of the nanomaterial synthesis using XPS, EXAFS and IR spectroscopy [98]. It was shown that sonication of the MWCNTs tend to create dangling bonds on the surface of the nanotubes which progressively oxidize to hydroxyl, carbonyl and carboxyl groups. Controlled surface functionalization can influence the PZC of the support which is an important variable in the Strong Electrostatic Adsorption (SEA).

Cobalt supported on carbon nanotubes have also been synthesized using the SEA method for applications in Fischer Tropsch synthesis to produce hydrocarbons [99]. The STEM images indicated that acid treatment opened the caps of the closed nanotubes and introduced some defects on the surface of the CNTs which led to better metal dispersion.

As mentioned before, SEA is a simple and rational approach for creating highly dispersed metal catalysts on a wide variety of supports. Carbon supported metal catalysts find a great deal of applications in liquid phase hydrogenation reactions, fuel cell as well as fine chemical synthesis. In this study, SEA has been extended to synthesize Pt- metal nano-particles on a number of specialty carbons. The carbons used in the study comprise a set of multi-walled carbon nanotubes with varying surface functional groups and orientation of graphene sheets. The goal is to analyze the effects of the surface impurities and functional groups on the adsorption of metal and develop a rational method to achieve maximum dispersion of platinum nanoparticles on these specialty carbons to agglomerate.

5.2 Experimental

5.2.1 Specialty Carbons

The term “specialty carbons” has been coined by the authors to designate carbons like multiwalled carbon nanotubes, nanofibers, graphene nanoplatelets, graphene oxides etc for reasons stated later. The specialty carbons used in the study comprise a set of multi-walled carbon nanotubes with varying aspect ratio, surface functional groups and orientation of graphene sheets. Some of the carbons were un-oxidized whereas some were obtained in the oxidized form from the manufacturer. Table 5.1 below gives a summary of the types of carbon used, their BET surface areas, PZCs and type of precursor. The carbons

used in the study as listed in Table 5.1: for MWCNT I and Herringbone nanofibers were obtained from Sigma-Aldrich, USA and the other carbons: MWCNT II, MWCNT II-OH and MWCNT II-COOH were obtained from Nanostructured and Amorphous Materials, Inc, USA. The method for determining the PZC and choosing the right precursor for SEA has already been discussed in Chapter 2. After determining the point of zero charge, the appropriate precursor, (PTA, Platinum Tetraammine or CPA, Chloroplatinic acid: Sigma-Aldrich, USA) was chosen to perform the uptake experiment in order to determine the optimal pH of adsorption. As shown in the table, both the precursors were evaluated for all the carbon supports. As the standard for SEA, 1000 m^2/l surface loading was used for cations and 500 m^2/l was used for the anions.

One of the carbon nanotubes, MWCNT I was oxidized in boiling nitric acid was 3 hrs to study the effect of oxygen functionalities on the adsorption on nanotubes.

Table 5.1 Specialty carbons along with their PZCs, pore volumes, BET surface areas: PV represents the pore volume at incipient wetness

Carbon Type	PZC	Oxidized	Precursor	BET SA (m^2/gm)
MWCNT I (OD X ID xL: 10 nm X 4.5 nm x 3-3micrometer)	5.4	No	PTA/CPA	301 PV=12.2 ml/gm
MWCNT I Oxd(OD X ID xL: 10 nm X 4.5 nm x 3-3micrometer)	2.7	Yes	PTA/CPA	308 PV= 9.8 ml/gm
Nanofibers (HerringBone) (D X L: 100nm x 20-200 micrometer)	3.8	No	PTA/CPA	54 PV=7.65 ml/gm
MWCNT II (OD X ID x L: <8 nm X 2-5 nm x 10-30 micrometer)	9.3	No	PTA/CPA	302 PV=1.6 ml/gm
MWCNT II-OH (OD X ID x L: <8 nm X 2-5 nm x 10-30 micrometer)	5.9	Yes (from Manufacturer)	PTA/CPA	558 PV=2.4 ml/gm
MWCNT II-COOH (OD X ID x L: <8 nm X 2-5 nm x 10-30 micrometer)	3.1	Yes (from Manufacturer)	PTA/CPA	416 PV=1.8 ml/gm

5.2.2 Washing protocol for specialty carbons

The specialty carbons were first washed with deionized water at a pH of 5.8 and then, with acid or base depending on the PZC: acid wash for high PZC carbons and base wash for low PZC carbons. For the washing procedure, a solution about 10 times in excess of the pore volume of the carbon support was employed, and the mixtures were shaken for 1 h, and then filtered. The washing solutions use were a deionized water with a pH of 5.8 for all supports, acidic HNO_3 solution at a pH of 2 for the high PZC supports and basic solution of pH12 NaOH solution for those samples with the low PZCs. The filtered samples were dried overnight in ambient air followed by drying overnight in static air at 120℃. The dried samples were again washed using deionized water with pH 5.5 in a dialysis bags for 24 hrs and filtered followed by drying under the same conditions.

5.2.3 Adsorption surveys of pre and post washed samples

Adsorption surveys were performed over the entire range of pH using both PTA and CPA on the as-received specialty carbons. Depending on the pre-wash uptake, the adsorption surveys were repeated on the post washed carbons using the precursor that gave the highest uptakes before the washes. All the catalysts were then prepared at the optimum pH and subsequently dried and reduced to obtain the supported platinum nanoparticles.

5.2.4 X-Ray Photoelectron Spectroscopy (XPS)

XPS Survey scans were conducted on the all the bare nanotube supports to check for the presence of surface impurities remaining from the manufacturing process. The OIs peaks for all the supports were also monitored.

5.3 Results and Discussion

Figure 5.4 shows the changes in the PZC of the carbons before and after the washes. While the deionized water did not affect the PZCs of the specialty carbons significantly, the acid/base washes found to decrease or increase the PZC. For the MWCNT-I and Herringbone nanofibers, the neutral DI water washes did not affect the PZCs but the base washes caused an increase in the PZC. The OH-functionalized nanotubes were affected by the DI wash as well as the base wash that led to an increase in the PZCs. This is an indication of the presence of acidic impurities like Cl^-, NO_3^- which have been known to artificially decrease the PZC [100]. The acid washed carbons MWCNT-II led to a decrease in the PZC which leads to the conclusion that they may have had residual metal impurities which rendered a high artificial PZC. The neutral wash did not cause any change in the PZC.

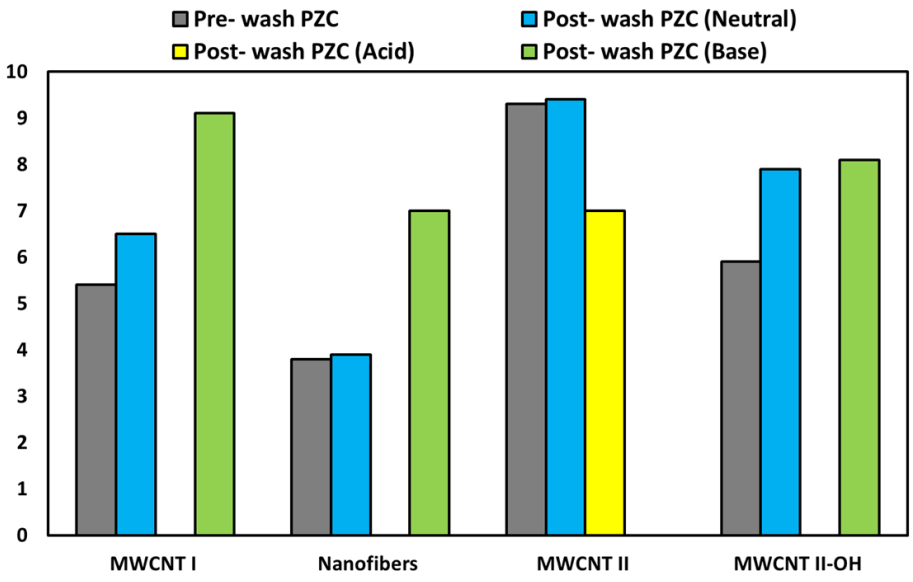

Figure 5.4 PZC variations of specialty carbons with acid, base and neutral washes

Figure 5.5 shows the uptake curves for the carbons in the as-received form without any washing as well as the post wash uptakes. From prior work done in the group and literature, it is known that the maximum Pt uptake when the anionic precursor (CPA) is used should be 1.4 μ-moles/ m^2 and 0.8 μ-moles/m^2 for the cationic precursor. The specialty carbons displayed volcano-shaped uptake curves typical of electrostatic adsorption for both Pt anions at low pH and Pt cations at high pH.

From Table 5.1, it is seen that the as-received MWCNT I, HB nanofibers, MWCNT-OH were low PZC supports and so, PTA was used as the precursor. However, from Figure 5.5a, b, d, it is seen that there is no uptake of the cation. On the other hand, using the anionic precursor, CPA gives good uptake for all the four low PZC supports. From Figure 5.4, it has already been seen that base wash had shifted the PZC to higher values. This explains the fact why anionic precursors are taken up by the support while cationic ones are not. The change in PZC may be attributed to the presence of residual surface impurities on the nanotubes as a result of the manufacturing process that render an artificial PZC to the support. The post base wash uptakes did not show any change in the uptake regime or maxima although the PZC changed. So, the presence of impurities change the PZC of the support but the uptakes remain unaltered. Hence, it is not necessary to introduce any washing step prior to synthesizing the catalysts at the optimum pH of adsorption.

Figure 5.5c shows that the high PZC MWCNT II showed good uptake using the anionic precursor. This becomes evident from Figure 5.4 where even after the acid wash, although the PZC changes to lower values, the support is still sufficiently basic to take up

anions as opposed to cations. Again, post acid wash, there was no change in either the anionic or cationic uptakes.

Figure 5.5e shows the pre wash uptake plot for the COOH functionalized MWCNT. Based on the acidic PZC, only the cationic precursor should ideally give a good uptake, however, it is seen that the uptake is good using both PTA and CPA. From prior results, this is an indication that this nanotube may have a PZC in the mid range which is good for both cationic and anionic adsorption.

Figure 5.5f shows the uptake for the oxidized MWCNT I. This is the only low PZC carbon other than the COOH functionalized nanotube (MWCNT-COOH) that showed good uptake for the cationic precursor.

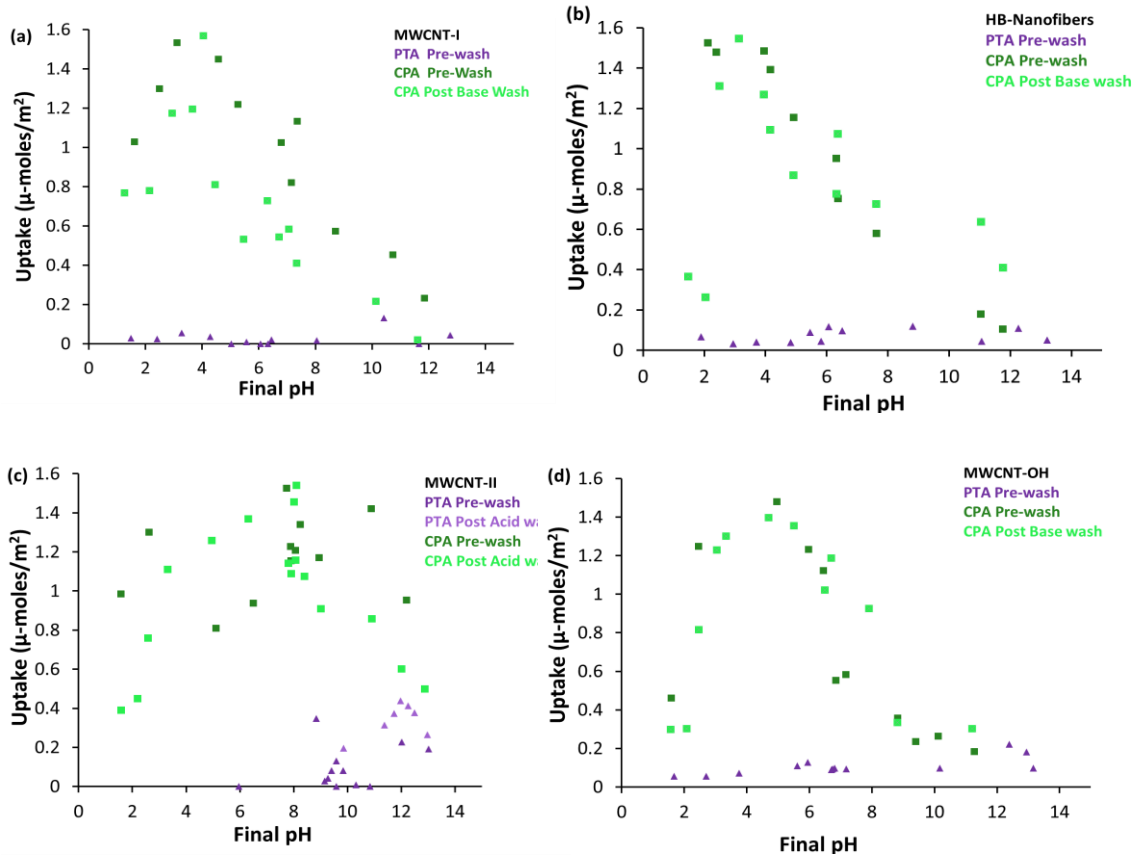

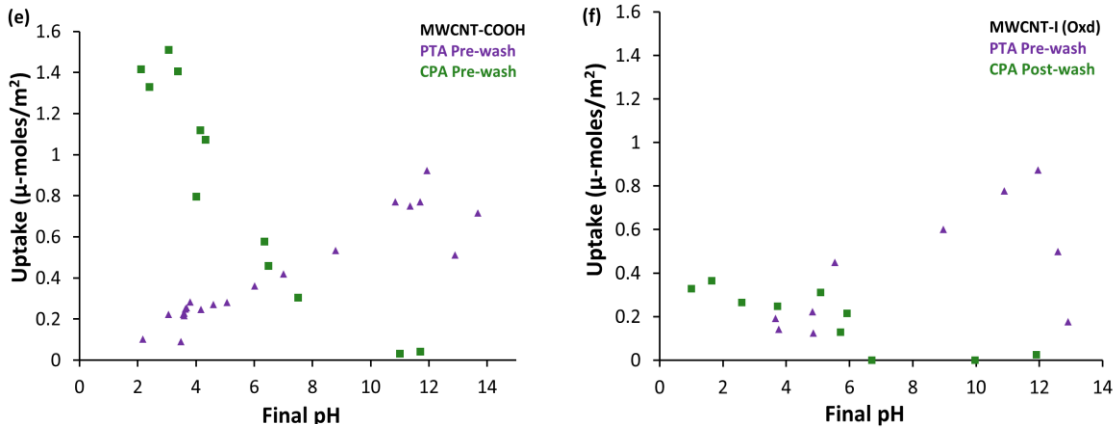

Figure 5.5 Prewash and post wash uptakes using PTA and CPA for (a) MWCNT I (b) HB Nanofibers (c) MWCNT II (d) MWCNT-OH (e) MWCNT-COOH (f) MWCNT I-Oxidized

It has been seen in earlier work in the JR group that acidic impurities like Cl^- or NO_3^- are known to shift the PZCs down to the acidic regime while metallic impurities like Ca^+, K^+ etc are known to move up the PZCs to the basic regimes [100]. Figure 5.6a shows that small traces of Fe or Co are detected on the MWCNT II which may be responsible for the pre wash basic PZC observed. The lowering of PZC after the acid washes signifies removal of these impurities. However, figure 5.6a shows that the XPS plots for the acidic PZC specialty carbons that does not detect any impurities. Hence, these impurities are below the detection limit of XPS but significant enough to affect the PZC, however, not large enough to affect the platinum adsorption.

Figure 5.6b shows the corresponding O1s peaks for all the specialty carbons. The MWCNT I has a significantly less amount of oxygen compared to the other carbons which increases significantly upon oxidation. However, the oxygen content could not be directly related to the uptake patterns observed in the specialty carbons.

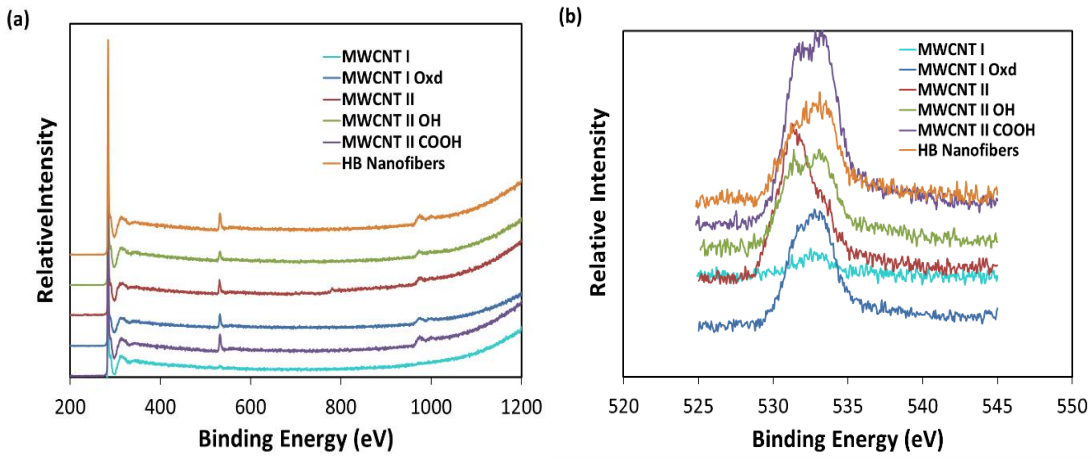

Figure 5.6 (a) XPS Survey scans and (b) XPS O1s peaks for specialty carbons

Figure 5.7 and 5.8 shows the XRD patterns and STEM images of the catalysts that were prepared on the pre washed carbon supports at the optimum pH of adsorption. The corresponding weight loadings of the catalysts and the XRD derived particle sizes are listed in Table 5.2. Figure 5.7 shows the deconvolutions of all the XRD patterns on the inset. The deconvolutions have been done based on the Pt FCC and Pt_3O_4 peaks as has been mentioned in detail in Chapters 3 and 4. As has been mentioned in earlier chapters, all the catalysts consisted of both the platinum metal and oxide phases. The Figures 5.7a and 5.7g show that the particles were fit with a bimodal distribution. This is also confirmed with the STEM images in Figures 5.9 a and g. For all the deconvolutions, the support subtracted signal still showed the presence of strong graphitization. On close observation, it is seen that these peaks appear at 26°, 43°, 44° and 54° which corresponds to graphitic carbon peaks (PDF Card No: 00-001-0640). The presence of the peaks after subtraction indicates that the presence of metal may have increased the degree of graphitization in these specialty carbons.

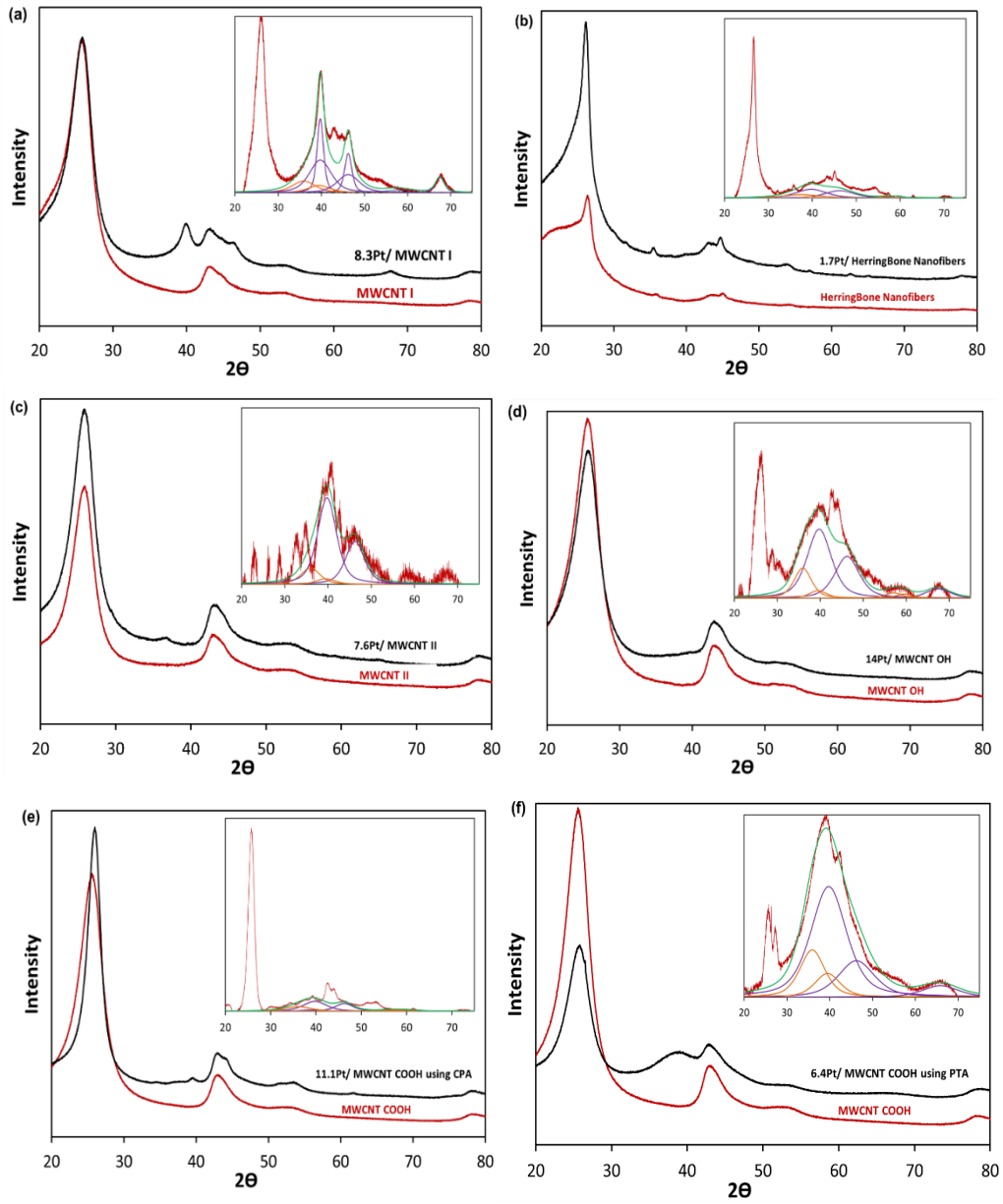
(a)
Intensity
8.3Pt/ MWCNT I
MWCNT I
2θ
(b)
Intensity
1.7Pt/ HerringBone Nanofibers
HerringBone Nanofibers
2θ
(c)
Intensity
7.6Pt/ MWCNT II
MWCNT II
2θ
(d)
Intensity
14Pt/ MWCNT OH
MWCNT OH
2θ
(e)
Intensity
11.1Pt/ MWCNT COOH using CPA
MWCNT COOH
2θ
(f)
Intensity
6.4Pt/ MWCNT COOH using PTA
MWCNT COOH
2θ

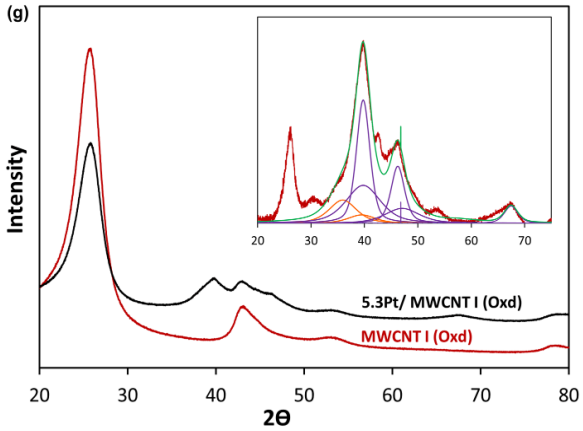

Figure 5.7 XRD Plots with deconvolutions on the inset for (a) MWCNT I (b) HB Nanofibers (c) MWCNT II (d) MWCNT-OH (e) MWCNT-COOH using CPA (f) MWCNT-COOH using PTA (g) MWCNT I-Oxidized

Table 5.2 XRD derived particle sizes for the catalysts

Specialty Carbon Support	**Precursor used for catalyst preparation**	**Metal weight loadings (%)**	**XRD Sizes (nm)**	
			Pt	**Pt_3O_4**
MWCNT I	CPA	8.3	2.9	1.5
MWCNT I Oxd	PTA	5.3	2.1	1.5
HerringBone Nanofibers	CPA	1.7	1.1	0.8
MWCNT II	CPA	7.6	1.7	1.7
MWCNT II-COOH	PTA	6.4	1.0	1.3
	CPA	11.1	1.5	1.3
MWCNT II-OH	CPA	14	1.3	1.8

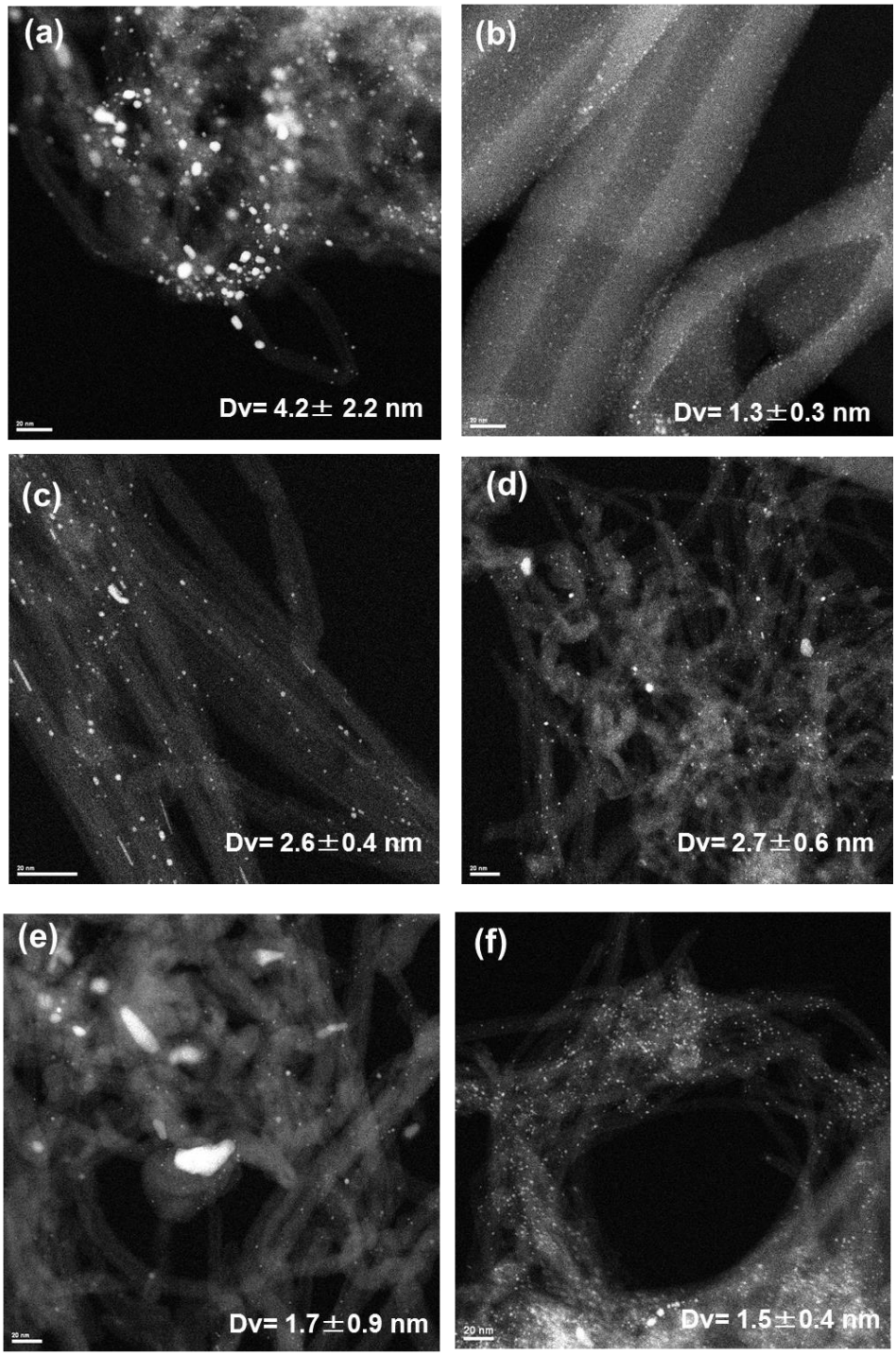
(a)
Dv= 4.2± 2.2 nm
(b)
Dv= 1.3±0.3 nm
(c)
Dv= 2.6±0.4 nm
(d)
Dv= 2.7±0.6 nm
(e)
Dv= 1.7±0.9 nm
(f)
Dv= 1.5±0.4 nm

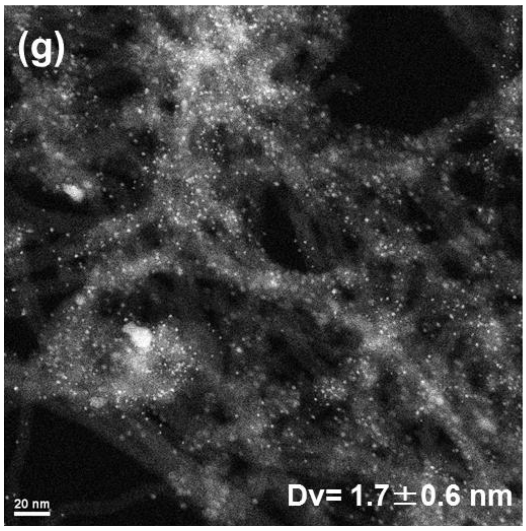

Figure 5.8 STEM images for (a) MWCNT I (b) HB Nanofibers (c) MWCNT II (d) MWCNT-OH (e) MWCNT-COOH using CPA (f) MWCNT-COOH using PTA (g) MWCNT I-Oxidized

Figure 5.8 depicts that the volume average sizes for all the catalyst nanoparticles is approximately a combination of the metal and oxide phases as was noticed in Chapter 3 which demonstrates a simplistic model of metal core with an oxide skin. The reason why the XRD derived sum of metal and oxide do not perfectly match with the STEM volume average sizes is that there are particles for each catalyst that are below 2.5 or 1.5 nm and hence, a combination of both metal and oxide phases or only the oxide or metal phase.

The STEM images also revealed that only the 1.7Pt/HB Nanofibers, 5.3Pt/MWCNT-oxd and 6.4Pt/MWCNT-COOH had good coverage of metal nanoparticles which meant that there was metal deposition on all the nanotubes despite their inherent hydrophobicity (Figure 5.9). This is probably due to the fact that HB nanofibers as well as the –COOH functionalized tubes have ample defect sites that allow the anchoring of metal nanoparticles [101, 102].

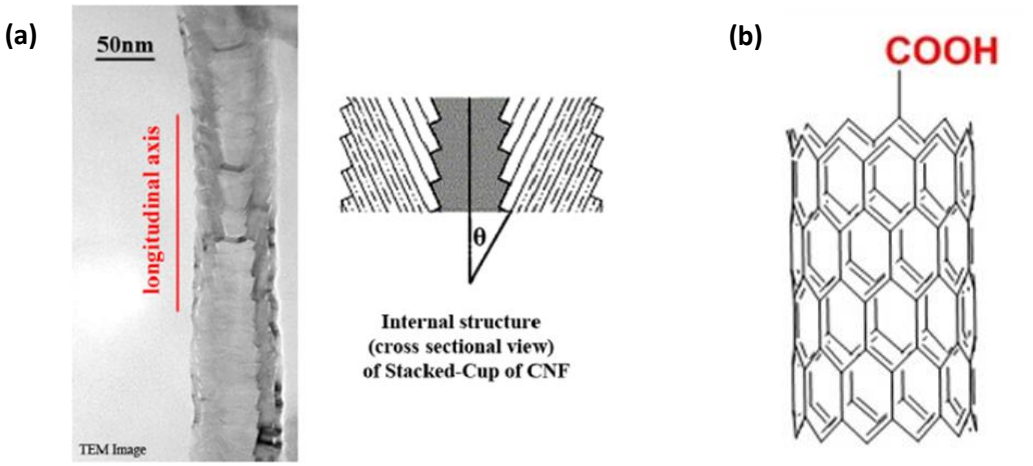

Figure 5.9 (a) STEM image and schematic of Herring Bone nanofibers (b) schematic of –COOH functionalized multiwalled carbon nanotubes

A tilting experiment was performed in STEM to determine whether the nanoparticles were homogeneously distributed on the inside as well as the outside of the nanotubes. Figure 5.10 shows four STEM images from no tilt to $+5^{o}$ and $+15^{o}$ clockwise tilt. Figure 5.10b is the composite image formed by superposing the no tilt image with the $+5^{o}$ tilt whereas 5.10c is the composite image formed by superposing the $+5^{o}$ and $+15^{o}$ tilt. The particles that do not move in between the tilts are on the inside of the nanotube whereas the ones that move are on the outside. This experiment showed that SEA was able to homogeneously distribute nanoparticles on the inside as well as the outside of the nanotubes.

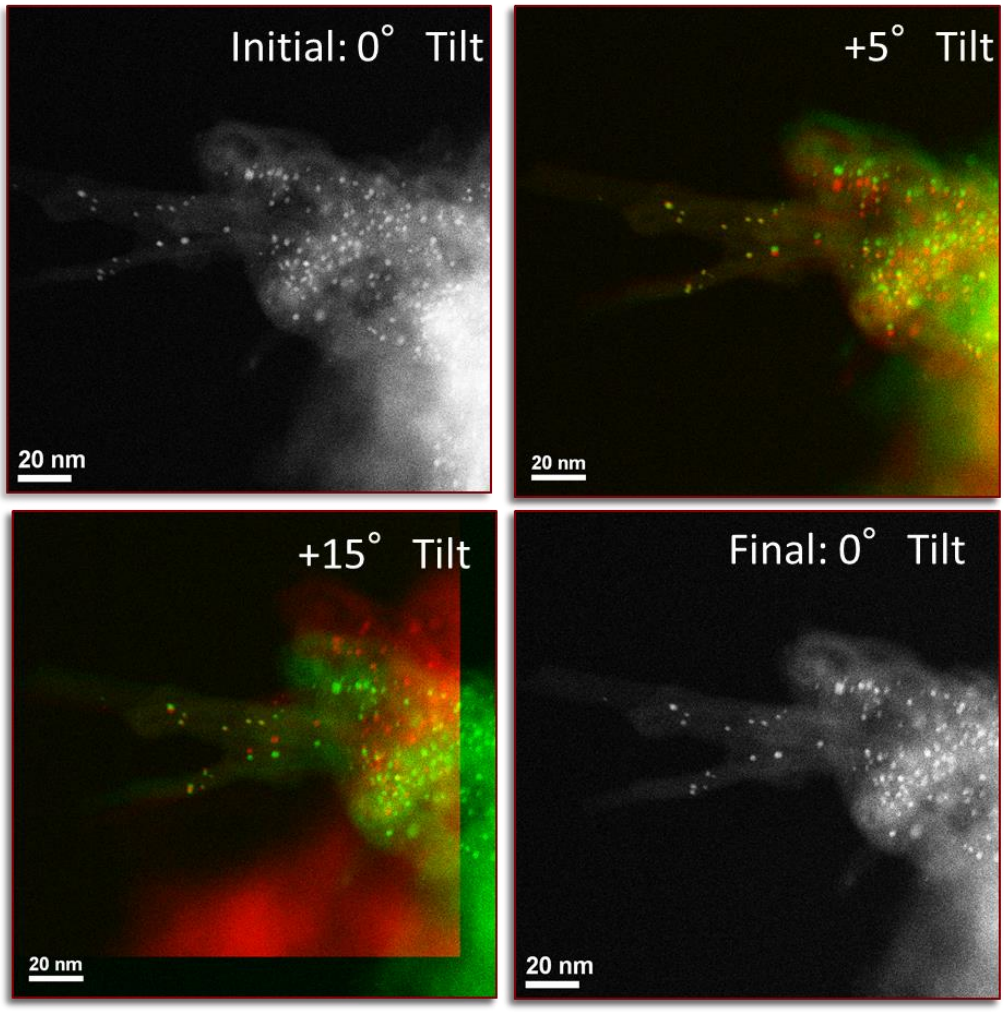

Figure 5.10 STEM images for 11.1Pt/ MWCNT II-COOH showing (a) Initial- no tilt (b) +5° tilt (c) +10° tilt (d) Final-no tilt

5.4 Conclusion

Strong Electrostatic Adsorption (SEA) has been demonstrated as a simple, scientific method to prepare well dispersed Pt nanoparticles over a variety of specialty carbons: multi-walled nanotubes, nanofibers, graphene nanoplatelets, etc. The specialty carbons displayed volcano-shaped uptake curves typical of electrostatic adsorption for both Pt anions at low pH and Pt cations at high pH. However, the regimes of uptake often did not correspond to the measured PZC. It was seen that the PZC of many of

the carbons could be changed with washing, and so was likely affected by residual impurities of the manufacturing process. This renders the measured PZC of these specialty carbons unreliable for predicting anion and cation uptake. On the other hand, the anion and cation uptake curves provide an "effective" PZC and do indicate the optimal pH for the synthesis of ultrasmall nanoparticle synthesis.

REFERENCES

[1] R.A. van Santen, P.W.N.M. van Leeuwen, J.A. Moulijn, B.A. Averill, Catalysis: An Integrated Approach, Elsevier, 1999.

[2] S.A.Topham, The History of the Catalytic Synthesis of Ammonia, Catalysis, Science and Technology, Springer Verlag, Berlin, 1985.

[3] J. Clark, D. Macquarrie, Handbook of Green Chemistry and Technology, Wiley Blackwell, 2002.

[4] L.J.M.J. Blomen, M.N. Mugerwa, Fuel Cell Systems, Springer, 1993.

[5] J. Erjavec, Automotive Technology, Cengage Learning, 2000.

[6] F. Rodriguez-Reinso, The Role of Carbon Materials in Heterogeneous Catalysis, Carbon, 3, (1998)159-175.

[7] F.Coloma, A.Sepulveda-Escribano, F. Rodriguez-Reinso, Heat-Treated Carbon Blacks as Supports for Platinum Catalysts, Journal of Catalysis, 154 (1995) 299-305.

[8] J.A.Menendez, J.Phillips, B.Xia, L.R.Radovic, On the Modification and Characterization of Chemical Surface Properties of Activated carbon: In Search of Carbons with Stable Basic Properties, Langmuir, 12 (1996) 4404-4410.

[9] D.S.Cameron, S.J.Cooper, I.L.Dodgson, B.Harrison, J.W.Jenkins, Carbons as Supports for Precious Metal Catalysts, Catal. Today, 7 (1990) 113-137.

[10] E.Antolini, Carbon Supports for Low-Temperature Fuel Cell Catalysts, Applied Catalysis B-Environmental, 88 (2009) 1-24.

[11] F.Coloma, A.Sepulveda-Escribano, J.L.G.Fierro, F. Rodriguez-Reinso, Gas-phase Hydrogenation of Crotonaldehyde over Pt/Activated Carbon Catalysts. Influence of the Oxygen Surface Groups on the Support, Applied Catalysis A: General, 150 (1997) 165-183.

[12] E. Guille´n , R. Rico, J. M. Lo´pez-Romero, J. Bedia, J.M.Rosas , J. Rodrı´guez-Mirasol, T. Cordero. Applied Catalysis A: General, 368 (2009) 113-120.

[13] B. Pawelec, R. Mariscal, J.L.G. Fierro, A. Greenwood, P.T. Vasudevan, Carbon-Supported Tungsten and Nickel Catalysts for Hydrodesulfurization and Hydrogenation Reactions, Applied Catalysis A:General, 206 (2001) 295-307.

[14] http://www.carbon-black.org/index.php/about-icba

[15] P. Serp, B.Machado, Nanostructured Carbon Materials for Catalysis (2015)1-45

[16] P.Serp, M.Corrias, P.Kalck, Carbon Nanotubes and Nanofibers in Catalysis, Applied Catalysis A: General., 253 (2003) 337–358.

[17] K.B.K.Teo, C. Singh, M. Chhowalla, W.I.Milne, Catalytic Synthesis of Carbon Nanotubes and Nanofibers, Encyclopedia of Nanoscience and Nanotechnology X (2003) 1-22.

[18] J.M. Solar, F.J. Derbyshire, V.H.J. de Beer, L.R. Radovic, Effects of Surface and Structural Properties of Carbons on the Behavior of Carbon-supported Molybdenum Catalysts, Journal of Catalysis, 129 (1991) 330-342.

[19] N. Krishnakutty, M.A. Vannice, The Effect of Pretreatment on Pd/C Catalysts, Journal of Catalysis, 155 (1995) 312-326.

[20] A. Sepulveda-Escribano, F. Coloma, F. Rodriguez-Reinso, Platinum Catalysts supported on Carbon Blacks with different Surface Chemical Properties, Applied Catalysis A: General, 173 (1998) 247-257.

[21] D. Briggs, G.Bong, E. Leong, L. Oei, G.Lestari, A.T. Bell, Effect of Support Composition and Pretreatment on the Activity and Selectivity of Carbon-supported PdCunClx Catalysts for the Synthesis of Diethyl Carbonate, Journal of Catalysis, 276 (2010) 215-228.

[22] F.Coloma, A.Sepulveda-Escribano, J.L.G.Fierro, F. Rodriguez-Reinso, Preparation of Platinum Supported on Pregraphitized Carbon Blacks, Langmuir, 10 (1994) 750-755.

[23] J.W. Niemantsverdriet, Spectroscopy in Catalysis: An Introduction, 2007.

[24] J.R. Regalbuto, Strong Electrostatic Adsorption of metals onto catalyst supports, Catalyst Preparation: Science and Engineering, CRC Press, 2016.

[25] J.P.Brunelle, Preparation of Catalysts by Metallic Adsorption on Mineral Oxides, Pure Applied Chem, 50 (1978) 1211.

[26] L. D'Souza , J.R. Regalbuto, J.T. Miller, Preparation of carbon supported cobalt by electrostatic adsorption of [Co(NH3)6]Cl3, Journal of Catalysis, 254 (2008) 157–169.

[27] N. Santhanam, T.A. Conforti, W. Spieker, J.R. Regalbuto, Nature of metal catalyst precursors adsorbed onto oxide supports, Catalysis Today, 21 (1994) 141-156.

[28] G.M. Schwab, Electronics of Supported Catalysts, Adv. Catalysis, 27 (1978) 1-22.

[29] D. Nerhing, H. Dreyer, Chem.Tech, 12 (1960) 343.

[30] M.C. Roman-Martinez, D.Cazorla-AMora, A.Linares-So'Lano, C. Salinas-Martinez De Lecea, Metal-Support Interactions in Pt/C Catalysts: Influence of the Support Surface Chemistry and the Metal Precursor, Carbon, 33 (1995) 3-13.

[31] J.M.M.Tengco, Y.K.Lugo-Jose, J.R.Monnier, J.R.Regalbuto, Chemisorption-XRD Particle Size Discrepancy of Carbon Supported Palladium: Carbon Decoration of Pd, Catalysis Today, 246 (2015) 9-14.

[32] C. Amorim, M.A. Keane, Palladium Supported on Structured and Non-Structured Carbon: A Consideration of Pd Particle Size and the Nature of Reactive Hydrogen, Journal of Colloid and Interface Science, 322 (2008) 196-208.

[33] N. Krishnakutty, M.A.Vannice,The Effect of Pre-treatment on Pd/C Catalysts, Journal of Catalysis, 155 (1995), 312-326.

[34] J.R. Gallagher, T. Li, H. Zhao, J. Liu, Y. Lei, X. Zhang, Y. Ren, J. W. Elam, R. J. Meyer, R. E. Winans, J. T. Miller, In situ diffraction of highly dispersed supported platinum nanoparticles, Catal. Sci. Technol., 4 (2014) 3053-3063.

[35] F.J. Gracia, L. Bollmann, E.E. Wolf, J.T. Miller and A.J. Kropf, In situ FTIR, EXAFS, and activity studies of the effect of crystallite size on silica-supported Pt oxidation catalysts, Journal of Catalysis, 220 (2003) 382–391.

[36] J. Park and J.R Regalbuto, A simple, accurate determination of oxide PZC and the strong buffering effect of oxide surfaces at incipient wetness, J. of Coll. Interf. Sci., 175 (1995) 239-252.

[37] K.O'Connell, J.R. Regalbuto, High Sensitivity Silicon Slit Detectors for 1 nm Powder XRD Size Detection Limit, Catal Lett, 145 (2015) 777– 783.

[38] K.P. de Jong, Synthesis of Solid Catalysts, Wiley-VCH, Fuel Cell Systems, Springer, 2009.

[39] B. Zhang and D.S. Su, Probing the Metal–Support Interaction in Carbon- Supported Catalysts by using Electron Microscopy, ChemCatChem, DOI: 10.1002/cctc.201500666.

[40] N. Job, M. Chatenet, S. Berthon-Fabry, S. Hermans, F. Maillard, Efficient Pt/carbon electrocatalysts for proton exchange membrane fuel cells: Avoid chloride-based Pt salts!, Journal of Power Sources, 240 (2013) 294-305.

[41] H.P. Klug, L.E. Alexander X-ray diffraction procedures: for polycrystalline and amorphous materials, 2nd edn. Wiley-VCH, New York (1974).

[42] J.M. Hudspeth, K.O. Kvashnina, S.A.J Kimber, E.P. Mitchell E.P, Synchrotron X-Ray Scattering as a Tool for Characterizing Catalysts on Multiple Length Scales, Oil Gas Sci. Technol, 70 (2015) 429-436.

[43] Z. Ristanovic and B.M. Weckhuysen, Breakthroughs in Hard X-ray Diffraction: Towards a Multiscale Science Approach in Heterogeneous Catalysis, Angew. Chem. Int. Ed. 53, (2014) 8556 – 8558.

[44] B. Ingham, Crystallography Reviews, 21 (2015) 229-303.

[45] M.R.V. Jørgensen, V.R. Hathwar, N. Bindzus , N. Wahlberg, Y.S. Chen, Contemporary X-ray electron-density studies using synchrotron radiation J. Overgaarda, B.B. Iversena, IUCrJ, 1 (2014) 267–280.

[46] K.H. Cats, B.M. Weckhuysen, Combined Operando X-ray Diffraction/Raman Spectroscopy of Catalytic Solids in the Laboratory: The Co/TiO2 Fischer–Tropsch Synthesis Catalyst Showcase, ChemCatChem, 8 (2016) 1531-1542.

[47] H.F. Chung, F. Smith, Industrial Applications of X Ray Diffraction, CRC Press (1999)

[48] T. Taguchi, A new position sensitive area detector for high-speed and high sensitivity X-ray diffraction analysis, Powder Diffr, 21 (2006) 97–101.

[49] R.N. Singh, R. Awasthi and C.S. Sharma, Review: An Overview of Recent Development of PlatinumBased Cathode Materials for Direct Methanol Fuel Cells Int. J. Electrochem. Sci., 9 (2014) 5607 – 5639.

[50] P. Gélin, M. Primet, Complete Oxidation of Methane at Low Temperature Over Noble Metal Based Catalysts: A Review, Applied Catalysis B Environmental, 39 (2002) 1–37.

[51] E. Bailón-García, F. J. Maldonado-Hódar, A.F. Pérez-Cadenas and F. Carrasco-Marín, Catalysts supported on carbon materials for the selective hydrogenation of citral, Catalysts, 3 (2013) 853-877.

[52] J.J.H.B. Sattler, J. Ruiz-Martinez , E. Santillan-Jimenez and B.M. Weckhuysen, Catalytic Dehydrogenation of Light Alkanes on Metals and Metal Oxides, Chemical Reviews, 114 (2014) 10613-10653.

[53] Z. Liu Z, LM. Gan, L. Hong L, W. Chen, J.Y Lee, Carbon-supported Pt nanoparticles as catalysts for proton exchange membrane fuel cells, Journal of Power Sources, 139 (2005) 73–78Y.

[54] Y. Tang , L. Zhang, Y. Wang , Y. Zhou, Y. Gao, C. Liu , W. Xing, T. Lu, Preparation of a carbon supported Pt catalyst using an improved organic sol method and its electrocatalytic activity for methanol oxidation, Journal of Power Sources, 162 (2006) 124–131.

[55] H. Cho, H.S. Park, Y.H. Cho, D.S. Jung, H.Y. Park, Y.E. Sung, Effect of platinum amount in carbon supported platinum catalyst on performance of polymer electrolyte membrane fuel cell, Journal of Power Sources, 172 (2007) 89–93.

[56] F. Sen, G. Gokagac, Different sized platinum nanoparticles supported on carbon: an XPS study on these methanol oxidation catalysts J. Phys. Chem. C, 111 (2007) 5715-5720.

[57] X. Hao, S. Barnes, J.R. Regalbuto, A fundamental study of Pt impregnation of carbon: Adsorption equilibrium and particle synthesis, Journal of Catalysis, 279 (2011) 48–65.

[58] M.S. Contreras, C.A. Pa´ ez, L. Zubizarreta , A. Le´onard , S. Blacher, C.G. Olivera-Fuentes, A. Arenillas, J.P. Pirard, A comparison of physical activation of carbon xerogels with carbon dioxide with chemical activation using hydroxides, N. Job, Carbon, 48 (2010) 3157-3168.

[59] D. Zhao, Q. Huo, J. Feng , B.F. Chmelka, G.D. Stucky, Nonionic Triblock and Star Diblock Copolymer and Oligomeric Surfactant Syntheses of Highly Ordered, Hydrothermally Stable, Mesoporous Silica Structures, J. Am. Chem. Soc., 120 (1998) 6024-6036.

[60] X. Hao, L. Quach , J. Korah, W.A. Spieker, J.R. Regalbuto, The control of platinum impregnation by PZC alteration of oxides and carbon, Journal of Molecular Catalysis A Chemical, 219 (2004) 97–107.

[61] M. Wojdyr, *Fityk*: a general-purpose peak fitting program, J. Appl. Cryst., 43 (2010) 1126-1128.

[62] R.P. Campos, A.C. Cuevas, R.E. Muñoz, Materials Characterization, Springer International Publishing (2015).

[63] E.E. Galloni, A.E. Roffo Jr, The crystalline structure of Pt_3O_4, The Journal of Chemical Physics, 9 (1941) 875-877.

[64] T. Kyotani, Control of Pore Structure in Carbon, Carbon 38 (2000) 269–286.

[65] W. Han, G. Zhang, G. Lu and Z. Tang, Influence of pore structures of a carbon support on the surface textures of a CO oxidation catalyst, RSC Adv., 5 (2015) 59666-59676.

[66] M.M. Dubinin, Adsorption properties and microporous structures of carbonaceous adsorbents, Carbon, 25 (1987) 5, 593-598.

[67] D.C.S. Azevedoa, J. C.S. Araújoa, M.B. Netoa, A. E. B. Torresa, E. F. Jaguaribe, C. L. Cavalcante, Microporous activated carbon prepared from coconut shells using chemical activation with zinc chloride, Microporous and Mesoporous Materials, 100 (2007) 361-364.

[68] N. Job , B. Heinrichs, A. Leonard, J.F. Colomer, J. Marien , J.P. Pirard, Avoiding Mass Transfer Limitations in Carbon Supported Catalysis by using Carbon Xerogel as Supports, Chemistry for Sustainable Development, 14 (2006) 571-575.

[69] R.H. Hurt, A.F. Sarofim, and J.P. Longwell, Role of Microporous Surface Area in Uncatalyzed Carbon Gasification, Energy & Fuels, 5 (1991)5, 290-299.

[70] Y. Zhang, M.M. Maroto-Valer and Z. Tang, Microporous Activated Carbons produced from Unburned Carbon Fly-Ash and their Application for CO_2 Capture, Fuel Chemistry Division, 49 (2004) 1, 304-305.

[71] J.C. Chaston, The Oxidation of the Platinum Metals, Platinum Metals Rev., 19 (1975) 4, 135-140.

[72] V. Johánek, M. Václav, I. Matolínová, I. Khalakhan, S. Haviar, V. Matolín, High low-temperature CO oxidation activity of platinum oxide prepared by magnetron sputtering, Applied Surface Science, 345 (2015) 319–328.

[73] F. Sü en, G. Go1kagacü, Different Sized Platinum Nanoparticles Supported on Carbon: An XPS Study on These Methanol Oxidation Catalysts, J. Phys. Chem. C, 111 (2007) 5715-5720.

[74] J.F. Sauvage, R.H. Baker, A.S. Hussey, The Hydrogenation of Cyclohexenes over Platinum Oxide, J. Am. Chem. Soc, 82 (1960) 23, 6090–6095.

[75] L. Olsson, E. Fridell, The Influence of Pt Oxide Formation and Pt Dispersion on the Reactions $NO_2 \Leftrightarrow NO+1/2\ O_2$ over Pt/Al_2O_3 and $Pt/BaO/Al_2O_3$, Journal of Catalysis, 210 (2002) 340–353.

[76] W.E Kaufmann, R. Adams, The Use of Platinum Oxide as a Catalyst in the reduction of Organic Compounds. IV. Reduction of Furfural and its Derivatives, J. Am.Chem.Soc., 45 (1923) 12, 3029–3044.

[77] L.K. Ono, J.R. Croy, H. Heinrich, B.R. Cuenya, Oxygen Chemisorption, Formation, and Thermal Stability of Pt Oxides on Pt Nanoparticles Supported on SiO2/Si(001): Size Effects, J. Phys. Chem. C, 115 (2011) 16856–16866.

[78] R. Banerjee , Q. Liu, J.M.M. Tengco, J.R. Regalbuto, Detection of Ambient Oxidation of Ultrasmall Supported Platinum Nanoparticles with Benchtop Powder X-ray Diffraction, Catal Lett (Submitted for publishing).

[79] J. S. Albero, A. S. Albero, F. Rodrı´guez-Reinoso, M. Thommes, Physical characterization of activated carbons with narrow microporosity by nitrogen (77.4 K), carbon dioxide (273 K) and argon (87.3 K) adsorption in combination with immersion calorimetry, Carbon, 50 (2012) 3128–3133.

[80] L.E. Drain, Permanent electric quadrupole moments of molecules and heats of adsorption, Trans. Faraday Soc., 49 (1953) 650-654.

[81] N. Job, R. Pirard, J.P. Pirard and C. Alié, Non-Intrusive Mercury Porosimetry: Pyrolysis of Resorcinol-Formaldehyde Xerogels, Part. Part. Syst. Charact., 23 (2006) 72–81.

[82] W.D. Harkins and G. Jura, Surfaces of Solids XIII. A Vapor Adsorption Method for the Determination of the Area of a Solid without the Assumption of a Molecular Area, and the Areas Occupied by Nitrogen and other Molecules on the Surface of a Solid, J. Am. Chem. Soc., 66 (1944) 1366

[83] S. Lambert, N. Job, D'Souza, M. Fernando, R. Pereira, R. Pirarda, B. Heinrichs, J.L. Figueiredo, J.P. Pirarda, J. R. Regalbuto, Synthesis of very highly dispersed platinum catalysts supported on carbon xerogels by the strong electrostatic adsorption method, Journal of Catalysis 261 (2009) 23–33.

[84] H.R. Cho, J. R. Regalbuto, The rational synthesis of Pt-Pd bimetallic catalysts by electrostatic adsorption, Catalysis Today, 246 (2015) 143–153.

[85] T. Soboleva, X. Zhao, K. Malek, Z. Xie, T. Navessin, and S. Holdcroft, On the Micro-, Meso-, and Macroporous Structures of Polymer Electrolyte Membrane Fuel Cell Catalyst Layers, Applied Materials and Interfaces, 2 (2010) 2, 375–384.

[86] A.K.M.M. Islam, J.I. Hwang, S.E. Lee & J.E. Kim, Comparative study of carbon black and activated carbon adsorbents for removal of carbofuran from aqueous solution, Desalination and Water Treatment, 57 (2016) 21512–21523.

[87] K. J. Naidoo, G. Klatt, K.R. Koch and D. J. Robinson, Geometric Hydration Shells for Anionic Platinum Group Metal Chloro Complexes, Inorg. Chem., 41 (2002) 1845-1849.

[88] Y. Marcus, Thermodynamics of Solvation of Ions, J. CHEM. SOC. FARADAY TRANS., 89 (1993) 713-718.

[89] K. Kuribayashi, S.Kitamura, Preparation of Pt-PtO*x* thin films as electrode for memory capacitors, Thin Solid Films, 400 (2001) 160-164.

[90] R. B. Shumbera, H.H Kan, J. F. Weaver, Oxidation of Pt (100)-hex-R 0.7 degrees by gas phase oxygen atoms, Surf. Sci., 601 (2007) 235-246.

[91] R. S. Hsu, Catalysts for Polymer Electrolyte Fuel Cell, Ontario, Canada, University of Waterloo, PhD Thesis (2010).

[92] Y.A. Kim, T. Hayashi, M. Endo, M.S. Dresselhaus. Springer Handbook of Nanomaterials, Carbon Nanofibers (2011).

[93] K.P. De Jong, J.W. Geuss, Carbon Nanofibers: Catalytic Synthesis and Applications Catal. Rev. Sci-Eng, 42 (2000) 481-510.

[94] S. Lee, Z. Zhang, X. Wang, Lisa D. Pfefferle, G. L. Haller, Characterization of multi-walled carbon nanotubes catalyst supports by point of zero charge, Catalysis Today, 164 (2011) 68-73.

[95] J.M. Planeix, N. Coustel, B. Coq, V. Brotons, P.S. Kumbhar, R. Dutrartre, P. Geneste, P. Bernier, P.M. Ajayan, Application of Carbon Nanotubes as Supports in Heterogeneous Catalysis J. Am.Chem.Society, 116 (1994) 7935-7936.

[96] B.L. Mojet, M.S. Hoogenraad, A.J. Van Dillen, J.W. Geuss, D.C. Koningsberger, J.chem. Soc. Faraday Trans. 93 (1997) 4371.

[97] L. Zhang, G. Wen, H. Liu, N. Wang, D. Su, Preparation of Carbon Nanotubes Supported Pd Catalysts by an Electrostatic Adsorption Method, ChemCatChem, DOI:10.1002/cctc.200.

[98] C.C. Chusuei, M. Wayu, Characterizing Functionalized Carbon Nanotubes for Improved Fabrication in Aqueous Solution Environments Electronic Properties of Carbon Nanotubes (2011) ISBN: 978-953-307-499-3, InTech, DOI: 10.5772/16743.

[99] O. Akbarzadeh, N. A.M. Zabidi, B.Abdullah, D.Subbarao, Synthesis of Co/CNTs Catalyst via Strong Electrostatic Adsorption: Effect of Calcination Condition Advanced Materials Research, 1109 (2015) 1.

[100] X. Hao, L. Quach, J. Korah, W.A. Spieker1, John R. Regalbuto, The control of platinum impregnation by PZC alteration of oxides and carbon, Journal of Molecular Catalysis A: Chemical, 219 (2004) 97–107.

[101] V. Gupta, T. A. Saleh, Synthesis of Carbon Nanotube-Metal Oxides Composites, Adsorption and Photo-degradation, Carbon Nanotubes - From Research to Applications (2011).

[102] L. Guadagno , M. Raimondo , V. Vittoria , L. Vertuccio , K. Lafdi , B. De Vivo , P. Lamberti , G. Spinelli, V. Tucci, Nanotechnology 24 (2013) 305704.